FACHBEREICH PHYSIK
BERGISCHE UNIVERSITÄT
WUPPERTAL

Measurement and Interpretation of Muon-Pair Production at LEP energies above the Z^0 Resonance

Dissertation zur Erlangung des Doktorgrades der Naturwissenschaften (Dr. rer. nat.)

eingereicht an den

Fachbereich Physik der Bergischen Universität Wuppertal

von

Anette Behrmann

1. Gutachter: Prof. Dr. J. Drees
2. Gutachter: Prof. Dr. K.-H. Becks

WUB-DIS 2003–8
August 2003

Gewidmet meiner Großmutter Erika Behrmann

Abstract

In this report the muon-pair production at energies well above the Z resonance is investigated. The analysis presented here is based on data taken with the DELPHI detector during the years from 1997 to 2000 at nominal center-of-mass energies of 183-207 GeV corresponding to an integrated luminosity of $\sim$ 645 pb^{-1}. The measurement of the total cross sections, the forward-backward asymmetries and differential cross sections are presented. The results obtained are compared to the Standard Model predictions. No significant deviations have been found. The results are also interpreted in terms of new physics phenomena like the possible existence of an additional heavy gauge boson, so-called Z', and the graviton exchange in the framework of quantum theory of gravity in large extra dimensions. No evidence for any of this models has been found and exclusion limits at 95% confidence level have been derived. A possible Z' should have a mass of $\mathrm{M}_{\mathrm{Z}'} >$ 360-530 $\mathrm{GeV/c^2}$ dependent on the model considered (E_6, L-R). A lower limit on $\mathrm{M_s}$, the *String* scale, of 794/804 $\mathrm{GeV/c^2}$ ($\lambda = \pm 1$) was obtained.

Kurzfassung

Die vorliegende Arbeit befasst sich mit der Messung der Myonpaar Produktion bei Energien oberhalb der Z Resonanz. Die Analyse basiert auf dem Datensatz, der von 1997 bis 2000 bei nominalen Schwerpunktenergien von 183 bis 207 GeV mit dem DELPHI Detektor aufgenommen wurde. Dies entspricht einer integrierten Luminosität von 645 pb^{-1}. Die Messung der totalen und differentiellen Wirkungsquerschnitte und der Vorwärts-Rückwärts-Asymmetrien werden präsentiert und mit den Vorhersagen des Standard Modells verglichen. Alle ermittelten Ergebnisse sind in guter Übereinstimmung mit der Theorie. Die Ergebnisse werden auch im Hinblick auf neue Phänomene jenseits des Standard Modells interpretiert. Dies sind die mögliche Existenz eines weiteren schweren Eichbosons, genannt Z', sowie der Austausch eines vorhergesagten Gravitons im Rahmen einer Quantentheorie der Gravitation in grossen extra Dimensionen. Keines dieser Modelle kann mit den vorliegenden Messungen bestätigt werden, jedoch wurden Ausschlussgrenzen auf 95% Vertrauensniveau ermittelt. Aus den Messungen ergibt sich eine untere Grenze der Z' Masse von 360-530 $\mathrm{GeV/c^2}$, abhängig von dem betrachteten Modell (E_6, L-R). Das untere Limit auf die *String*-Skala $\mathrm{M_s}$ kann mit 794/804 $\mathrm{GeV/c^2}$ ($\lambda = \pm 1$) angegeben werden.

Contents

List of Tables

List of Figures

Chapter 1

Introduction

The field of particle physics has been explored very intensively in the last century, considering the discovery of the electron in 1897 as the starting point. Since then, many experiments have been carried out, followed by the discovery of other particles. The theoretical concepts have been very successful in describing their properties and expanded our understanding of nature. The present theory that describes the elementary particles and their fundamental interactions except for the gravity is the so-called Standard Model. Although the Standard Model has manifest itself to a very high level of precision in a large number of experiments in the last decades, it is still called a *model*. This should not curtail its enormous success.

In the Standard Model, the strong, the electromagnetic and the weak force are established in the framework of gauge theories. The electromagnetic force between charged particles is mediated by the exchange of the massless photon. According to the unified electroweak theory - developed in the 1960s - the weak nuclear interactions are mediated by the exchange of charged (W^+, W^-) and neutral (Z) massive gauge bosons, such as in the beta decay (via W exchange). These have been discovered in 1983 at CERN, the European laboratory for particle physics near Geneva in Switzerland. The strong interactions are mediated by the exchange of so-called gluons, which were discovered in 1979 at the DESY laboratory in Germany. The first identified particles of matter were the leptons, to which the electron belongs to as well as the muon (1936) and the tau lepton (1975), and which do not feel the strong force. Each of the three charged and massive leptons is associated to its own uncharged neutrino, which are nowadays believed to have very small masses and which only take part in the weak force. The strongly interacting particles are the hadrons, discovered since the 1940s, which are known to be composite bound states of more elementary constituents, the quarks. The heaviest of the six quarks, the top quark ($\sim$ 175 GeV/c^2), was discovered in 1994 at the Fermilab laboratory near Chicago. At the same laboratory, the last missing particle of the fermion families in the Standard Model was observed in the year 2000, the tau-neutrino. The remaining particle predicted by the Standard Model and not yet observed is the Higgs boson which is assumed to give the other massive particles their masses.

Particle physics has been dominated in the recent years by precision tests of the Standard Model, both the strong and the electroweak interactions. Tests of the electroweak sector have been carried out, among others, by high energy collisions between electrons and positrons at LEP. The large electron positron collider LEP, the largest experiment at CERN so far, was operating successfully during the years 1989 to 2000. In a first step, LEP was running near the energy corresponding to the mass of the Z resonance (about 91 GeV), called the LEP I period. At this energy, the rate of electron-positron interactions is increased significantly, yielding to a resonance peak. This allowed to measure the mass of the Z boson as well as the peak height and width which depend on the number of decay modes of the Z boson. From this measurement, the number of neutrino species that were expected to be three was confirmed.

In the last years of operation, the LEP beam energy was raised well above the Z resonance, approaching the threshold for W^+W^- production ($\sim$ 160 GeV) in 1996 and reaching the highest energy achieved at e^+e^- colliders, 209 GeV, in the last year of running. Besides the measurement of the W boson properties, the main goals of the LEP II phase were the search for the Higgs boson and the search for new physics beyond the Standard Model, as for examples supersymmetric particles or even unexpected effects. The fermion-pair production is a stringent test of the Standard Model parameters. While this process allowed the precise measurement of the Z boson properties at LEP I it is still dominant at energies well above. Deviations of the measurements from the expectation may be hints for new physics phenomena.

In this thesis, the muon-pair production at energies above the threshold of the Z resonance is investigated. The analysis is based on data taken with the DELPHI detector in the years from 1997 to 2000. Chapter 2 outlines the theoretical framework of the Standard Model of particles physics and phenomenological aspects of fermion-pair production in e^+e^- annihilation. Furthermore, possible extensions to the SM, including new physics scenarios considered here, are described. In Chapter 3, a short overview of the experiment, the LEP accelerator and the DELPHI detector, is given. Chapter 4 describes in detail how the muon pairs are selected and how the effective center-of-mass energy, which is an important feature for the classification of events, is reconstructed. Chapter 5 presents the methods for the determination of the cross sections and forward-backward asymmetries for the muon-pair production and the obtained results. A discussion of these results is given in Chapter 6, where a quantitative comparison to the predicted values from the Standard Model is made. In addition, the results are interpreted in terms of models including new physics phenomena; these are the possible existence of an additional heavy gauge boson, Z', and gravity in large extra dimensions. After the summary in Chapter 7, some technical descriptions can be found in the Appendices.

Chapter 2

Theoretical Framework

2.1 The Standard Model

The Standard Model (SM) is the present theory that describes the today known fundamental interactions between the particles except for the gravity: the weak force, the electromagnetic force and the strong force (in increasing order of strength). Its common mathematical formalism of gauge theories is expressed by the symmetry group $\mathrm{SU}(3)_C \times \mathrm{SU}(2)_L \times \mathrm{U}(1)_Y$ described in more detail in the next sections. The small strength of gravity allows to neglect its effects in high energy physics. The fundamental particles in the SM are the fermions, spin-$\frac{1}{2}$ particles that build up the matter, and the bosons, the spin-1 particles that mediate the interactions. The fermions themselves are divided into six leptons and six quarks, according to the interactions they take part. The quarks (namely up, down, charm, strange, bottom and top) take part in all interactions whereas the charged leptons (e, μ, τ) do not feel the strong force as well as the uncharged leptons, the neutrinos $(\nu_e, \nu_\mu, \nu_\tau)$, which merely take part in weak interactions. All stable matter is composed of the light fermions of the first family: the up and down quark, the components of the proton and the neutron that build up the atomic nucleus, and the electron. All other fermions, except for the neutrinos, are heavier and decay into lighter particles after a short life time. They can only be created artificially in large high energy experiments. This is also the case for anti-matter which appears to have only a tiny amount in our universe. In principle, each quark and lepton has an anti-particle with opposite quantum numbers, like the positron (e^+) which is the counterpart to the electron.

2.1.1 The Strong Force

The underlying theory of the strong force will be described very briefly as it is not of major concern to the analysis presented here. The strong interactions are described by the Quantum Chromodynamics (QCD), which is a non-abelian gauge theory based on a $\mathrm{SU}(3)_c$ [1], where c denotes the "color". Each quark flavor is a color triplet in the fundamental representation of the SU(3) gauge fields. The symmetry of the gauge group leads to 8 massless gluons, the spin-1 bosons that mediate the strong force. The gluons themselves carry the color charge which leads to gauge self-interactions. All other particles are color singulets and do not participate to the strong force. The quarks are the constituents of the hadrons which are color *neutral.* The baryons are built up by three quarks with three different colors, e.g. the proton (uud) and the neutron (udd), and the mesons consist of a quark and anti-quark pair, e.g. the pi-meson, where each quark has the anti-color of the partner. The strength of the strong force that is characterised by its coupling constant, α_s, gets small, flavor independently, with increasing energy up to the *asymptotic freedom*, where the quarks behave like free particles. At small energies α_s gets very strong leading to the *confinement* of the quarks which forbids their existence as a free particle.

2.1.2 The Electroweak Theory

The Glashow - Weinberg - Salam theory of electroweak interactions [2] is based on the $\mathrm{SU}(2)_L \times \mathrm{U}(1)_Y$ symmetry group. The formulation of the Standard Model is given by empirical facts. The fermions appear as left-handed doublets and right-handed singlets, as shown in Table 2.1. They can be characterised by the quantum numbers of the weak isospin I, I_3 and the weak hypercharge Y. The quantum numbers are related to electric charge with respect to the group SU(2)× U(1) via the Gell-Mann-Nishijima equation:

$$Q = I_3 + \frac{Y}{2} \tag{2.1}$$

There are four vector bosons that carry the electroweak forces:

$$\gamma,\ W^-,\ W^+,\ \mathrm{Z},$$

where the photon is the only massless particle ($M_W \neq 0, M_Z \neq 0$). This structure can be embedded in a gauge invariant field theory of the unified electromagnetic and weak interactions by interpreting the SU(2) × U(1) as the group of gauge transformations under which the Lagrangian is invariant. This full symmetry has to be broken by the Higgs mechanism down to the electromagnetic gauge symmetry to give the $W^\pm$, Z bosons their masses. The minimal formulation, which is the Standard Model, requires a single scalar field which is a doublet under SU(2), the Higgs field.

From gauge, fermion and Higgs fields to physical fields and parameters

The SU(2) × U(1) is generated by the isospin operators I_1, I_2, I_3, and the hypercharge Y which are the elements of the corresponding Lie algebra. Each of these charges is related to a vector field, a triplet of $W_\mu^{1,2,3}$ with $I_{1,2,3}$ and a singlet B_μ with Y, and the referring coupling constants g_2 and g_1.

The fermion fields of each lepton and quark family can be given as (without color index):

$$\Psi_i^L = \begin{pmatrix} \Psi_{i+}^L \\ \Psi_{i-}^L \end{pmatrix}, \qquad \Psi_i^R = \Psi_{i\pm}^R$$

the left-handed doublet and the right-handed singlet, where i is the family index. Only the left-handed fermion fields interact with the SU(2):

$$\Psi_L = \frac{1}{2}(1 - \gamma_5)\Psi \tag{2.2}$$

Fermion Families			Quantum Numbers			
I	II	III	I	I_3	Y	Q
$\begin{pmatrix} \nu_e \\ e \end{pmatrix}_L$	$\begin{pmatrix} \nu_\mu \\ \mu \end{pmatrix}_L$	$\begin{pmatrix} \nu_\tau \\ \tau \end{pmatrix}_L$	1/2 1/2	1/2 −1/2	−1 −1	0 −1
e_R	μ_R	τ_R	0	0	−2	−1
$\begin{pmatrix} u \\ d' \end{pmatrix}_L$	$\begin{pmatrix} c \\ s' \end{pmatrix}_L$	$\begin{pmatrix} t \\ b' \end{pmatrix}_L$	1/2 1/2	1/2 −1/2	1/3 1/3	2/3 −1/3
u_R	c_R	t_R	0	0	4/3	2/3
d_R	s_R	b_R	0	0	−2/3	−1/3

Table 2.1: The fermion families of the Standard Model with their referring quantum numbers: the weak isospin I, I_3 and weak hypercharge Y. Q is the electric charge.

The different transformations of the L and R fields are the origin of parity violation in the electroweak sector. Each left- and right-handed multiplet is an eigenstate of the weak hypercharge such that Equation (2.1) is fulfilled. To leave the electromagnetic gauge subgroup $U(1)_{em}$ unbroken after spontaneous symmetry breaking a single complex scalar doublet field is introduced, the Higgs field:

$$\Phi = \begin{pmatrix} \Phi^+ \\ \Phi^0 \end{pmatrix} = \frac{1}{\sqrt{2}} \begin{pmatrix} \Phi_1^+ + i\Phi_2^+ \\ \Phi_1^0 + i\Phi_2^0 \end{pmatrix} \tag{2.3}$$

The self-interaction of the Higgs field

$$V(\Phi) = -\mu^2 \Phi^+ \Phi + \frac{\lambda}{4} (\Phi^+ \Phi)^2 \tag{2.4}$$

is constructed such that its vacuum expectation value is non-vanishing:

$$\Phi_{min} = \frac{1}{\sqrt{2}} \begin{pmatrix} 0 \\ v \end{pmatrix}, \tag{2.5}$$

where v is related to the potential V by $v = 2\mu/\sqrt{\lambda}$. The real part of Φ^0 describes physical neutral particles with mass $M_H = \sqrt{2}\mu$. In order to generate massive fermions in a gauge invariant way, Yukawa interactions between the fermions and the physical Higgs field are introduced with couplings proportional to the fermion masses. Likewise, the interaction between the vector bosons and the gauge invariant Higgs field gives rise to their masses, with non-diagonal mass terms. The physicalfields are derived by a unitary transformation of the symmetry fields leading to the charged current:

$$W_\mu^\pm = \frac{1}{\sqrt{2}} (W_\mu^1 + i W_\mu^2), \tag{2.6}$$

and the neutral current:

$$Z_\mu = \cos\theta_{\rm W} W_\mu^3 + \sin\theta_{\rm W} B_\mu \tag{2.7}$$
$$A_\mu = -\sin\theta_{\rm W} W_\mu^3 + \cos\theta_{\rm W} B_\mu. \tag{2.8}$$

The mixing introduced in the rotation is the so-called Weinberg angle which is given by

$$\cos\theta_{\rm W} = \frac{g_2}{\sqrt{g_1^2 + g_2^2}} = \frac{M_W}{M_Z}, \tag{2.9}$$

with the diagonal mass terms of the physical fields:

$$M_W = \frac{v}{\sqrt{2}} g_2, \qquad M_Z = \frac{v}{\sqrt{2}}\sqrt{g_1^2 + g_2^2}\ . \tag{2.10}$$

In contrast to the W boson, the Z boson interacts with the right-handed fermion fields, except for the neutrinos. To describe the neutral current for all fermion fields in a common way the $(1-\gamma_5)$ structure in equation (2.2) is modified in terms of the vector couplings and axial vector couplings of the neutral current $(v_f - a_f\gamma_5)$, where

$$v_f = I_3^f - 2Q_f \sin^2\theta_{\rm W} \qquad \text{and} \qquad a_f = I_3^f \tag{2.11}$$

A_μ can be identified by the electromagnetic field $\mathrm{U}(1)_{em}$ with the massless photon as vector boson. The photon field couples to the electron via the electric charge $e = \sqrt{4\pi\alpha}$ which can be expressed in terms of the gauge couplings

$$e = \frac{g_1 g_2}{\sqrt{g_1^2 + g_2^2}} = g_2 \sin\theta_{\rm W} = g_1 \cos\theta_{\rm W}. \tag{2.12}$$

Finally, the fermion masses are obtained from the Yukawa coupling terms:

$$m_f = g_f \frac{v}{\sqrt{2}} = \sqrt{2}\,\frac{g_f}{g_2} M_W. \tag{2.13}$$

Since quarks with the same charge have different masses the diagonalisation of the quark mass matrices from the Yukawa coupling in the charged current leads to the family mixing in the quark sector [3], i.e. the mixing of the mass and the weak eigenstates:

$$\begin{pmatrix} d' \\ s' \\ b' \end{pmatrix} = \begin{pmatrix} V_{ud} & V_{us} & V_{ub} \\ V_{cd} & V_{cs} & V_{cb} \\ V_{td} & V_{ts} & V_{tb} \end{pmatrix} \begin{pmatrix} d \\ s \\ b \end{pmatrix} \tag{2.14}$$

where the transformation matrix is called the Cabibbo-Kobayashi-Maskawa matrix, U_{CKM}. Assuming massless neutrinos, no mixing in the leptonic sector exists. Due to the unitarity of U_{CKM} the mixing is not present in the neutral current.

The Lagrangian for the Standard Model after spontaneous symmetry breaking is [4]

$$\begin{aligned} \mathcal{L} \;=\; & \mathcal{L}_{gauge} + \mathcal{L}_{Higgs} + \sum_i \bar{\psi}_i (i\,\delta - m_i - \frac{m_i H}{v})\psi_i \qquad (2.15) \\ & - \frac{g}{2\sqrt{2}}(J_W^\mu W_\mu^- + J_W^{\mu\dagger} W_\mu^+) - eJ_Q^\mu A_\mu - \frac{g}{2\cos\theta_{\rm W}} J_Z^\mu Z_\mu \end{aligned}$$

The free parameters of the Standard Model

The minimal Standard Model has 18 free parameters, assuming massless neutrinos and not counting electric charge, that are not fixed by the theory and have to be determined experimentally. These are nine Yukawa couplings to the fermions, four parameters describing the CKM matrix, three independent coupling constants - one of it belongs to QCD, α_s - the Higgs mass and one additional independent gauge boson mass.

The relations above allow to replace the original set of parameters by an equivalent set of physical parameters that can be measured in a suitable experiment:

$$g_1,\, g_2,\, \lambda,\, \mu^2,\, g_f \;\rightarrow\; e,\, M_W,\, M_Z,\, M_H,\, m_f \tag{2.16}$$

A very precisely measured parameter is the Fermi constant G_F, which is the effective 4-fermion coupling constant in the Fermi model, derived by the muon lifetime. The consistency of the Standard Model with the Fermi model at low energies ($q^2 \ll M_W$) requires

$$G_\mu = \frac{\pi\alpha}{\sqrt{2}\, M_W^2 \sin^2\theta_W}. \tag{2.17}$$

The relation equivalent to formula (2.9):

$$\sin^2\theta_W = 1 \;-\; \frac{M_W^2}{M_Z^2} \tag{2.18}$$

allows the determination of the Weinberg angle and the mass of the W boson since the mass of the Z boson has been measured to a high level of precision, as well as the constant α (in Thomson scattering).

Once expressed in terms of the physical parameters the Lagrangian can be written down such that the propagators and vertices can be read off directly. The calculation of amplitudes for fermionic processes are performed by the *Feynman rules*. In general, the relations between the formal parameters and the measurable quantities at tree level are different from those at higher order perturbation theory. Furthermore, loop integrations result in divergences that have to be treated in a mathematically consistent way. The solution is the *renormalisation* of the parameters which can be performed in different schemes, e.g. the *on-shell* renormalisation. The renormalisability is one success of the Standard Model as a theory. A very detailed discussion of the Standard electroweak Model can be found in [4] from which this description is extracted.

2.1.3 Fermion-Pair Production in e^+e^- Annihilation

The fermion-pair production in the e^+e^- annihilation via the photon and Z exchange in the s-channel is described in lowest order in the Born level diagrams in Figure 2.1. In case of an electron pair in the final state, the Bhabha scattering, the t-channel exchange is also possible, but this is not considered in this analysis. Important measurable quantities predicted by the SM are the cross section and the forward-backward asymmetry.

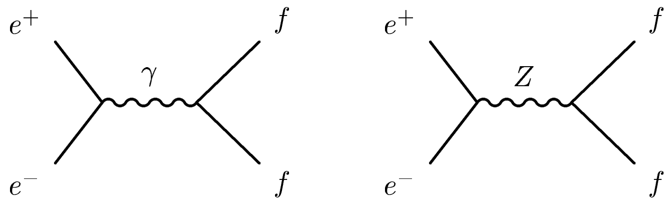

Figure 2.1: Fermion-pair production at lowest order via γ and Z exchange, $f = e,\ \mu\ \tau,\ q$

The Cross Section and Forward-Backward Asymmetry

The differential cross section is given in the following way [5]:

$$\frac{d\sigma_f}{d\Omega} = \frac{\alpha^2}{4s} N_c^f \sqrt{1-4\mu_f} \cdot \{G_1(s)\cdot(1+\cos^2\theta) + 4\mu_f G_2(s)\cdot\sin^2\theta + \sqrt{1-4\mu_f}G_3(s)\cdot 2\cos\theta\} \quad (2.19)$$

with $N_c = 3$ (quarks), 1 (leptons), $\mu_f = m_f^2/s$, $s = E_{cm}^2$, $\theta = \angle(e^-, f)$

The functions $G_i(s)$ in Equation (2.19) are:

$$\begin{aligned} G_1(s) &= Q_f^2 - 2v_e v_f Q_f \mathrm{Re}\chi_0(s) + (v_e^2 + a_e^2)(v_f^2 + a_f^2 - 4\mu_f a_f^2)|\chi_0(s)|^2 \\ G_2(s) &= Q_f^2 - 2v_e v_f Q_f \mathrm{Re}\chi_0(s) + (v_e^2 + a_e^2)v_f^2|\chi_0(s)|^2 \\ G_3(s) &= -2a_e a_f Q_f \mathrm{Re}\chi_0(s) + 4v_e a_e v_f a_f |\chi_0(s)|^2 \end{aligned} \quad (2.20)$$

which are derived from the vector and the axial vector coupling constants given in (2.11) and the propagator in the lowest order Breit-Wigner approximation:

$$\chi_0(s) = \frac{s}{s - M_Z^2 + iM_Z\Gamma_Z} \quad (2.21)$$

with the width of the Z boson

$$\Gamma_Z = \sum_f N_c^f \frac{\alpha}{3} M_Z \sqrt{1-4\mu_f}(v_f^2(1+2\mu_f) + a_f^2(1-4\mu_f)) \quad . \quad (2.22)$$

Terms in Equation (2.19) that contain factors of $\chi_0(s)$ or Q_f^2 reflect the pure Z or γ exchange, the $Q_f \cdot \mathrm{Re}\chi_0(s)$ contributions are due to the $Z-\gamma$ interference. Thus, the total cross section can be expressed in terms of the propagators in lowest order:

$$\sigma_f(s) = \sigma_Z(s) + \sigma_\gamma(s) + \sigma_{Z\gamma}(s). \quad (2.23)$$

At energies near the Z resonance the total cross section is dominated by the Z exchange and can be written as:

$$\sigma_Z(s) = \sigma_f^0 \frac{s\Gamma_Z^2}{(s-M_Z^2)^2 + \frac{s^2\Gamma_Z^2}{M_Z^2}}, \quad (2.24)$$

where σ_f^0, the cross section at the peak, can be expressed in terms of the partial decay width of the fermions:

$$\sigma_f^0 = \sigma(M_Z^2) = \frac{12\pi\Gamma_e\Gamma_f}{M_Z^2\Gamma_Z^2}, \qquad \Gamma_f = \frac{G_F M_Z^3}{6\pi\sqrt{2}}(v_f^2 + a_f^2) \quad (2.25)$$

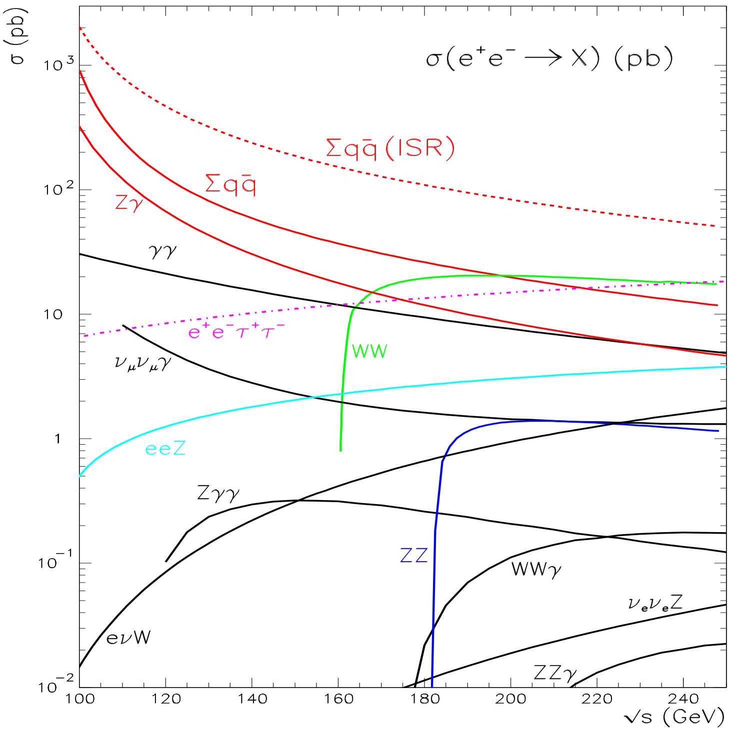

Figure 2.2: The total cross section of Standard Model processes above the Z resonance [6]

At energies well above the Z resonance the photon exchange becomes increasingly important. For example, at $\sqrt{s}$=175 GeV the ratio of the muon-pair production via γ/Z exchange is $\sigma_Z/\sigma_\gamma \simeq 0.27$. With increasing energy the cross section of the fermion-pair production drops significantly. Below the WW threshold the annihilation processes into fermion-pairs (lepton and quark pairs) still dominates. Above 161 GeV the WW- and ZZ-pair production become more important. In addition, the cross section of the two-photon process increases with $\sim (\ln(s/m_e^2))^2$, see Figure 2.2. Those processes, shown in the diagrams in Figure 2.3, can have an event topology similar to the $e^+e^- \to f\bar{f}$ process and thus being important background channels.

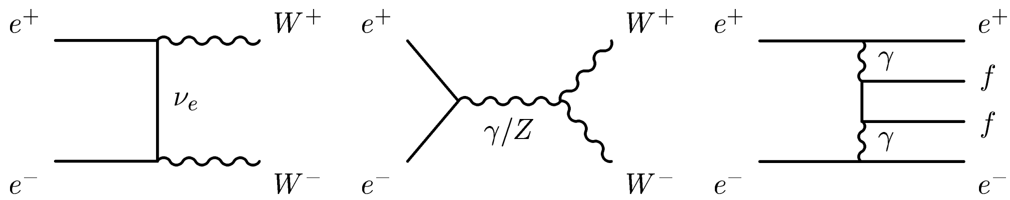

Figure 2.3: 4-fermion processes: W^+W^- pair production in the t- and s-channel where each W boson decays either into a quark pair or a lepton pair, and the two-photon production (multi-peripheral)

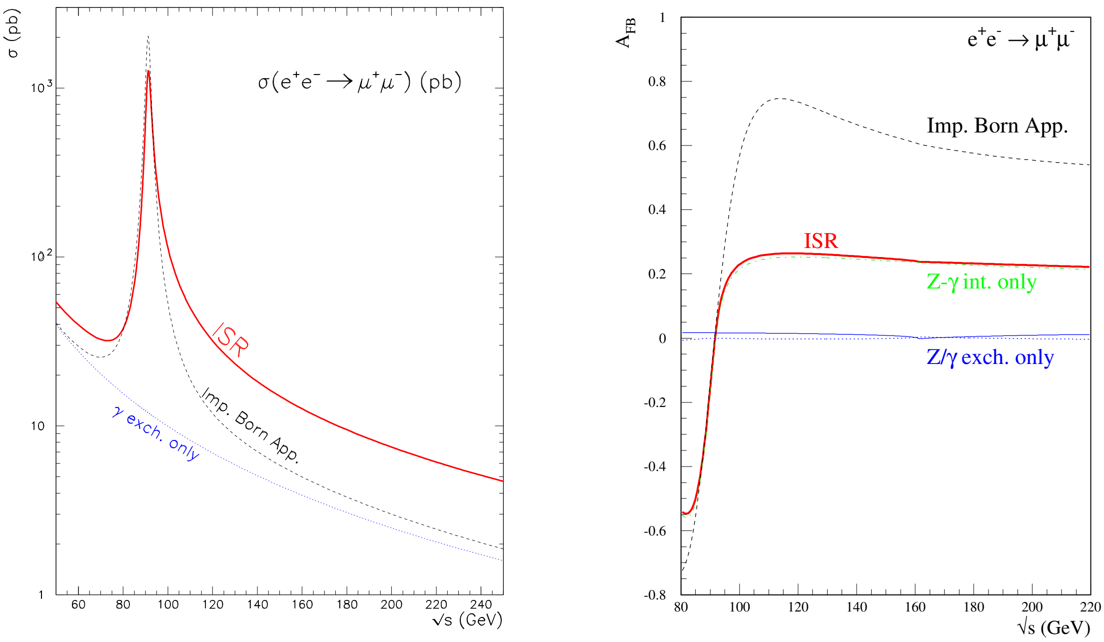

Figure 2.4: The cross section and forward-backward asymmetry for the process $e^+e^- \to \mu^+\mu^-(\gamma)$ as a function of $\sqrt{s}$ before and after ISR convolution

The forward-backward asymmetry is defined by

$$A_{FB} = \frac{\sigma_F - \sigma_B}{\sigma_F + \sigma_B} \quad , \tag{2.26}$$

where

$$\sigma_F = 2\pi \int_0^1 d(\cos\theta)\frac{d\sigma}{d\Omega} \, , \qquad \sigma_B = 2\pi \int_{-1}^0 d(\cos\theta)\frac{d\sigma}{d\Omega} \quad . \tag{2.27}$$

Using Equation (2.19) this gives for the asymmetry in lowest order:

$$A_{FB} = \frac{3}{4} \cdot \frac{G_3(s)}{G_1(s) + 2\mu_f G_2(s)} \sqrt{1 - 4\mu_f} \quad . \tag{2.28}$$

While G_1 and G_2 belong to symmetric functions of θ, a non-vanishing G_3 leads to an asymmetry of $A_{FB} \neq 0$. This is the case specially at energies well above the Z resonance where the $Z - \gamma$ interference becomes important (see Figure 2.4). Neglecting the fermion masses and the terms with $(\Gamma_Z/M_Z)^2$ the peak asymmetry is given by

$$A^0_{FB} = \frac{3}{4}\mathcal{A}_e\mathcal{A}_f, \quad \text{with} \quad \mathcal{A}_f = \frac{2v_f a_f}{v_f^2 + a_f^2}, \tag{2.29}$$

which allows a precise measurement of the Weinberg angle.

Radiative Corrections

The parameters given in the previous section are obtained at tree level and are modified in higher orders of perturbation theory. Radiative corrections have to be taken into account that include higher order diagrams. As mentioned above, due to divergences in the loop integrals the parameters have to be redefined. With the on-shell renormalisation scheme the corrections are divided into the following subclasses.

QED Corrections consist of those diagrams with an extra photon added to the Born diagrams either as a real bremsstrahlung photon or a virtual photon inside a loop, see Figure 2.5. The main parts of real photon radiation are: the initial state radiation (ISR), the final state radiation (FSR), initial and final state quark- and lepton-pair production and the initial-final (IF) QED interference. At energies near the Z mass the radiation of soft photons leads to a 74% reduction of the cross section, whereas at energies $>$ 100 GeV this quantity more than doubles in comparison to the Born level due to photon emission (see Figure 2.4). In the latter case, the dominating contribution is the ISR with a collinear emission of a hard photon. This leads to a reduction of the effective center-of-mass energy before collision. As the cross section at the Z resonance is high, in most cases (40-70%, depending on the final fermion type) $\sqrt{s'}$ is reduced down to the peak energy, thus called *Z returns*.

The correction is done by convoluting the Born cross section with a radiator function $G(x = s'/s)$ that describes the probability of photon radiation [6]:

$$\sigma(s) = \int_{x_0}^{1} dx \cdot \sigma_B(sx) \cdot G(x), \quad \text{with} \quad x_0 = 4m_f^2/s \quad , \tag{2.30}$$

where $G(x)$ can be interpreted as a probability density function for the emission of a photon.

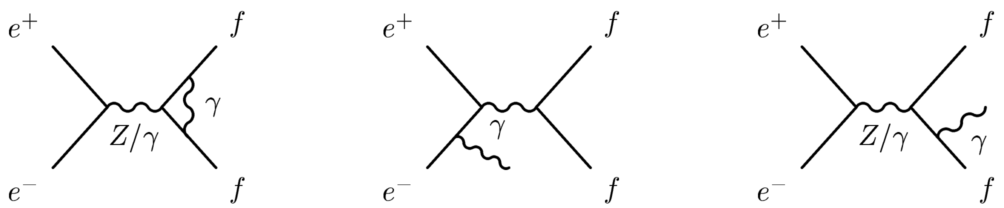

Figure 2.5: Examples of virtual and real (initial and final) photon corrections for $\mathrm{e^+e^-} \to \mathrm{f\bar{f}}$

Weak corrections include all other diagrams with corrections to vector boson propagators, vertex corrections and box diagrams with two massive boson exchange, see Figure 2.6. The weak corrections include the more subtle part beyond tree level as they can be mimicked by virtual effects of new physics. The redefinition of parameters via on-shell renormalisation provides for the validity of Equation (2.18) such that other quantities can be expressed in terms of $\mathrm{M_Z}$, $\mathrm{M_W}$ and α. In contrast to energies near the Z, the box contributions become important above the WW production threshold. For example, at $\sqrt{s}$= 205 GeV the effect of weak boxes on $\sigma_{\mu\mu}$ is $\approx$ 1.5%.

The theoretical uncertainty on the calculations for quantities measured at LEP II is dominated by the QED part of radiative corrections, mainly by the initial state radiation, and is

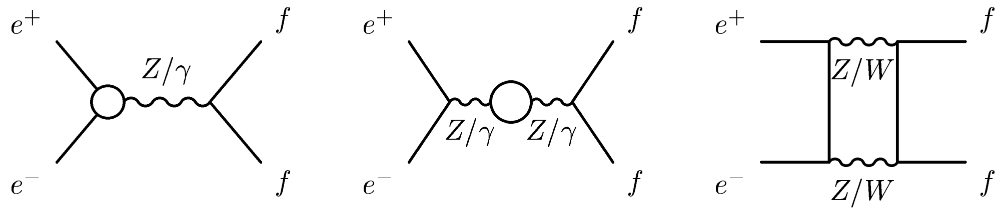

Figure 2.6: Examples of weak (vertex, propagator and box) corrections, for $e^+e^- \to f\bar{f}$

estimated to be 0.4% [7]. QCD corrections are only small in this sector, mainly playing a role in quark-pair production and therefore not discussed here. A detailed description of all corrections can be found in [6].

2.2 Beyond the Standard Model

In the last decades the Standard Model predictions have been confirmed in many experiments to a very high level of precision. There remain, however, a number of unanswered questions that can non be explained by this theory. These include:

- The relatively large number of free parameters in the Standard Model that have to be determined experimentally
- The origin of the fermion masses that is explained with the Higgs field and its referring Higgs boson, but which has not yet been discovered
- The origin of electroweak symmetry breaking
- The different strength of the coupling constants referring to the four fundamental forces that may converge at a very high energy scale ($\simeq 10^{15}$ GeV) as predicted in GUTs[1].
- The gravity has not been incorporated as a quantum field theory
- The hierarchy problem due to the fact that the mass scale for electroweak interactions is so different from the Planck mass, $M_{EW} \ll M_{Planck}$, with $M_{EW} \sim \mathcal{O}(M_W)$ and $M_{Planck} \sim \mathcal{O}(10^{19}\text{GeV})$.
- The increasingly strong evidence of neutrino masses and oscillations

Therefore, the Standard Model is believed not to be the final theory, and that there must be new physics underlying it. Some of the most-favoured solutions are:

- Supersymmetry
- Extra Dimensions
- String Theory

[1] Grand unifying theories

There are several hints that these possible new effects may be measurable at $\mathcal{O}$(TeV) scale. For example, in a supersymmetric theory, which could solve the hierarchy problem, there are equal numbers of bosons and fermions with identical couplings. As none of the known fermions can be paired with the known bosons because of their difference in internal quantum numbers, new particles have to be introduced, e.g. quark $\rightarrow$ squark, photon $\rightarrow$ photino, Higgs $\rightarrow$ Higgsino. For similar masses ($\leq$ 1 TeV) of the supersymmetric partners (spartners) the one-loop corrections are small and remove the divergences, which is the best motivation to find supersymmetry at low energies. There are as well phenomenological hints that supersymmetry may appear at low energies: the strength of the gauge interactions unify as predicted in GUTs consistent with the values of the electroweak parameters, if supersymmetry is included; the minimal supersymmetric extension of the Standard Model (MSSM) is consistent with a relatively light Higgs mass ($\leq$ 200 GeV) [8] preferred from precision electroweak data.

The search for new physics phenomena can be performed either directly by seeking for a clearly given experimental signature or in an indirect way by probing its virtual effects. The former requires a sufficient production energy and a good separation from known SM processes that can mimic the decay products. In the latter case, the measured quantity in an experiment is compared to its prediction from the SM, deviations are interpreted with respect to possible new physics interactions. Those can be probed by fitting certain models containing one or more new parameters to the data obtained by the measurements. If no evidence for the existence is found, upper or lower limits on the parameters at a certain confidence level can be derived.

2.2.1 Predictions from a Z$'$ Boson

In many extensions beyond the Standard Model the existence of additional heavy gauge bosons is predicted. In the presence of one extra Z, a so-called Z$'$ boson, the Lagrangian which describes the neutral current extends to the form:

$$\mathcal{L} = eA_\mu J^\mu_\gamma + g\mathrm{Z}^\mu_0 J^\mu_{\mathrm{Z}_0} + g'\mathrm{Z}'^\mu_0 J^\mu_{\mathrm{Z}'_0} \tag{2.31}$$

with the neutral currents

$$J^\mu_n = \sum_f \bar{f}\gamma^\mu[v_f(n) + \gamma_5 a_f(n)]f, \quad n = \gamma, \mathrm{Z}_0, \mathrm{Z}'_0, \tag{2.32}$$

and the coupling constants, g and g', being defined for the symmetry eigenstates Z_0 and Z'_0.

Generally, the mass eigenstates Z and Z$'$, which are the observed particles, will be formed by the mixing of the symmetry eigenstates:

$$\begin{pmatrix} \mathrm{Z} \\ \mathrm{Z}' \end{pmatrix} = \begin{pmatrix} \cos\theta_{\mathrm{ZZ}'} & \sin\theta_{\mathrm{ZZ}'} \\ -\sin\theta_{\mathrm{ZZ}'} & \cos\theta_{\mathrm{ZZ}'} \end{pmatrix} \begin{pmatrix} \mathrm{Z}_0 \\ \mathrm{Z}'_0 \end{pmatrix}, \tag{2.33}$$

with $\theta_{\mathrm{ZZ}'}$= mixing angle between the Z_0 and Z'_0. As the renormalisation is performed on mass shell, these masses have to be distinguished, where the lighter Z is identified with the Z resonance. Z_0 denotes the Standard Model Z boson with its mass $\mathrm{M_{SM}}$. From $\mathrm{M_{SM}} \leq \mathrm{M}_{\mathrm{Z}'_0}$ it follows that the Z mass $\mathrm{M_Z}$ is reduced compared to the SM prediction due to the mixing and $\mathrm{M}_{\mathrm{Z}'} > \mathrm{M}_{\mathrm{Z}'_0}$ [9].

$\mathrm{M_{SM}}$ can be obtained for each set of the model parameters, $\mathrm{M_{Z'}}$ and $\theta_{\mathrm{ZZ'}}$, and $\mathrm{M_Z}$:

$$\tan^2\theta_{\mathrm{ZZ'}} = \frac{\mathrm{M^2_{SM}} - \mathrm{M^2_Z}}{\mathrm{M^2_{Z'}} - \mathrm{M^2_{SM}}} \quad \Leftrightarrow \quad \mathrm{M^2_{SM}} = \mathrm{M^2_Z}\cos^2\theta_{\mathrm{ZZ'}} + \mathrm{M^2_{Z'}}\sin^2\theta_{\mathrm{ZZ'}}. \tag{2.34}$$

In the usual relation between $\mathrm{M_Z}$ and $\mathrm{M_W}$ and the Weinberg angle, $\mathrm{M_Z}$ has to be replaced by the mass before mixing:

$$\mathrm{M_{SM}} = \frac{\mathrm{M_W}}{\cos\theta_W} \tag{2.35}$$

The couplings for the mass eigenstates to the fermions are modified as follows:

$$v_f(\mathrm{Z}) = \cos\theta_{\mathrm{ZZ'}} v_f + \frac{g'}{g}\sin\theta_{\mathrm{ZZ'}} v'_f, \tag{2.36}$$

$$v_f(\mathrm{Z'}) = \cos\theta_{\mathrm{ZZ'}} v'_f - \frac{g}{g'}\sin\theta_{\mathrm{ZZ'}} v_f, \tag{2.37}$$

and analogue definitions for the axial vector couplings, with

$$g = (\sqrt{2}\,G_\mu \mathrm{M_Z}^2)^{1/2}, \quad v_f = a_f(1 - 4|Q_f|\sin^2\theta_W), \qquad a_f = I_3^L(f). \tag{2.38}$$

and a_f, v_f and a'_f, v'_f being the couplings of the unmixed eigenstates, $\mathrm{Z_0}$ and $\mathrm{Z'_0}$.

Because of the large number of possible couplings to fermions it is easier to consider specific models where the couplings are defined as described in the following.

E_6 and L-R Models

In GUT theories the symmetry groups of the Standard Model are embedded in larger groups. In many cases this leads to extra U_1 groups when the symmetry is broken, such as in the $\mathrm{E_6}$ models [9], [10]:

$$\begin{array}{rclcl} \mathrm{E_6} & \rightarrow & \mathrm{SO(10)} & \times & \mathrm{U(1)}_\psi \\ \mathrm{SO(10)} & \rightarrow & \mathrm{SU(5)} & \times & \mathrm{U(1)}_\chi, \end{array}$$

in which the SU(5) contains the standard $\mathrm{SU(3)}_c \times \mathrm{SU(2)}_L \times \mathrm{U(1)}$. In this way two gauge groups, $\mathrm{U(1)}_\chi$ and $\mathrm{U(1)}_\psi$, are introduced. The observed particles will be mixed states of these groups via:

$$\mathrm{Z'_0} = Z_\psi \sin\theta_{E6} + Z_\chi \cos\theta_{E6}, \tag{2.39}$$

with θ_{E6} being the free parameter of the model. Three special cases are considered: $\theta_{E6} = 0$ (χ model), $\theta_{E6} = \pi/2$ (ψ model) and $\theta_{E6} = -\arctan(5/3)$ (η model). The latter emerges in a particular $\mathrm{E_6}$-breaking that is motivated by some superstring-inspired models.

In the L-R model the Standard Model is extended to the $\mathrm{SU(2)}_R \times \mathrm{SU(2)}_L \times \mathrm{U(1)}_Y$, with an extra $\mathrm{Z'}$ that couples to the current [11], [12]:

$$J_{LR} = \alpha_{LR}\; J_{3R} - \frac{1}{2\alpha_{LR}} J_{B-L}, \tag{2.40}$$

where J_{3R} is the third component of $\mathrm{SU}(2)_R$ and B (L) is the baryon (lepton) number. J_{3R} is constructed such that all right-handed fermions are doublets and all left-handed fermions are singulets. In Equation (2.40) α_{LR} is:

$$\alpha_{LR} = \left(\frac{\cos^2 \theta_W}{\sin^2 \theta_W} \frac{g_R^2}{g_L^2} - 1 \right)^{1/2} \tag{2.41}$$

where $g_{L,R}$ are the gauge couplings of the $\mathrm{SU}(2)_{L,R}$. α_{LR} is limited to $\sqrt{(2/3)} \leq \alpha_{LR} \leq \sqrt{\cot^2 \theta_W - 1}$ by theory. Special cases are $\alpha_{LR} \simeq 1.53$ where $g_R = g_L$, the manifestly L-R symmetric model, and $\alpha_{LR} = \sqrt{2/3}$ which reproduces the E_6 χ model.

In most versions of symmetry breaking to the $\mathrm{SU}(2)_R$ the $\mathrm{Z}'_{\mathrm{L,R}}$ acquires a large mass scale ($10^{10} - 10^{11}$ GeV) and is not relevant at a low scale (~ 1 TeV). However, the model is interesting, because it can occur in models, besides the SO(10), with more complicated symmetry-breaking patterns.

As an example, the Z' couplings to leptons arising from the E_6 models and the L-R model are given in Table 2.2.

l	$g'_{v_f} / \sin \theta_{\mathrm{W}}$	$g'_{a_f} / \sin \theta_{\mathrm{W}}$
E_6	$2/\sqrt{6} \cos \theta_{E6}$	$1/\sqrt{6} \cos \theta_{E6} + \sqrt{10}/6 \sin \theta_{E6}$
L-R	$1/\alpha_{LR}$ - $\alpha_{LR}/2$	$\alpha_{LR}/ 2$

Table 2.2: The Z' couplings to leptons given as a function of $\cos \theta_{E6}$ for the E_6 models and as a function of α_{LR} for the L-R model [13].

Finally, a heavy Z' boson with the same couplings as for the standard Z is considered in the so-called *sequential* Standard Model (SSM). Such couplings are not very likely in extended gauge theories, but are a useful reference point for the sensitivity of the experiments. It could also play an important role as an exited state of the SM Z boson in models with extra dimension at the weak scale.

2.2.2 Quantum Gravity in large extra Dimensions

Theories of quantum gravity in extra spatial dimensions have been studied very actively during the last few years. It has been shown that the effective Planck scale at which gravitation gets strong can be reduced to $\mathcal{O}(1$ TeV) (low scale quantum gravity). Theories including extra spatial dimension are strongly related to *string* theories in which the point-like particles are replaced by one-dimensional extended objects, called *strings*, that can oscillate in different modes. Due to the very small extension ($\approx 10^{-35}$ m) they cannot be observed. All particles of the Standard Model, fermions and bosons, and the graviton can be described by different vibration patterns of the oscillating strings, each representing the specific properties of the particle observed (like the mass, charge etc.). Analogue to the forces strings can interact while connecting or disconnecting to each other potentially changing their particular vibration pattern. A plain introduction to string theory can be found in [14]. The string theory has the strong capacity to unify the Standard Model interactions and the gravity, but it has the requirement of extra spatial dimensions. In modern string theories eleven dimensions in spacetime (10 spatial + 1 time) are introduced.

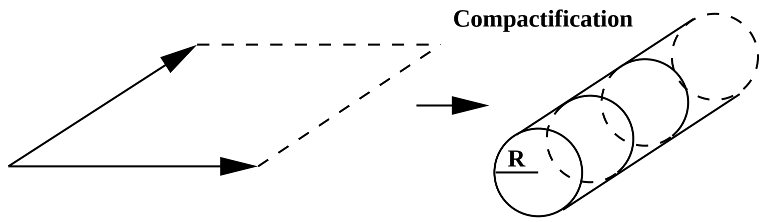

Figure 2.7: Compactification of a two-dimensional space into a cylinder with radius R.

Kaluza-Klein Theory

The idea of extra dimensions existing additional to our 4 dimensional space time is not completely new. In 1919, Theodor Kaluza developed a mathematical formalism that described Einstein's gravity in five dimensions by adding one additional imaginary dimension in space. Amazingly, as a solution of this the exact maxwell equations emerged. It seemed as if electromagnetism can be derived from gravity or at least both were of the same origin. However, we live in 4 dimensional space time and no one has ever observed more than that. A possible explanation was made by Oskar Klein in 1926 who supposed the extra dimensions to be very small and somehow compactified such that they can not be observed. They only become "visible" at very low distances of the size L that can be simply the radius of a circle, see Figure 2.7.

Generally, the four-dimensional Minkowski space-time could be embedded in a D-dimensional space-time: $M^4 \times X^{D-4}$ with (D-4) extra dimensions. Combining this geometry with quantum mechanic wavefunctions assuming the lowest order of space expansion, (4+1) dimensions, Kaluza and Klein developed a compactified theory [15] which consists of a single massless and an infinite number of massive complex scalar fields and a massless gauge field, the so-called Kaluza-Klein modes. For the masses hold the relation $m_k^2 = k^2/L^2$ $(k = 0, 1, 2, ..., \infty)$, the KK Tower of massive gravitons. At low energies only the zero mode is essential, for high energies, $E > 1/L$, all the KK modes become important. The compactification yields to a quantisation of the momentum corresponding to the compactified coordinate. As a consequence, a relation between the Planck mass and the compactification radius was found [16]: $M_{Pl}^2 = M_*^3 \pi L$, where $M_{Pl} = 1/\sqrt{G_N}$ and M_* is the scale of gravity.

The theory of Kaluza-Klein seems to be very successful in unifying the 4 dimensional gauge and gravitation fields to a common 5 dimensional gravitation field. However, due to significant inconsistencies, e.g. the predicted value for e/m_e was far away from the measurement, the Kaluza-Klein theory was not pushed forward.

Framework of ADD

The concept that our (3+1)-dimensional world could lie on a surface of a higher dimensional space was discussed in the context of general relativity already since 1960. Our real"3D world is then described as a braneworld in which our Standard Model particles (and fields) can be localized. The idea to combine this braneworld and the KK compactification of extra dimensions was proposed recently by Arkani-Hamed, Dimopoulos and Dvali (ADD) [17]. The main concept of ADD is as follows:

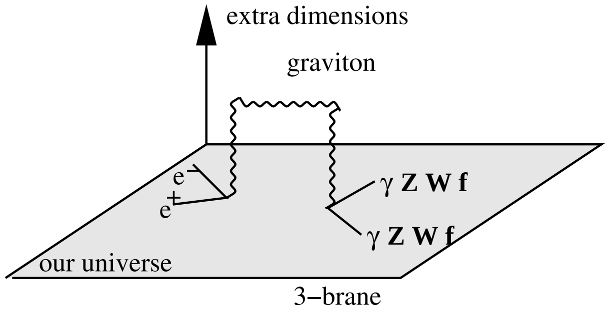

Figure 2.8: The propagation of gravitons in the extra dimensions (the bulk) illustrated with a two-dimensional plane being our three-dimensional universe (3-brane), a wall to which the SM particles and fields are confined.

- The SM particles are bound to the 3-brane, whereas the gravity can propagate in all (4+n) dimensions, called the bulk
- The fundamental scale of gravity, M_*, is of the order 1 TeV
- The n extra dimensions are compactified

In this case, the hierarchy problem is avoided and the gravitational interactions become strong near the weak scale. Gravity, thus, appears to be weak only in the ordinary (3+1) space time as we observe only its projection from the higher dimensional space onto the wall. The KK tower of massive gravitons can interact with the SM fields on the wall. The simple force law has then to be modified to:

$$F_{(4+n)}(r) = G_{N(4+n)} \frac{m_1 m_2}{r^{n+2}}, \tag{2.42}$$

where $G_{N(4+n)}$ is the Newton constant in (4+n) dimensions [18]. For distances between both masses greater than the size of the compactified dimension, the usual $\frac{1}{r^2}$ force law is obtained. The (4+n) dimensional Gauss' law gives the relation between $G_{N(4+n)}$ and $G_{N(4)}$:

$$G_{N(4)} = \frac{S_{(3+n)}}{4\pi} \frac{G_{N(4+n)}}{V_n}, \tag{2.43}$$

where S is the surface area in (3+n) spatial dimensions and $V_n = L^n$ is the volume of the compactified dimensions. Using $M^{n+2}_{Pl(4+n)} = 1/(G_{N(4+n)}\, S_{(3+n)})$, the relation between the effective Planck scale $M_{eff} = M_{Pl(4+n)}$, the fundamental scale where gravity becomes strong, and M_{Pl} is derived:

$$M^2_{Pl} \sim R^n M^{2+n}_{eff}, \tag{2.44}$$

where R is the size and n the number of the extra dimensions. Assuming M_{eff} to be near 1 TeV yields to $R \sim 10^{30/n-17}$ cm. For $n = 1$, $R \sim 10^{13}$ cm which is excluded as this would be too large. For $n = 2$, $R \sim 1$ mm which is the level of precision for the measurement of gravitational force at present. For $n = 7$ (the maximum suggested by M-theory), R becomes about 1 fm, which is still large compared to $(M_{Pl})^{-1}$.

It has been recently shown that this framework can be embedded in string theories, where the effective Planck scale can be identified with the string scale M_s [18] as the ADD model represents the lower energy limit of the string scale. Besides the ADD model alternate theories exist including low Planck or string scale. Those are not considered here, examples can be found in [20].

Phenomenology

The spin-2 graviton can manifest itself in the following processes in the e^+e^--annihilation:

1. $e^+e^- \to (\gamma/Z)\, G$
2. $e^+e^- \to G \to \gamma\gamma$
3. $e^+e^- \to G \to f\bar{f}$

In the first process a real graviton is produced which escapes into the extra dimensions leaving an amount of missing energy according to its invisible particle mass. The total cross section of this reaction is inversely proportional to the effective Planck mass M_{eff} and thus dependent on the number of extra dimensions. Process (2) and (3) include a virtual graviton exchange in the s-, t- and u-channel. As this analysis deals with process (3), the fermion-pair production, the others shall not be not followed up here.

The process $e^+e^- \to f\bar{f}$ provides strong bounds on the effective Planck scale which is independent on the number of extra dimensions. The approach to the virtual graviton exchange outlined here follows closely the notation of J. Hewett [21]. The spin-1 KK states do not interact with SM fields on the wall and the scalar does not contribute to the process addressed here. Thus, only the interactions of spin-2 gravitons in the KK tower to the SM fields, which couple in an identical manner, have to be considered. As the summation over all states of the KK tower causes ultraviolet divergences - the distance is given by $\sim 1/r$ -, a cut-off must be introduced which is taken to be the scale of the new physics. For $n > 2$ the scale is defined as the string scale $\mathrm{M_s}$.

The angular distribution for the fermion-pair production including s-channel spin-2 graviton exchanges can be expressed as:

$$\begin{aligned} \frac{d\sigma}{dz} &= N_c \frac{\pi\alpha^2}{2s}\beta(P_{ij}(A^e_{ij}A^f_{ij}(1+\beta^2 z^2) + 2\beta B^e_{ij}B^f_{ij}z + A^e_{ij}C^f_{ij}(1-\beta^2)) \\ & -\frac{\lambda s^2}{2\pi\alpha \mathrm{M_s^4}} P_i(2\beta^3 z^3 v^e_i v^f_i - \beta^2(1-3z^3)a^e_i a^f_i) \\ & +\frac{\lambda^2 s^4}{16\pi^2\alpha^2 M_s^8}(1 - 3\beta^2 z^2 + 4\beta^4 z^4 - (1-\beta^2)(1-4\beta^2 z^2))), \end{aligned} \tag{2.45}$$

where i, j sum over γ and Z exchange, $z = \cos\theta$, $\beta = (1 - 4m_f^2/s)^{1/2}$, $A^f_{ij} = (v^f_i v^f_j + a^f_i a^f_j)$, $B_{ij} = (v^f_i a^f_j + v^f_j a^f_i)$, $C_{ij} = (v^f_i v^f_j - a^f_i a^f_j)$, P_{ij} and P_i are the usual propagator factors, $P_\lambda = P_{\lambda\lambda} = 1$, $P_Z = P_{Z\lambda} = P_{\lambda Z} = s(s-m_Z^2)/((s-m_Z^2)^2 + m_Z^2\Gamma_Z^2)$, $P_{ZZ} = s^2/((s-m_Z^2)^2 + m_Z^2\Gamma_Z^2)$.

A parameter is defined that is $\epsilon = \lambda/\mathrm{M_s^4}$. Terms including ϵ are due to the new interaction: ϵ^2 describes the pure graviton exchange, ϵ the interference with the SM bosons (γZ). The coefficient λ which is of $\mathcal{O}(1)$ is dependent on the number of extra dimensions and how they are compactified, as well as on the energy. However, the dependence is only weak with respect to the level of precision expected for the limits ($\sim |\lambda|^{1/4}$) and will be taken as one, with both choices of sign. Its precise value can only be calculated with the full knowledge of quantum gravity theory. Integrating over $\cos\theta$ the second term vanishes, therefore, the total cross section for fermion-pair production does not change up to terms of order s^4/M_s^8, independently of fermion flavor, and thus, only the angular distribution can give a measurable effect from virtual graviton exchange.

Chapter 3

The Experiment

3.1 The LEP Accelerator

The large electron positron collider LEP at CERN, a circular accelerator of 27 km circumference, was operating successfully during the years 1989 to 2000. The LEP tunnel was located near to the Lake Geneva close to the border of Switzerland and France, installed $100 - 150\,\mathrm{m}$ below the ground. The four LEP experiments - ALEPH, DELPHI, L3 and OPAL- were situated in four different interaction points (IP) for detecting the out-coming particles in the e^+e^- annihilation. A schematical outline of the accelerator and the experiments can be found in figure 3.1. From the start of operation in 1989 until 1995, LEP was running with a center-of-mass energy close to the Z resonance (87-95 GeV), the LEP I operation period. The second operation period - LEP II - started in autumn 1995 where the energy for the first time was increased to 130-140 GeV. In 1996 the energy was high enough to produce a W pair ($\approx 161\,\mathrm{GeV}$), which measurement was a main goal of the LEP programme. In the following years the energy was continuously increased up to 209 GeV in 2000, the highest ever reached energy in a e^+e^- collider.

LEP accelerated bunches of electrons and positrons in a single vacuum beam pipe. Before the bunches were injected into LEP, their energy was increased successively up to approximately 20 GeV by a system of smaller accelerators (LINAC, PS, SPS)[1]. In LEP the counter-rotating particles passed every turn through more accelerating sections. Their circular path was bent by the magnetic fields in bending magnets. While the particles gained energy the fields in the magnets had to be raised synchronously. During the injection and acceleration phase the beams had to be separated at the IPs to avoid undesired collisions or interactions with the detectors before reaching the nominal energy. The operation cycle between the filling to LEP, acceleration, colliding the beams for data taking and by the time the beam was lost or dumped after collisions was called a *fill*. Typically, the duration of a fill at LEP II was about 2-5 hours.

The parameters of lepton storage rings are determined by the synchrotron radiation due to the transverse acceleration during deflection in the bending magnets. The corresponding energy loss per particle and per turn is:

$$\Delta U = \frac{4\pi}{3} \cdot \frac{r_e\, m_0\, c^2\, \gamma^4}{\rho}, \tag{3.1}$$

[1]Linear Accelerator, Proton Synchrotron, Super Proton Synchrotron

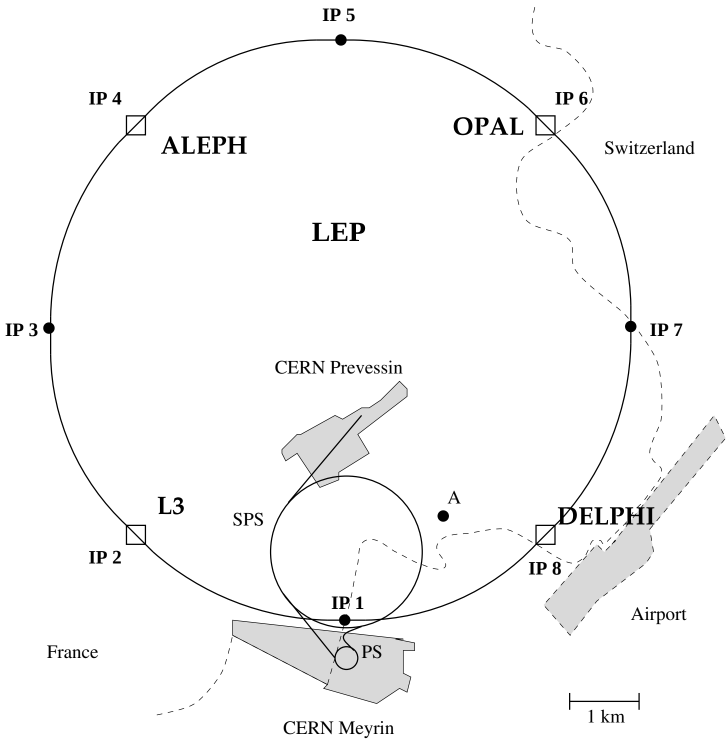

Figure 3.1: A schematical view of the LEP accelerator and the four experiments

where

$$\begin{aligned} r_e &= \text{classical electron radius} \\ m_0 &= \text{mass of the electron} \\ \gamma &= \text{relativistic factor} \\ \rho &= \text{radius of the curvature (LEP: } \rho = 3096 \text{ m),} \end{aligned}$$

which scales with the fourth power of the energy. For example, the loss per turn is $\approx$ 120 MeV at a beam energy of 46 GeV and 2000 MeV at 90 GeV. These energy losses have to be compensated by more revolution frequency (RF) power. At LEP I the maximum RF voltage was 340 MeV with a maximum energy of $\approx$ 55 GeV. Due to the required energies at LEP II more RF cavities had to be installed. The achieved RF voltages and corresponding energies for this period are shown in figure 3.2 .

The determination of the beam energy at LEP I was performed directly at the physics operating energy, after the collision period, by resonant depolarisation which resulted to an uncertainty on the Z boson properties ($\mathrm{M_Z}, \Gamma_\mathrm{Z}$) of $\sim$ 1 MeV [22]. At LEP II the transverse polarisation was not sufficient, therefore, above 80 GeV the beam energy was derived from continuous measurements of the bending fields by 16 NMR probes located in dipole magnets around the LEP ring. These are calibrated assuming a linear relationship between the NMR field and the the beam energy from resonant depolarisation in the region 40-60 GeV. From

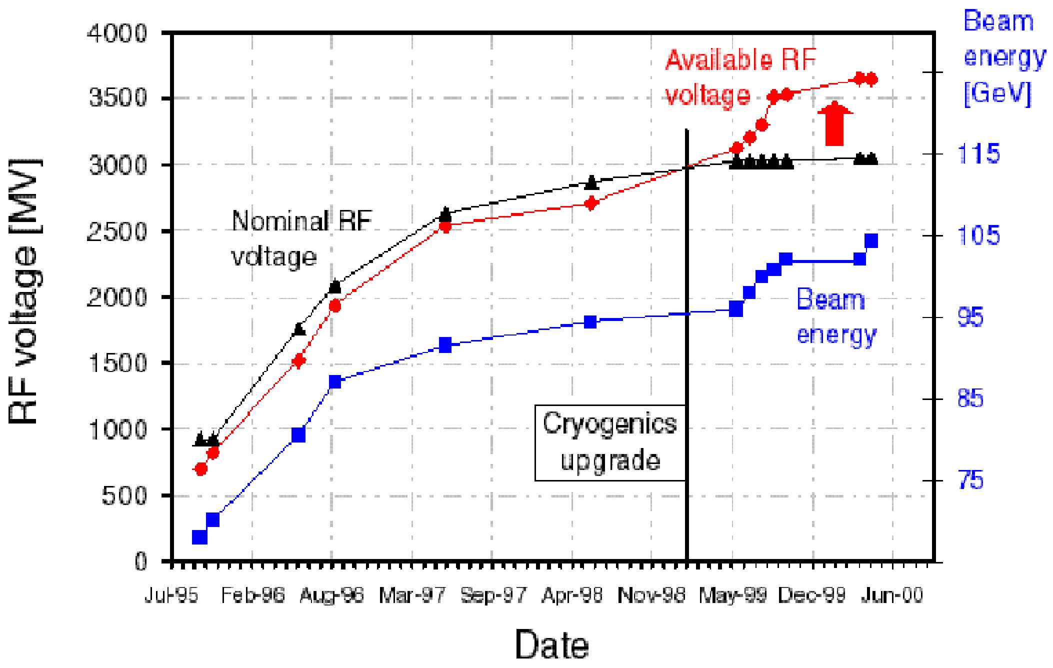

Figure 3.2: The nominal and available RF voltage and energy at LEP II

this method the uncertainty on E_b was determined to be 20-30 MeV during the different years at LEP II [23]. This is an important contribution to the error on the W mass measurement.

Besides the energy, the important parameter of a collider is the luminosity which is given by:

$$\mathcal{L} = \frac{I_{b^2}\, N_b\, f_0}{4\pi\, \sigma_x\, \sigma_y} \tag{3.2}$$

where

$$\begin{aligned} I_b &= \text{intensity per bunch} \\ N_b &= \text{number of bunches per beam} \\ f_0 &= \text{revolution frequency } (\sim 11 \text{ kHz}) \\ \sigma_{x,y} &= \text{horizontal and vertical beam sizes} \end{aligned}$$

During LEP I the collider operated in the “Pretzel” scheme with four and eight (since 1992) bunches per beam. Each of the eight bunches of electrons and positrons were equally spaced around the ring and collided at each of the four IPs. In order to improve the achievable luminosity, the mode of operation since 1995 was changed to the *bunch train mode* where four equally spaced trains of up to four bunches crossed at each IP. The thus achieved luminosity reached 10^{32} s^{-1}cm^{-2}. The integrated luminosities from 1989 to 2000 are illustrated in figure 3.3.

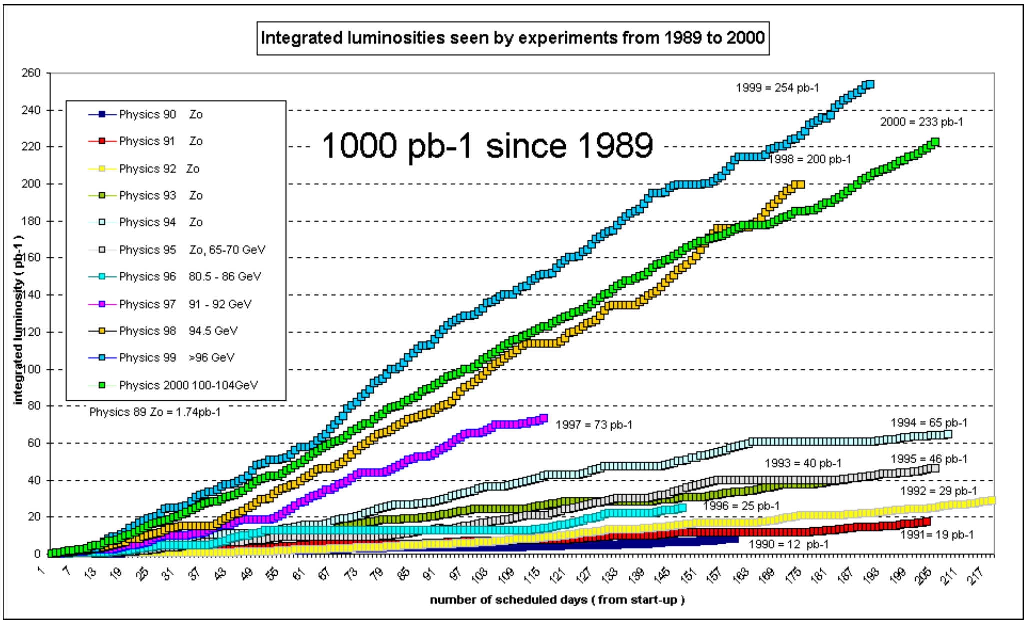

Figure 3.3: Integrated luminosities for all years of data taking at LEP

3.2 The DELPHI Detector

DELPHI (DEtector with Lepton, Photon and Hadron Identification) was one of the four large detectors at the LEP collider that measuredthe out-coming particles in the e^+e^- annihilation. The DELPHI detector was designed for a high granularity over a wide angular range. A characteristic feature was its powerful particle identification. The detector consisted of several subdetectors which were arranged cylindrically around the beam axis, the "barrel" region ($\sim 40°$ to $140°$), and at the very "forward" region, the end-caps. A schematical outline of the detector is shown in Figure 3.4. It is convenient to use a local reference system to describe the coordinates of a particle. The DELPHI coordinate system is chosen such that the z-axis is along the the beam pipe, the y-axis points towards and the x-axis points towards the center of LEP. The angle to the z-axis is defined as the polar angle θ, the angle in the x-y plane around the z-axis is the azimuth angle ϕ. The radial coordinate is $R = \sqrt{x^2 + y^2}$. A brief review of the detector components relevant to this analysis is given in the following sections. A more detailed description of the DELPHI detector including particle identification can be found in [24].

3.2.1 The Tracking System

The tracking system consisted of several independent subdetectors, which measured the track segments of a charged particle: The Vertex Detector (VD), the Inner Detector (ID), the Time Projection Chamber (TPC) and the Outer Detector (OD) in the barrel region, the Very Forward Tracker (VFT) and the Forward Chambers (FCA and FCB) in the forward regions of the end-caps. The superconducting solenoid provided a highly uniform magnetic field (1.23 T) parallel to the z-axis bending the trajectory of the traversing charged particles. The curvature was used to determine charge and momentum of the particle.

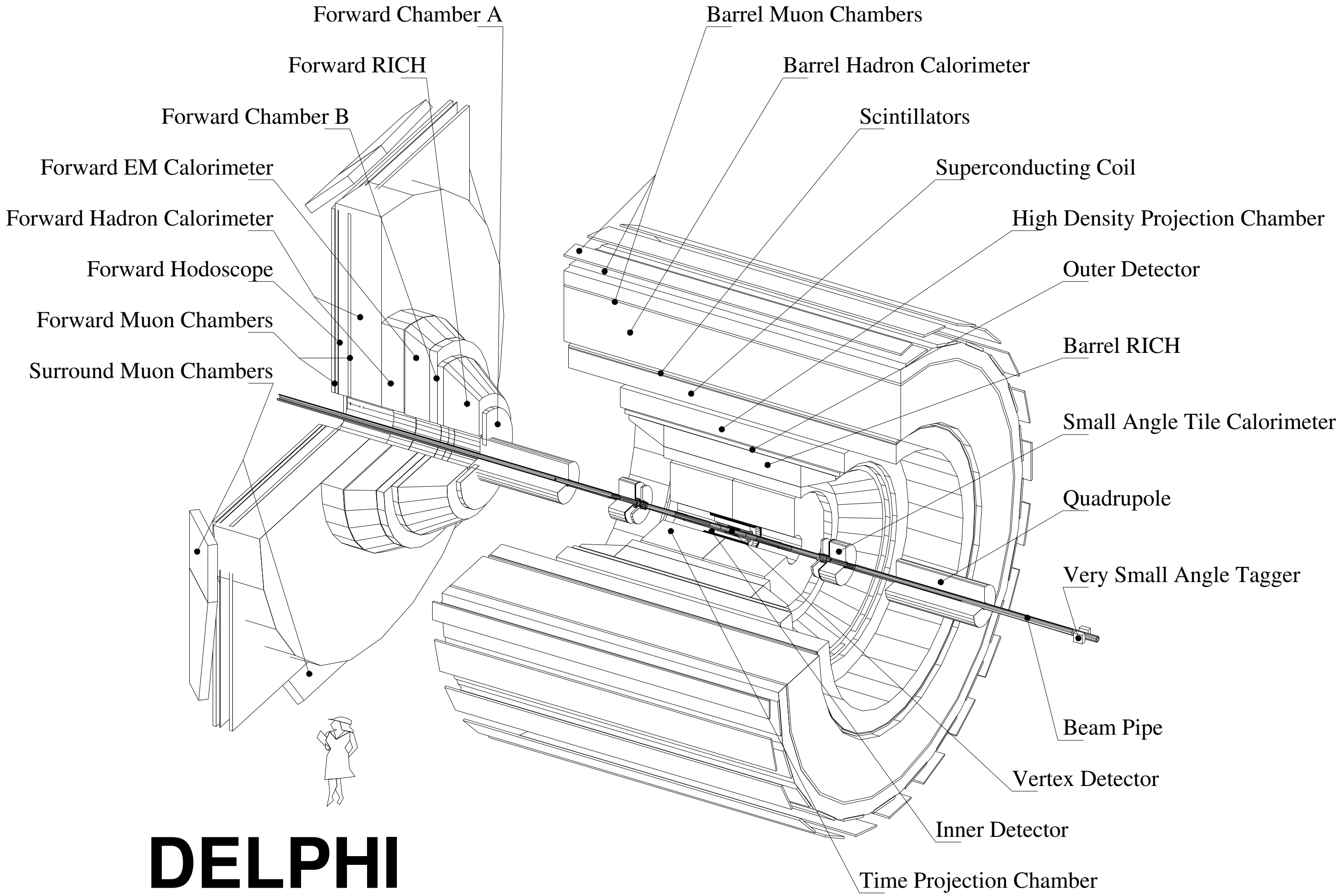

Figure 3.4: A schematical view of the different components of the DELPHI detector

The Silicon Tracker The silicon tracker was the nearest subdetector to the interaction point which provided a very precise reconstruction of primary and secondary vertices with a high spatial resolution (8 μm in $R\phi$ and 10 μm in z in the barrel and 0.1 mm in $R\phi$ in the end caps per hit). The detector, optimised in 1996 for the physics program of LEP II, consisted of a 3-layer microstrip Vertex Detector (VD) in the barrel and the Very Forward Tracker (VFT) in the end-caps, which was composed of two layers of ministrips and two layers of pixel detectors. In total, the detector had a length of 1 m along the beam axis including the repeater electronics, the central part spanned 55 cm. The VD was composed of three concentrical layers placed at average radii of 6.6, 9.2 and 10.6 cm. Each of them contained several modules (20 and 24) mounted in a staggered way to cover overlaps for the full azimuth angle and redundancy. Two of the layers were equipped with double sided microstrip to give both $R\phi$ and z information. The layers of the VFT were inclined with respect to the beam axis in order to cover small polar angles ($< 26°$). The combined silicon detector system covered the polar angles $10° < \theta < 170°$. The silicon tracker had the following sensitives areas: 1.37 m^2 (microstrips), 0.26 m^2 (ministrips) and 0.15 m^2 (pixels, with 1.2 million pixels of the size 330$\times$330 μm).

The Time Projection Chamber The main tracking device in DELPHI was the Time Projection Chamber (TPC). The detector, a cylinder of 3 m length and 0.4-1.2 m radial extension, was located in the barrel and consisted of two separated active drift volumes with an electrical field of 187 V/cm parallel to the z-axis. The drift chambers were filled with a gas (80% Ar, 20% CH_4) which was ionised when a charged particle passed through it. Under the influence of the field, the released electrons drifted to the end plates of the TPC. Both end plates were divided into 6 azimuthal sectors, each provided with 192 sense wires of 20 μm diameter and 16 circular pad rows with constant spacing, see Figure 3.5. This allowed to measure up to 16 space points per particle between the polar angles of $39° \leq \theta \leq 141°$. At least three pad rows were crossed down to polar angles of $20° \leq \theta \leq 160°$. The z coordinate was given by the drift time of the electrons to the wires. The single point precision achieved was 0.25 mm in the $R\phi$ plane and 0.9 mm in z direction. The 192 wires were also used to get the dE/dx information.

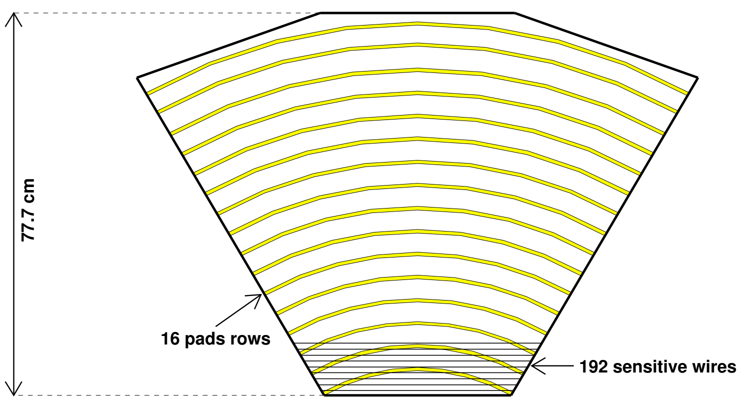

Figure 3.5: One of 12 sectors of the TPC, 6 were on each half.

The Inner and the Outer Detector The Inner Detector (ID) was located between the TPC and the VD. It consisted of an inner drift chamber surrounded by five cylindrical layers of straw tube detectors. The jet chamber was divided into 24 azimuthal sectors, each of them providing up to 24 $R\phi$ points per track between radii of 12 and 23 cm with an average single wire precision of 85 μm. The $R\phi$ measurements of the straw tube detectors (192 tubes per layer) were mainly used for the trigger and resolving of left/right ambiguities inherent in the jet chamber. The polar angle acceptance was $15^\circ \leq \theta \leq 165^\circ$ for both parts. The Outer Detector (OD) was the outmost tracking device in the barrel, located between radii of 197 and 206 cm. It consisted of five staggered layers of drift tubes, operated in the limited streamer mode. In each layer, the adjacent modules of the 24 azimuthal sectors overlapped to provide full azimuthal coverage. The polar angle acceptance was $42^\circ \leq \theta \leq 138^\circ$. Three layers were used to determine the position in z-direction by time measurements at the ends of the anode wires, with a precision of 3.5 cm. The single point precision in $R\phi$ was 0.11 mm

The Forward Chambers The forward chambers A and B (FCA and FCB) provided the tracking in the forward region at polar angles between $11^\circ \leq \theta \leq 36^\circ$ and $144^\circ \leq \theta \leq 169^\circ$. The FCA consisted of three modules that were mounted directly on the TPC end-caps at each side at a distance in |z| of 160 cm. A module was composed of two staggered planes of drift tubes. The wire orientation of the modules was rotated by an angle of 120°. The track elements had a precision of 290 μm in x and 240 μm in y. The FCB - constructed, built and maintained by the Wuppertal group of DELPHI - was a drift chamber with two modules at a distance of $|z| = 275$ cm at each side. Each module consisted of 12 readout planes, coordinates in each of three directions rotated by 120° being defined by four planes. The precision achieved was 150 μm in the x- and y-coordinate. The FCB provided improved momentum resolution in the forward region and, in combination with FCA, a contribution to the trigger.

Momentum Precision In principle, the momentum resolution of a charged particle depends on the precision the curvature of the trajectory introduced by the magnetic field was measured. The curvature ρ is related to the transverse momentum of a charged particle via:

$$p_t = 0.3 \cdot B \cdot \rho \tag{3.3}$$

The resolution of the momentum obtained by the DELPHI tracking system was determined from the inverse momentum spectrum of $Z^0 \to \mu^+\mu^-$ events with a low acollinearity ($< 0.15^\circ$) to remove radiative Z decays. The precise knowledge of the beam energy was taken as the exact value for the momentum expected for those muons. Using information from all barrel detectors (VD, ID, TPC, OD), a width of

$$\sigma(1/p) = 0.57 \times 10^{-3}\ (\mathrm{GeV}/c)^{-1} \tag{3.4}$$

was obtained. In the forward region the resolution was worse, yielding to a width of

$$\sigma(1/p) = 2.7 \times 10^{-3}\ (\mathrm{GeV}/c)^{-1} \tag{3.5}$$

for $\theta < 25^\circ$ and including information from the FCB. The precisions obtained on the track parameters at other momenta can only be estimated by comparing the simulated and reconstructed parameters in a sample of generated Z^0 hadronic decays.

3.2.2 The Calorimeters

The system of calorimetry of the DELPHI detector consisted of the electromagnetic calorimeters for the identification of photons and electrons and the hadron calorimeter (HCAL). The electromagnetic system was composed of a barrel calorimeter (HPC), a forward calorimeter (FEMC), and two very forward calorimeters, the STIC and the VSAT. The latter two were used mainly for the luminosity measurement described in Section 3.2.4.

The High Density Projection Chamber The HPC was located between the OD and the solenoid, covering a polar angle of $43^\circ \leq \theta \leq 137^\circ$. It consisted of 144 modules arranged in 6 rings inside the magnetic field. Each ring was composed of 24 modules coaxially arranged around the beam axis with an inner radius of 208 cm and an outer radius of 260 cm. In principle, each HPC module worked like a small TPC with layers made of lead wires which served as converter material and provided the drift field. The total converter thickness was $18X_0/\sin\theta$. This concept allowed to measure an electromagnetic shower in three dimensions. The energy resolution obtained for 45 GeV electrons was about 6.5%. The relative precision on the measured energy can be parametrised as $\sigma(E)/E = 0.043 \oplus 0.32/\sqrt{E}$. The angular accuracies for high energy photons were ± 1.7 mrad in ϕ and ± 1.0 mrad in θ.

The Forward Electromagnetic Calorimeter The FEMC, placed at $|z| = 284$ cm, provided the electromagnetic calorimetry in the forward region, covering $8^\circ \leq \theta \leq 35^\circ$ and $145^\circ \leq \theta \leq 172^\circ$. It consisted of two arrays of 4532 Cherenkov lead glass blocks of the size 5.0×5.0 cm^2 and a depths of 40 cm. This corresponded to a radiation length of $20X_0$. The Cherenkov photons emitted by the charged particles of the electromagnetic shower were read out by a single stage photomultiplier (triode). The relative precision on the measured energy was parametrised as $\sigma(E)/E = 0.03 \oplus (0.12/\sqrt{E}) \oplus (0.11/E), E$ in GeV. For neutral showers with $E > 2\,\text{GeV}$ the spatial resolution in $|z|$ was ~ 0.5 cm.

The Hadron Calorimeter Hadrons which passed through the electromagnetic calorimeters produced a shower in the HCAL. The HCAL was located in the return yoke of the solenoid between radii of 320-479 cm in the central part and $|z| = 340 - 489\,\text{cm}$ in the forward region. It consisted of two end-caps, each of them composed of 12 sectors, and a barrel part built of 24 modules. More than 19 000 limited steamer tubes were installed in the distances between iron plates of 5 cm thickness. The whole calorimeter covered almost the full solid angle: $11^\circ \leq \theta \leq 169^\circ$. The energy precision was found to be $\sigma(E)/E = 0.21 \oplus 1.12/\sqrt{E}$.

3.2.3 The Muon Chambers

The muon chambers were the outermost subdetectors in DELPHI measuring muons that penetrate the whole detector as a minimise ionising particle. The iron of the hadron calorimeter provided a filter, at first level, to separate muons and hadrons. The latter, mostly, were stopped by this material. The system consisted of the muon chambers in the barrel and the forward (MUB/MUF) and the surround muon chambers (SMC). The SMC were installed in 1994 in order to provide full acceptance in those regions that were not covered by MUB and MUF (at $\theta \approx 45^\circ$ and $\approx 135^\circ$).

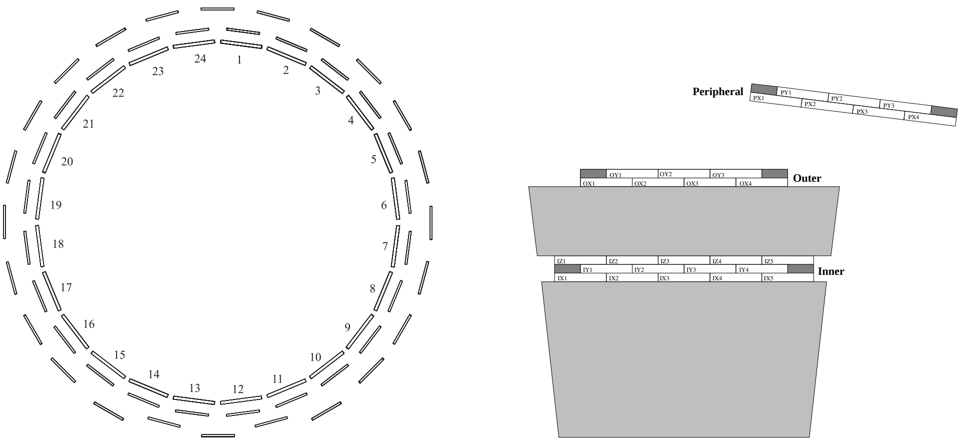

Figure 3.6: The sectors of the barrel muon chamber in the x-y plane.

The Barrel Muon Chambers The MUB was installed at a radius of $\sim$ 445 cm and a distance of $|z| \leq 385$ cm. It consisted of 1372 drift chambers that were arranged in 24 azimuthal sectors and two additional sectors between the legs of DELPHI. Each sector was composed of three modules of chambers, see Figure 3.6. The inner module, embedded in the HCAL material, had three layers, the outer and peripheral modules had two layers of drift chambers. The peripheral modules covered the gaps between adjacent sectors, providing full acceptance in the azimuthal plane. Each drift chamber, filled with 85.5% Ar, 8.5% CH_4, 6% CO_2, was able to provide up to three signals, one anode and two delay line signals. The drift time to the anode inside the chamber gave the distance perpendicular to the sense wires in the $R\phi$ plane with $\sigma(R\phi) = 2$ mm. From the time difference between the two cathode signals, the location in the z-direction was derived with a precision of 80 mm. Except for the gap between the two parts of the MUB at 90°, a full polar angle acceptance between $52° \leq \theta \leq 128°$ was achieved.

The Forward Muon Chambers The MUF was situated in the end-caps of DELPHI at a distance of $|z| \sim 500$ cm. It consisted of two detection planes in each of the two end-caps. Each plane was composed of four modules (quadrants) which contained two layers of 22 drift chambers crossed at 90 degrees. The readout was similar to the that of the MUB, providing three measurements, T_a, T_1 and T_2, giving the coordinates in z and $R\phi$. The accuracy on these coordinates was of the order of 5 mm. The polar angle acceptance was $9° \leq \theta \leq 43°$ and $137° \leq \theta \leq 171°$.

3.2.4 Luminosity Determination

In principle, it is possible to calculate the luminosity in terms of the beam parameters as given in formula (3.2). For the LEP experiments, however, these parameters cannot be determined with a sufficient accuracy needed for a small error on $\mathcal{L}$. Another method is to use a well known process, theoretically and experimentally, that has a high cross section σ compared to other processes. The luminosity can then be determined via the relation: $\mathcal{L} = N/\sigma$, counting the number of events produced and divide by the known cross section. A process that fulfills these criteria is the elastic scattering of electrons and positrons, the Bhabha process. In the

Bhabha process, a photon is exchanged in the t-channel while the energy of the incoming particles is conserved, only the direction of the outgoing particles changes. The cross section of the Bhabha process increases rapidly with lower scattering angles, therefore, the luminosity detectors were placed close to the beam axis, but far away from the interaction point.

The subdetectors at DELPHI that measured the luminosity were the Small Angle Tile Calorimeter (STIC) and the Very Small Angle Tagger (VSAT). The STIC was a lead/scintillator sampling calorimeter placed at $|z| = 2.2\,\mathrm{m}$ and $r = 6.4 - 41\,\mathrm{cm}$. It measured the energy deposited in the 320 towers of scintillator tiles that were alternated with metal plates of 3 mm thickness, corresponding in total to a radiation length of ~ 27. A silicon detector, composed of 3840 silicon strips, provided additional information on the shower direction. The spatial resolution in $R\phi$ was $\sim 0.4\,\mathrm{mm}$. The energy resolution was given as $\sigma(E)/E = 0.015 \oplus 0.135/\sqrt{E}$. The VSAT, situated at $|z| = 7.7\,\mathrm{mm}$, consisted of four identical calorimeter modules located symmetrically around the beam pipe, each composed of 11 silicon diodes separated by tungsten absorbers. Three silicon strip planes measured the shower position. The geometrical acceptance was 4.1-6.4 mrad in θ and 45-135 degrees in ϕ. The VSAT provided a useful monitoring of beam parameters and luminosity.

3.2.5 The Trigger and Data Acquisition System

In order to manage high luminosities and large background rates at LEP II, the DELPHI trigger was composed of four successive levels (T1,T2,T3,T4) of increasing selectivity. The first two trigger levels (T1,T2) were synchronous with respect to the Beam Cross Over signal (BCO). The trigger conditions included the fast tracking detectors (ID, OD, TPC, FCA and FCB), the calorimeters (HPC, FEMC and HCAL), the muon chambers (MUB) and the scintillators (TOF, HOF)[2]. In principle, the overlapping geometrical acceptance of the different subdetectors provided substantial redundancy between different trigger conditions.

The T1 and T2 trigger decisions were taken within 5 μs and 39 μs after the BCO, respectively. In case of a positive decision of the T2 trigger, the readout procedure of the Data Acquisition System (DAS) started with an average readout time of $\sim$ 2.5 ms per event. The fraction of dead time introduced by the trigger was dependent on the LEP crossing rate and the T1,T2 trigger rates which in turn depended on the backgrounds ($\sim$ total beam current). For the standard running at LEP II of $\approx$ 45 kHz BCO rate and trigger rates of T1 $\approx$ 300 Hz and T2 $\approx$ 3 Hz the introduced dead time was small ($\approx$ 2%). The last two trigger levels (T3,T4) were software filters performed asynchronously with respect to the BCO. T3 had the same logic as T2, but used more detailed information and halved the background passing T2. This maintained the data logging rate below 2 Hz. Finally, T4 rejected about half of the background events remaining after T3. The data of these two software triggers were also used to monitor the detector performance online. A detailed description of the trigger conditions and performance at LEP II can be found in [25].

The DAS system, based on the Fastbus standard, controlled the entire data transfer from the different subdetectors. During the readout, the detector operation was monitored and controlled by the Slow Control system. During the event reconstruction, the information on the status of each subdetector provided by the Slow Control System and the Data Quality Checking was combined to identify each module with a status flag. These flags were used for the run selection in the physics analysis.

[2] Time Of Flight, Forward Hodoskop

3.2.6 The Analysis Chain

In order to reduce the amount of information, the raw data taken with the DELPHI detector had to undergo certain processing before using them in the physics analyses in a suitable format. An outline of the production stream within the offline system is shown in Figure 3.7. The DELPHI reconstruction program (DELANA) was based on a modular structure that allowed the independent development of reconstruction code for the individual subdetectors. The backbone of the program was the Track ANAlysis and GRAphics package TANAGRA which provided a well defined data structure for storing track and vertex information in an independent format. All necessary constants needed for the reconstruction, e.g. pedestals, distortion corrections, machine running conditions, were taken from the DELPHI detector data base CARGO. In a first step, each subdetector decoded the raw data independently. This yielded to a set of "track elements" which, for example, consisted of a single point in $R\phi$, a full track segment from the TPC or an energy cluster from the calorimeters. These track elements provided the input to the global track search and fit processors. The track fit processor accounted for multiple scattering and energy loss in the material between the track elements. The fitted tracks were then extrapolated to the vertex detector and re-fitted using the vertex information. In a second step, clusters of energy were associated to the charged particles tracks, if possible, otherwise neutral tracks were created. Hits in the Muon Chambers were used for the muon identification.

The Data Summary Tapes (DST) contained very detailed information on events, called "full" DST. A further processing with the DSTANA package, the DST ANAlysis and fixing package, produced more data sets dedicated to the different physics teams, which were mainly the Short DST and extended Short DST (XSDST) allowing a faster analysis of the physics data. All data sets, from raw data to XSDST used the common data structure ZEBRA that made the transportation of data from one machine to another easily possible without converting the format. More details on the online and offline processing can be found in [24] and references therein.

In order to store the mostly used data sets on local machines at the university, the Wuppertal group developed a special format that achieved a further reduction of data (down to $\sim 10\%$) without loosing important information, called "Mini-DST". These could be derived from the DST and XSDST format.

An important tool in the analysis chain of data was DELGRA [26], the DELphi GRAphic package for interactive event viewing and analysis. It allowed a 3-dimensional view of an event with all tracks, hits and electromagnetic showers at different levels of data (raw, DST). Furthermore, analysis tools such as reconstructing jets, re-fitting tracks or parts of it, computing event variables, etc., were included. Two examples of a reconstructed muon pair event are shown in Figure 3.8. In the first picture a high energy event with two back-to-back tracks and hits in the surround muon chambers is illustrated. The second picture shows a radiative event with a photon having its energy deposited in the calorimeter.

3.2.7 The Simulation

An important role in the physics analysis plays the simulation of physics processes. The aim of a simulation program is to produce data which are as close as possible to the real data, including the knowledge of theory. These data are then treated in the same way as the real data using the reconstruction and analysis programs to make them comparable to physics results achieved by the real data.

The DELPHI Simulation (DELSIM) [27] is based mainly on two components. At first, the particles are produced in primary physics processes of e^+e^- interactions by generators using Monte Carlo methods. Different generators are used for different processes, for example, the KKMC event generator which provides events for fermion-pair production as described in the following sections. The output of the generators are the four-vectors of particles together with their possible decay products. In the next step, the particles are followed through the detector, stepping through the magnetic field until they hit an active detector component. Secondary interactions like pair production, multiple scattering, bremsstrahlung, etc., are taken into account. The realistic simulation of the detector response is provided by the different components using their specific simulation code including information from the data base CARGO. Finally, the output of DELSIM corresponds to the format of raw data after readout of the detector, which can be passed trough the analysis chain. In addition, the information of the generated particles is kept in order to allow the comparison of a "true" process with its measurement.

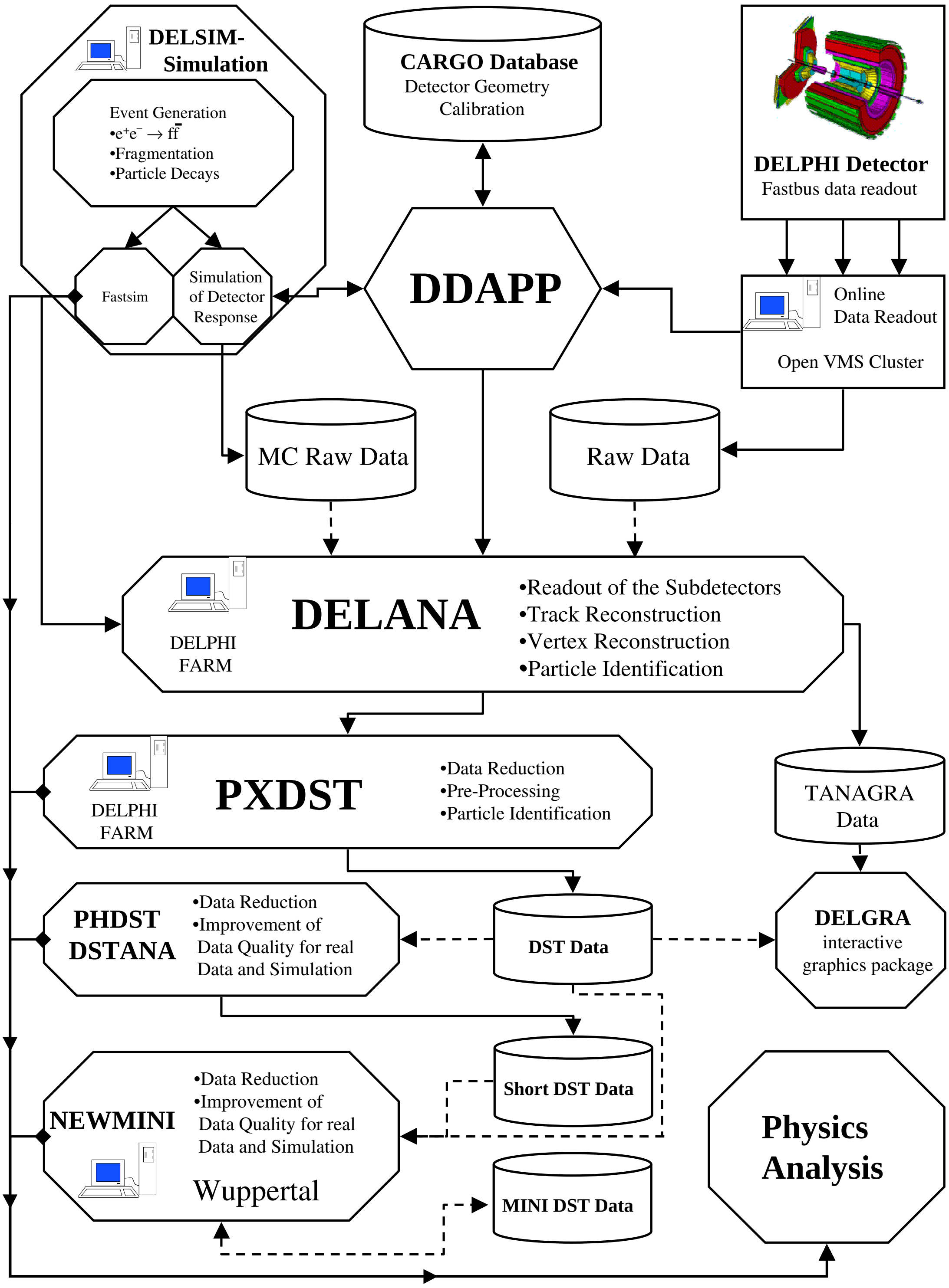

Figure 3.7: Analysis chain of data in the DELPHI experiment

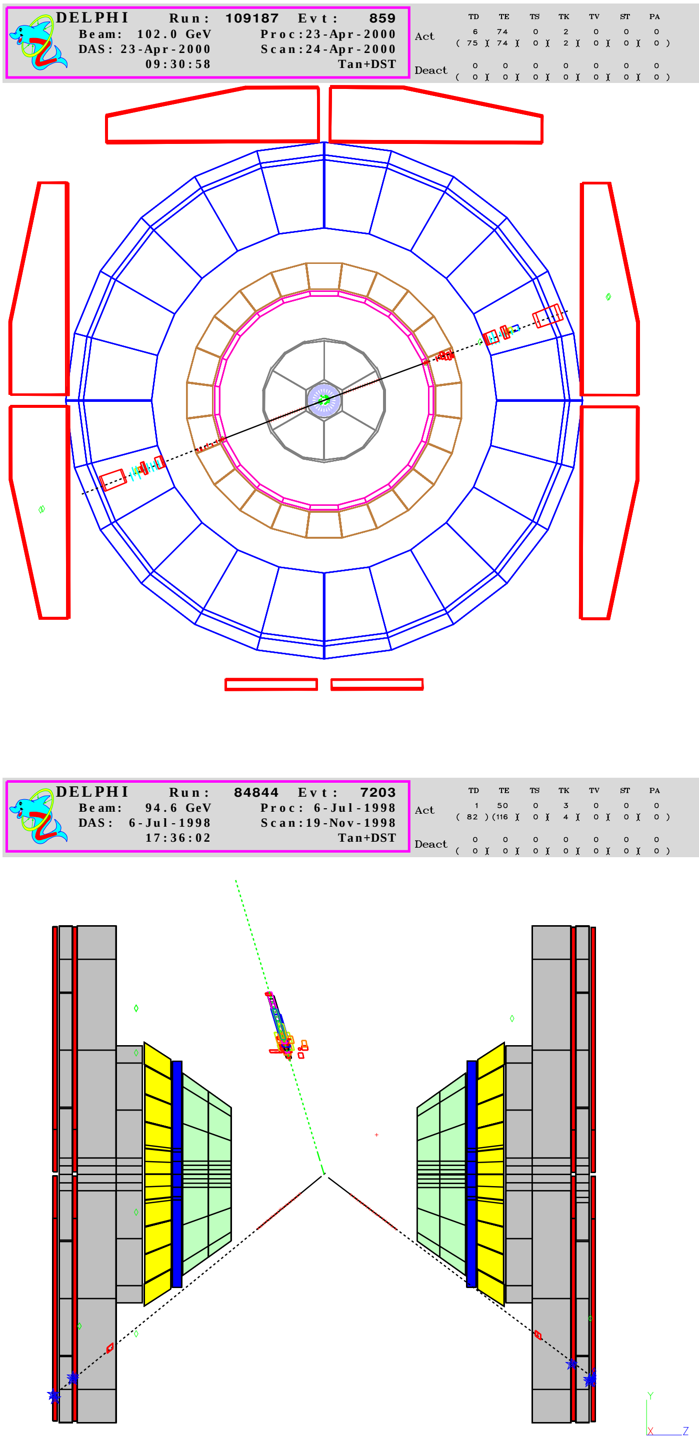

Figure 3.8: A graphical illustration of muon pair events produced in the e^+e^- annihilation: (top) a well measured high energy event at 205 GeV without photon radiation, (bottom) a radiative event at 189 GeV. The photon was reconstructed due to its shower in the electromagnetic calorimeter in the barrel. The outmost subdetectors seen are the muon chambers.

Chapter 4

Selection of Muon Pairs

4.1 Data Selection

4.1.1 Run Selection

Over the running period of the LEP accelerator the status of several DELPHI subdetectors may have changed due to temporary problems caused by various features. One common cause is machine background spikes that may have led to high voltage trips in some of the subdetectors while other components remained fully operational. To take this into account, data taking was divided into *runs* in which the status of all the subdetectors remained unchanged. This information was stored in a *run quality* file where each component in each *run* has a *status flag* reflecting the operational status.

In order to achieve a high data quality the following constraints were placed upon detectors most relevant for the tracking and identification of muons:

- The main tracking detector, the TPC, was required to be $\geq 90\%$ operational of its nominal efficiency[1]
- Either the muon chambers and/or the hadron calorimeter in the barrel and end-cap region were required to be $\geq 90\%$ operational of its nominal efficiency

These constraints avoid additional corrections arising from the detector performance.

In addition to the requirements on the subdetectors used for this analysis, *runs* were rejected for the cross-section measurements where the determination of luminosity failed due to occurring problems in the STIC subdetector during the running period.

4.1.2 Selection Criteria

The selection of muon events was done in two steps. First, muon candidates were selected by topological and kinematical cuts. The two tracks with highest momenta in an event were assumed to be muon candidates. Secondly, those were probed for muon identification criteria. A summary containing all cuts is given in Table 4.1.

[1]The value was lowered to 80% for the period after first of September 2000 where one sector of the TPC failed

Basic Cuts

Charged Multiplicity N_{ch} The following cut on the number of charged tracks was used:

$$2 \leq N_{ch} \leq 7.$$

As a clear topology with two tracks is always expected for a dimuon event a preselection was done by rejecting events with more than seven charged tracks. This minimised the data set to be analysed significantly by mainly reducing the hadronic background. The reason for allowing more than 2 tracks is the possibility of photon conversion in case of photon radiation.

Momentum Cuts Cuts were made on the momenta of the first and second fastest track separately. These were

$$|p_1| > 15 \text{ GeV/c} \qquad \text{and} \qquad |p_2| > 15 \text{ GeV/c}.$$

These cuts reduced the background contamination of $\tau^+\tau^-$, fully leptonic W^+W^-, ZZ, Zee, and two-photon events, see Figure 4.1 (top left).

In addition a cut on a third charged track with momentum greater than 5 GeV/c was made in order to reduce τ pairs. If the fastest charged track had a momentum above 90 GeV/c the event was accepted since this was most likely to be a muon pair, as can be seen in Figure 4.1

A further reduction of background was done by a cut on the invariant mass on the muon pair which is described later.

Impact Cuts In order to reduce cosmic background (these are muons coming from cosmic rays that pass the detector in coincidence with the BCO signal) cuts on the impact parameters were made. These are the closest approximations of the track to the interaction point in z-direction, IP_z, and in the $r\phi$-plane, $IP_{r\phi}$. As the topology of cosmic muons can be exactly the same to that of a dimuon production the distance to the interaction point is the best criterion to reduce the contamination. The following cuts were used:

$$IP_z < 2 \text{ cm},$$

$$IP_{r\phi} < 3 \text{ cm (no VD)} \qquad \text{or} \qquad IP_{r\phi} < 0.3 \text{ cm (VD)}.$$

The cut in the r - ϕ plane was dependent on whether there was information of the vertex detector (VD) or not. Further reduction of cosmic muons were made by accomplishing these loose cuts with a combined cut of $IP_{r\phi 1}$ and $IP_{r\phi 2}$, where one can profit from the fact that for cosmic muons these parameters are anti-correlated, whereas this is not the case for dimuons. Figure 4.2 (left) shows a distribution of the $IP_{r\phi}$ values - with respect to the beam spot - for events that passed the basic selection criteria and the muon identification. Data points in the central region origin from e^+e^- collisions, on the diagonal, far away from the interaction point, are the cosmic muons.

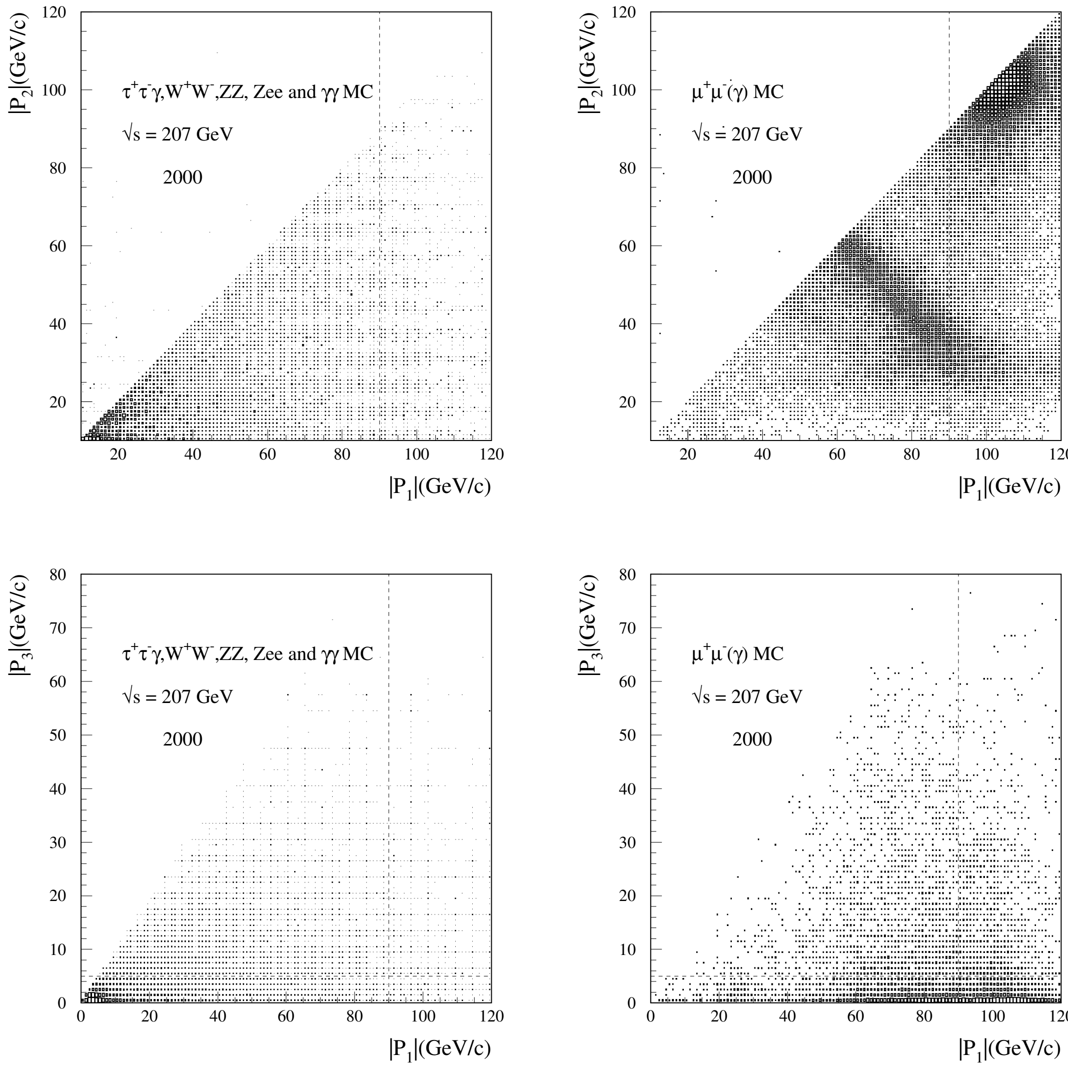

Figure 4.1: The momentum distribution of the two fastest tracks (top) and the momentum distribution of a third charged track as a function of the fastest track (bottom), for simulation of background processes (left) and simulation of signal (right), at 207 GeV.

A combined cut was done as follows:

$$(IP_{r\phi 1} < -1 \text{ cm} \ \text{ and } \ IP_{r\phi 2} > 1 \text{ cm}) \ \text{ or } \ (IP_{r\phi 2} < -1 \text{ cm} \ \text{ and } \ IP_{r\phi 1} > 1 \text{ cm}) \qquad (4.1)$$

without VD information. The cut value was decreased to 0.1 cm for tracks with VD information, see Figure 4.2 (right). The events along the diagonal inside the dashed boxes are used to estimate the contamination of cosmic muons by extrapolating them into the central region, this will be described later.

Angular Acceptance Only tracks within a polar angle of $14^\circ \leq \theta_{\mu^\pm} \leq 166^\circ$ were selected. This cut was placed on both tracks. Below (above) this value efficiency drops significantly

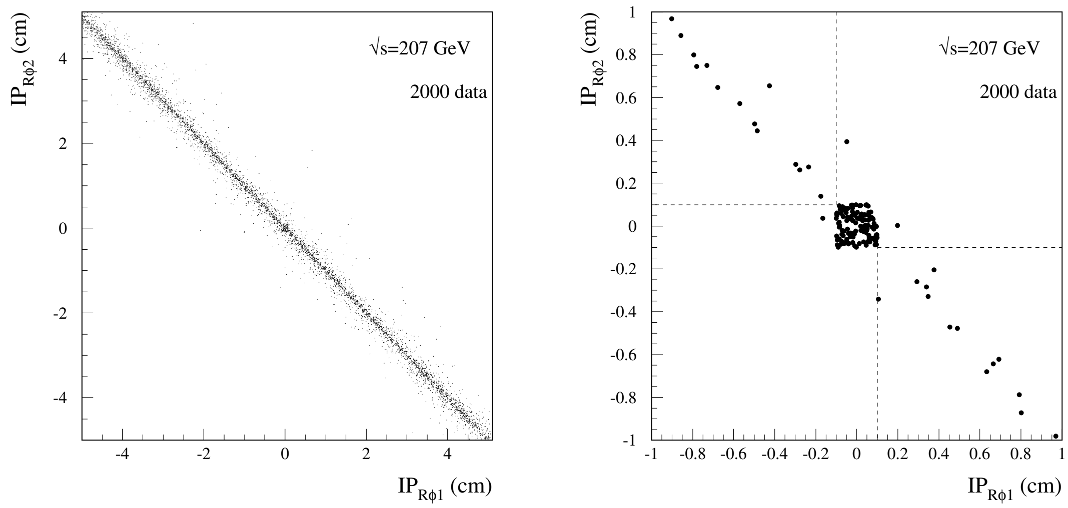

Figure 4.2: The impact parameter $IP_{r\phi}$ of the two fastest tracks after basic cuts and muon identification, (left) no IP_z cut, (right) with IP_z cut.

due to missing subdetectors in this region.

Muon Identification

The muon identification is done with information from muon chambers and calorimeters. The muon as a *minimal ionising particle* (MIP) deposits only a small amount of energy in the electromagnetic calorimeters (ECAL) and hadron calorimeters (HCAL) and penetrates the whole detector until its detection by the outmost muon chambers. Each of the two fastest tracks was probed for being a single muon with the following criteria.

Single Muon Criteria At least one of the following criteria was required to identify a charged track as single muon candidate:

- ECAL: the energy associated to the track was $E_{ECAL} < 1.5$ GeV, see Figure 4.3 (top left)
- HCAL: an associated shower energy per layer, corrected for the polar angle dependence was $E_{HCAL}/(N_{layer} \cdot C(\theta)) < 5$ GeV. N_{layer} had to be ≥ 2, at least one of them in the most outer region. Figure 4.3 (top right) shows the distribution of energy per layer of the HCAL as a function of θ.
- MUCH: there was at least one associated hit in the muon chambers.
  In addition, those tracks were accepted that were only seen by VD and/or ID (VD/ID only tracks) and had an un-associated hit in the muon chamber within a cone of 2° (only one of such tracks in an event was allowed). The distribution of muon chamber hits can be seen in Figure 4.3 (bottom left).

Vetoes A veto for muon identification was set on a track for the following criteria:

- ECAL: the energy associated to the track was $E_{ECAL} > 10$ GeV.
- HCAL: the corrected energy per layer was $E_{HCAL}/(N_{layer} \cdot C(\theta)) > 5$ GeV.

Muon Pair Identification An event was identified as a muon pair if each of the two fastest tracks fulfilled the muon identification criteria. A veto from ECAL for one track could be overruled by a muon chamber hit. A veto from HCAL for both tracks was allowed be overruled by muon chamber hits.

Figure 4.3 (bottom right) shows the distribution of detectors taking part in the muon identification. There is a good agreement in the total number of identified tracks between data and simulation, whereas the efficiency in the ECAL seems to be underestimated in simulation.

Run selection	TPC $\wedge$ (MUB $\vee$ HAB) $\wedge$ (MUF $\vee$ HAF) 90% operational of its nominal efficiency
Preselection	$2 \leq N_{ch} \leq 7$
Momentum	$p_{1/2} > 15$ GeV/c, $p_3 < 5$ GeV/c if $\max(p_1, p_2) < 90$ GeV/c
Impact	$IP_{z1}, IP_{z2} < 2$ cm, $IP_{r\phi1}, IP_{r\phi2} < 3/0.3$ cm (no VD/VD), combined $IP_{r\phi1}, IP_{r\phi2}$ cut, see Equation (4.1)
Angular Acceptance	$14° \leq \theta_{\mu^\pm} \leq 166°$
Muon Identification	$N_{MUCH} \geq 1$ or $E_{ECAL} < 1.5$ GeV or $E_{HCAL}/(N_{layer} \cdot C(\theta)) < 5$ GeV
Veto	$E_{ECAL} > 10$ GeV and $N_{MUCH} = 0$, $E_{HCAL}/(N_{layer} \cdot C(\theta)) > 5$ GeV and $N_{MUCH} = 0$

Table 4.1: Summary of all cuts (runs, kinematic, topologic and muon identification) for selecting muon pairs.

4.1.3 Corrections to Data and Simulation

In order to improve the agreement between the real data and the simulation, a number of corrections were applied before selecting events. These were corrections on the momenta and corrections on the muon chamber efficiency. They are also useful for other analyses, e.g. leptonic W decays into muons. The KK2F generator [28] was used for the simulation of $e^+e^- \to \mu^+\mu^-(\gamma)$ events. More details, not described here, can be found in [29].

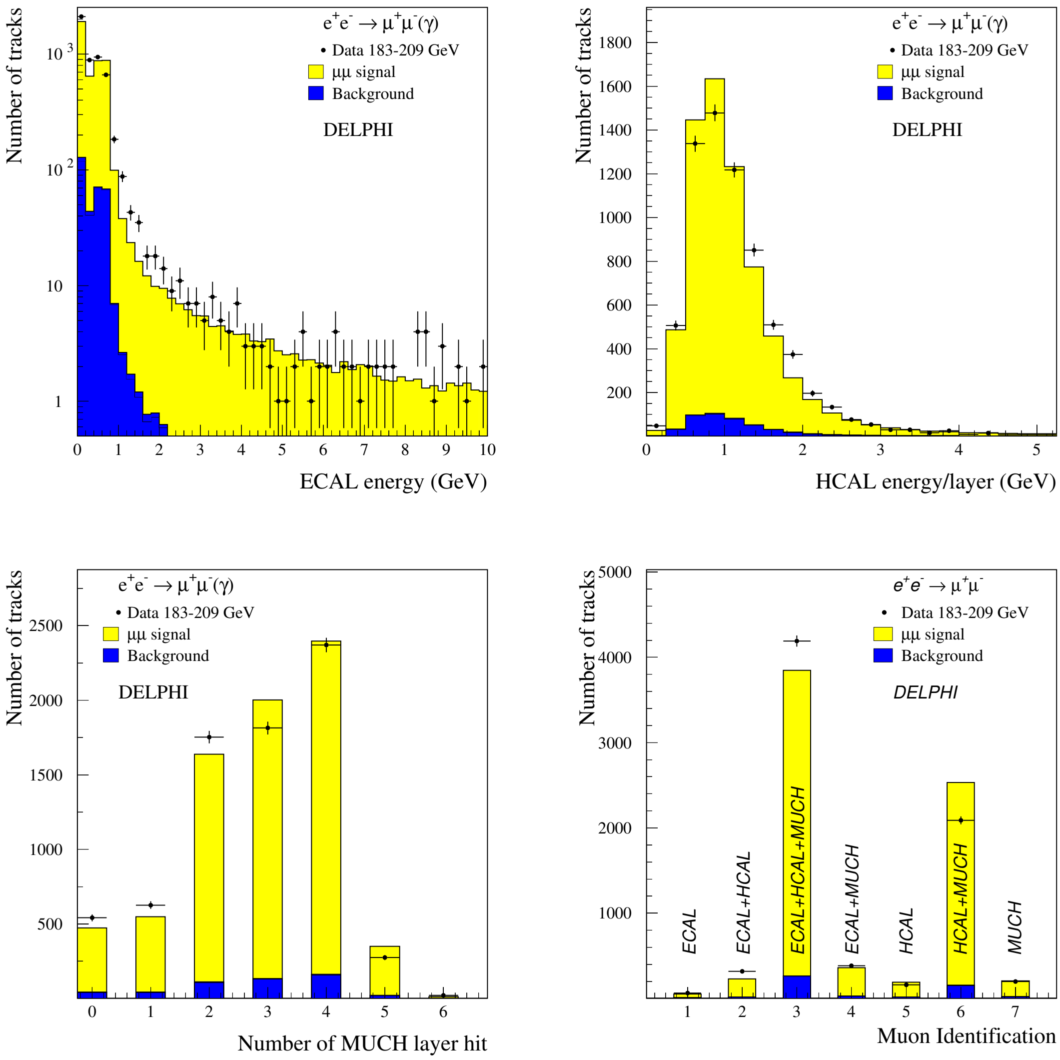

Figure 4.3: Muon identification quantities in comparison to simulation: (top) Distribution of associated energy in ECAL (left) and energy per layer in HCAL (right), (bottom) number of muon chamber hits associated to a track (left), detectors taking part in the muon identification (right).

Smear and Shift of the Momentum

The Time Projection Chamber (TPC) has always been affected by distortions of the drift path of the electrons that are produced by ionization along the particle trajectories. Those distortions are caused by defects of the electrical and magnetical fields and have been taken into account in the TPC calibration procedure [30]. A special method has been developed for the correction of LEP II data [31]. Residual shifts in the $1/p$ distribution between negatively and positively charged muons, caused by those effects, still existed in the data and were not seen in simulation. The most significant difference was found in the angular region between $138°$ and $144°$ which corresponds to the gap between the Outer Detector (OD) and the

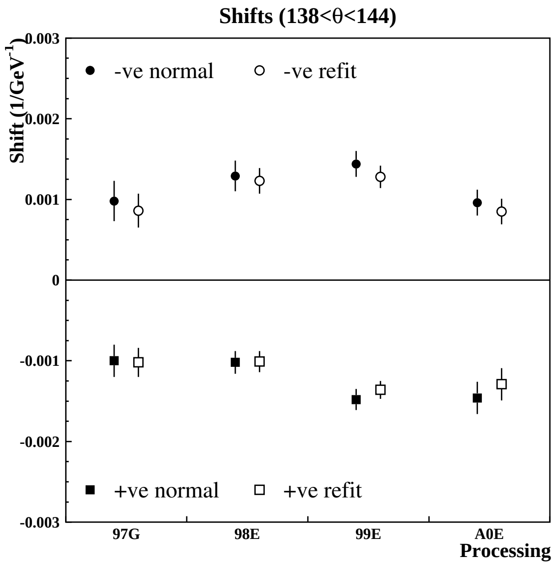

Figure 4.4: The size of the shifts to $1/p$ for positive and negative muons (*normal* and *beam spot re-fitted* tracks) in the angular region of $138^\circ < \theta < 144^\circ$ from 1997-2000 for different processings.

Forward Chambers and where the TPC is the outermost tracking device. As the momentum is one of the selection criteria and is later used to evaluate the effective center-of-mass energy, corrections on that effect were necessary.

The determination of corrections to the momenta in data and simulation is based on data taken at the Z^0 runs ($\sqrt{s} \approx M_Z$) during the years from 1997 to 2000 as those tracks have a definite momentum of $M_Z/2 \simeq 45$ GeV. The corrections on the muon momenta were done in two steps.

- A charge dependent shift was computed for the real data
- After applying the shifts, smearings were computed for $1/p$ in simulation

Shifts were computed, according to

$$\Delta(1/p_\pm) = (1/p_\pm)_{sim} - (1/p_\pm)_{data} \,. \tag{4.2}$$

This was done in bins of θ, for both charges separately, for each year from 1997 to 2000 taking into account that some tracks had to be re-fitted using the beam spot information if the track was not detected by the VD. The largest correction was found to be $|\Delta(1/p)| = 1.5 \cdot 10^{-3}(\mathrm{GeV/c})^{-1}$ in the $138^\circ < \theta < 144^\circ$ region. The shifts for this region for each processing is shown in Figure 4.4. The corrections for other regions of θ amount between 10^{-4} and 10^{-5}.

After applying the shifts to the data, a comparison of the *rms* spread in $1/p$ was made. As expected, the *rms* was wider in data than in simulation as this was an known effect seen in LEP I. Possible misalignments in the real DELPHI detector that are not simulated led to an

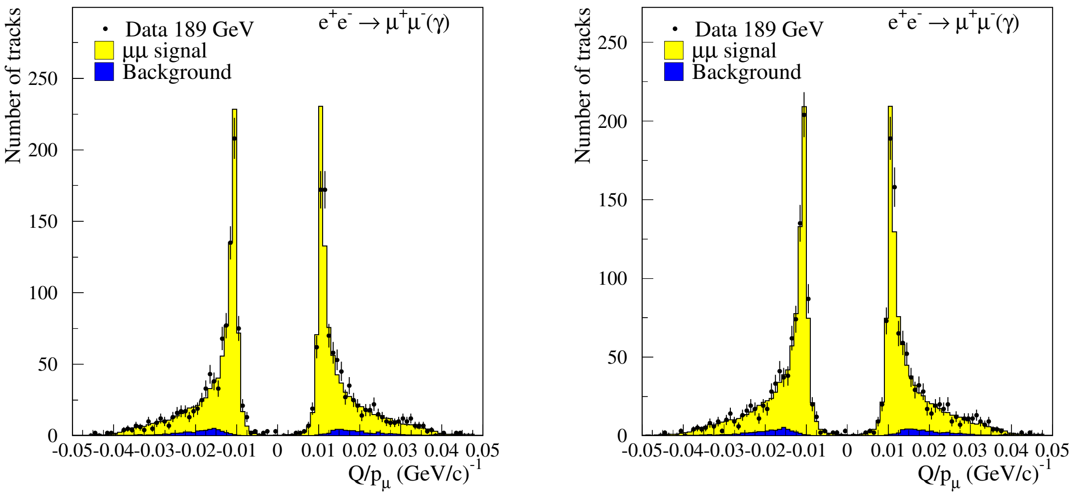

Figure 4.5: The Q/p distributions for high energy dimuons at 189 GeV before the momentum corrections (left) and after application of the shifts and the smearings to the momentum in data and simulation, respectively (right).

overestimation of the momentum resolution in simulation. Smearings were computed using a double Gaussian function to convolute with the $1/p$ distribution in simulation and fitting its parameters to the data. This was done in different bins of θ and whether there were OD hits for a track or not. The complete set of numbers used for the corrections can be found in [29].

Figure 4.5 shows the distributions for Q/p from the high energy data at 189 GeV before and after the corrections in comparison to the simulation. The agreement after the corrections is sufficiently good and indicates that the corrections applied on the high energy muons are momentum independent. This statement obviously can not be substantiated due to the lack of statistics in high energy data. However, the application of both, the shifts and the smearings, significantly improves the agreement between data and simulation.

Muon Chamber Hits

A comparison of the numbers of muon chamber hits associated to a muon track between data and simulation showed discrepancies. In simulation the efficiency of the muon chambers seemed to be higher than in data. This is caused by different reasons. In the barrel, the loss of efficiency is due to a high rate of trips in particular sectors of the muon chambers that led to the fact that a muon passing this sector at that time had no hits recorded. In the forward, due to electrical problems in the chambers, some particular layers were known to be inefficient. These effects were not simulated and had to be corrected for in simulation.

As the problems varied throughout data taking, it was necessary to use high energy data itself, rather than the Z^0 data. A sample of non-radiative events with high momentum tracks was used to calculate a correction for the distribution of the number of muon chamber hits in simulation. The extra inefficiencies in the muon chambers were parameterised as a function of global and layer inefficiencies and then fitted to data from 1997 to 2000. The obtained corrections, which can be found in [29], were applied on an event-by-event basis when analysing the data.

The effect of this correction does not have a significant impact on the number of dimuon events selected in this analysis as the selection criteria are very loose ($N_{MUCH} \geq 1$) and are not only based on the muon chambers, but on a combination between them and the calorimetry. The corrections, nevertheless, should be taken into account as they improve the agreement between data and simulation for the number of muons without associated muon chamber hits.

4.2 Data Sets and Luminosity

The data sets used for this analysis and the corresponding luminosity collected at the different nominal center-of-mass energies in the years from 1997 to 2000 are shown in Table 4.2. The errors given for the luminosity are the statistical ones coming from the measurement of the Bhabha process ($e^+e^- \rightarrow e^+e^-$ in the t-channel) at very low angles in the STIC.

The measured center-of-mass energies given here are obtained from a luminosity averaged mean after the run selection described in section 4.1.1. The LEP accelerator delivered, more or less, a constant energy in the years 1997 to 1999, whereas in 2000 the energy was spread in a wider range by increasing it continously in the so-called *mini-ramps*, in order to achieve the highest energy ever reached. Two samples in 2000 were chosen:

$$202.5 \text{ GeV} \leq \sqrt{s} < 205.5 \text{ GeV} \quad \text{and} \quad \sqrt{s} \geq 205.5 \text{ GeV},$$

resulting to a nominal center-of-mass energy of 205 and 207 GeV, respectively.

The processing in 2000 had been divided into two parts, one for the data taken before the 1^{st} of September, and one for events that were selected after that date, because since that day the TPC suffered a loss of an irreparable broken sector (1/12 of the acceptance). The tracking code had to be modified accordingly for that period in order to recover the tracking efficiency by using remaining detector information [32]. The same code was implemented in the DELSIM code for the corresponding simulation samples. Studies have been made to ensure the usability of this data set for the analysis presented here. No significant losses compared to the other data sets have been found and there was no obvious reason not to use it. To take into account for the differences between them, this data set was analysed separately, henceforth called 207U, in comparison to the "normal" sample 207E (according to the processings). The small sample at 205 GeV ($\approx$ 6 pb^{-1}) in this period was not considered.

4.3 Reconstruction of $\sqrt{s'}$

As described in chapter 2.1.3 many events undergo initial state radiation (ISR) and in a smaller amount final state radiation (FSR). This leads to the fact that the effective center-of-mass energy, $\sqrt{s'}$, in most cases is smaller than the nominal center-of-mass energy, $\sqrt{s}$. Very often $\sqrt{s'}$ is reduced down to the Z-Peak, so-called *radiative Z returns*. Two event samples

Year	Energy (GeV)		Processing	integrated Luminosity
	nominal	measured		$\int \mathcal{L}dt\ (pb)^{-1}$
1997	183	182.651	97G	52.544 ± 0.088 (stat)
1998	189	188.625	98E	156.384 ± 0.165 (stat)
1999	192	191.595	99E	25.788 ± 0.078 (stat)
	196	195.530	99E	73.982 ± 0.141 (stat)
	200	199.528	99E	83.140 ± 0.152 (stat)
	202	201.646	99E	40.510 ± 0.107 (stat)
2000	205	204.848	A0E	75.554 ± 0.149 (stat)
(< 1.Sept)	207E	206.613	A0E	85.098 ± 0.159 (stat)
($\geq$ 1.Sept.)	207U	206.452	A0U	51.969 ± 0.124 (stat)
total	197	197.061	-	644.969 ± 0.398 (stat)

Table 4.2: The data sets at different nominal energies used for the analysis with the corresponding luminosity weighted mean energy and the luminosity collected at each energy.

with different cuts on $\sqrt{s'}$ will be considered, thus, it is important to know $\sqrt{s'}$ very well. The non-radiative sample is of special interest as it is most sensitive to new physics phenomena. So first of all, one has to define $\sqrt{s'}$. This can be done in different ways, e.g. it can be taken as the invariant mass of the s-channel propagator.

4.3.1 Definition of $\sqrt{s'}$

In this analysis $\sqrt{s'}$ is chosen to be defined as the invariant mass of the selected muon pair:

$$\sqrt{s'} = M_{inv} = \sqrt{(E_{\mu^-} + E_{\mu^+})^2 - (\vec{p}_{\mu^-} + \vec{p}_{\mu^+})^2}, \tag{4.3}$$

with $E_{\mu^\pm}$ the energy and $\vec{p}_{\mu^\pm}$ the 3-momenta of the measured muons.

This has several advantages. Experimentally one can neglect final state photons and calculate $\sqrt{s'}$ simply from the measured 4-momentum of the muon pair. No ISR/FSR interference effects have to be subtracted. The 'true' value of $\sqrt{s'}$ can be easily calculated from the generated momenta in simulation. Finally, the definition of $\sqrt{s'}$ is implemented in the ZFITTER package [33] which calculates the predictions for $\sigma_{\mu\mu}$ and $\mathrm{A}_{\mathrm{FB}}^{\mu\mu}$.

The accuracy of $\sqrt{s'}$ is limited experimentally by the resolution of the measured momenta. One method to improve the resolution of $\sqrt{s'}$ is to use the Angular Method. A better method is the Constrained Fitting of the measured quantities. Both are described in the following.

4.3.2 The Angular Method

With the angular method one derives the energy of a radiated photon from the polar angles of the final muon pair only. For one photon emitted along the beam direction its energy is:

$$E_{\gamma\,(ISR)} = \frac{|\sin(\theta_{\mu-} + \theta_{\mu+})|\,\sqrt{s}}{\sin\theta_{\mu-} + \sin\theta_{\mu+} + |\sin(\theta_{\mu-} + \theta_{\mu+})|}, \tag{4.4}$$

where $\theta_{\mu-}$ and $\theta_{\mu+}$ are the polar angles of the negatively and positively charged muon, respectively, with $\theta_{acol} \neq 0$ and $\phi_{acop}{}^2 = 0$ (see Figure 4.6).

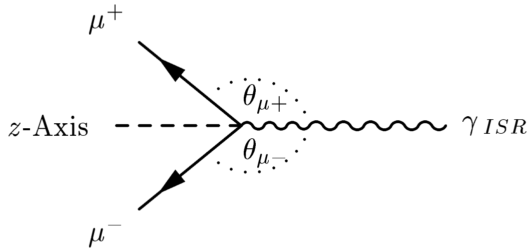

Figure 4.6: Angular method: polar angles of the muon pair

With the application of four momentum conservation to a radiative muon pair, the effective center-of-mass energy can be calculated in terms of $\sqrt{s}$ and E_γ alone:

$$s' = s - 2\,E_\gamma\,\sqrt{s}\;. \tag{4.5}$$

The substitution of E_γ, given in Equation (4.4), into Equation (4.5) gives a formula for $\sqrt{s'}$ in terms of the polar angles of the muons and $\sqrt{s}$:

$$\sqrt{s'} = \sqrt{\left(\frac{\sin\theta_{\mu-} + \sin\theta_{\mu+} - |\sin(\theta_{\mu-} + \theta_{\mu+})|}{\sin\theta_{\mu-} + \sin\theta_{\mu+} + |\sin(\theta_{\mu-} + \theta_{\mu+})|}\right) \cdot s}\;. \tag{4.6}$$

For back-to-back events where $\theta_{acol} \simeq 0$ (with $\theta_{\mu-} + \theta_{\mu+} = 180°$) this simply becomes $\sqrt{s'} = \sqrt{s}$.

As a matter of fact, the formula overestimates $\sqrt{s'}$ for radiative events with photons emitted in any direction. This is shown in Figure 4.10 where a comparison of the reconstructed $\sqrt{s'}$ to the 'true' $\sqrt{s'}$ from simulation is made.

4.3.3 Constraint Fitting

A more accurate method to reconstruct the invariant mass of the muon pair is the use of the *Constrained Fit.* In this method, kinematic constraints are applied on the measured muon track parameters, assuming different event topologies such as no photon was radiated or a photon was emitted in any direction. Seen photons that deposited energy in the calorimetry were taken into account. The constraints are those from 4-momentum conservation:

$$\sum_i^N p_i^k = 0 \;\text{ and }\; \sum_i^N E_i = \sqrt{s},$$

[2] The acoplanarity is defined as $\phi_{acop} = 180° - \alpha$, with α being the angle between the two muons in the projection to the $r - \phi$ plane

with k = 1,2,3 reflecting the component in x,y,z direction and N = number of particles (2 muons + photons)

Different topologies result in different number of constraints. The following event topologies were considered:

- No photon emitted $\Rightarrow$ 4 Constraints:

$$\begin{aligned} \vec{p}_{\mu^-} + \vec{p}_{\mu^+} &= 0 \\ E_{\mu^-} + E_{\mu^+} &= \sqrt{s} \end{aligned}$$

- 1 undetected ISR photon emitted in the beam direction $\Rightarrow$ 3 Constraints:

$$\begin{aligned} p^{x/y}_{\mu^-} + p^{x/y}_{\mu^+} &= 0 \\ E_{\mu^-} + E_{\mu^+} + |p^z_{\mu^-} + p^z_{\mu^+}| &= \sqrt{s} \end{aligned}$$

- n detected photons + 1 undetected photon emitted $\Rightarrow$ 1 Constraint:

$$E_{\mu^-} + E_{\mu^+} + \sum_i^n E_{\gamma_i} + |\vec{p}_{\mu^-} + \vec{p}_{\mu^+} + \sum_i^n \vec{p}_{\gamma_i}| = \sqrt{s},$$

For this analysis only $n = 1$ has been considered. The χ^2 evaluated from the track parameters, the covariance matrix and a matrix representing the constraints was minimised. As track parameters, the inverse momentum, $1/p$, the polar angle, θ, and the azimuth angle, ϕ of the muons were used. The algorithm of the constraint fit is described in Appendix A and more details to it can be found in a DELPHI note [34].

Boost Corrections

A natural energy spread of the nominal center-of-mass energy existed in data that had to be taken into account when applying the constraint fit. As the particles of the incoming bunches had a momentum dispersion of ≈ 0.2 GeV/c, the energy of the electron and positron at the collision was not exactly equal. Thus, the center-of-mass system was not at rest in the laboratory frame, but boosted in the direction of the incoming particles (z-direction), even in case no photon had been radiated. The boost resulted in a change of the polar angles of the two muons leading to a broadening of the peak at low acollinearities. This effect, in contrast to the small change in center-of-mass energy, was not negligible. The 4C fit requires $\theta_{acol} = 0°$ and therefore is very sensitive to deviations from a clear back-to-back topology. The change in angles due to the boost is ≈ 10 times larger than the estimated error on theta $\Delta\theta$ ($\approx 0.01°$) and can be derived from formula (4.4) assuming E_γ to be equal the resulting boost, Δp_z, the momentum imbalance in beam direction:

$$\sin \Delta\theta_{\mu\pm} = \frac{\Delta p_z}{\sqrt{s} - \Delta p_z} \cdot \sin \theta_{\mu\pm}. \tag{4.7}$$

In approximation, this gives typically an acollinearity of $\theta_{acol} = 2 \cdot \Delta\theta_{\mu\pm} \simeq 2 \cdot \Delta p_z/\sqrt{s}$, e.g. $\theta_{acol} = 2$ mrad ($0.11°$) at $\theta_{\mu\pm} \simeq 90°$ and $\Delta p_z = 0.2$ GeV.

The energy spread was taken into account in the fit procedure as an additional measurement of the boost. The constraints of the 4C fit were changed in the following way:

$$\begin{aligned} E_{\mu^-} + E_{\mu^+} &= \sqrt{s} \\ \vec{p}_{\mu^-} + \vec{p}_{\mu^+} &= \vec{p}_{boost}, \\ \text{where} \quad \vec{p}_{boost} &= \pm\Delta p_z. \end{aligned}$$

The Δp_z was computed for each event taking a random (Gaussian) boost from the known center-of-mass energy spread[3] which was of the order of $\approx$ 250 MeV. The exact values for each year were taken from [23]. The effect of the boost on the other fits was negligible, because the real back-to-back events that failed the 4C fit in data before in most cases were fitted by the 3C fit (photon in beam direction) that compensated the boost in z-direction. The boost affected mainly events with $\sqrt{s'}$ close to $\sqrt{s}$.

In simulation the incoming electron and positron beams were taken to be equal in the opposite momenta, thus, the beam energy had to be "smeared". The boost was computed for each generated event and applied on the 4-momentum of each particle in that event. After this, the distribution of the acollinearity showed good agreement to the data as shown in Figure 4.7. The width ($\approx 0.12°$) is broadened by the beam energy spread, radiation and resolution. The agreement of the residuals of the polar angles and, thus, the χ^2 distribution of the 4C fit improved significantly after the boost corrections.

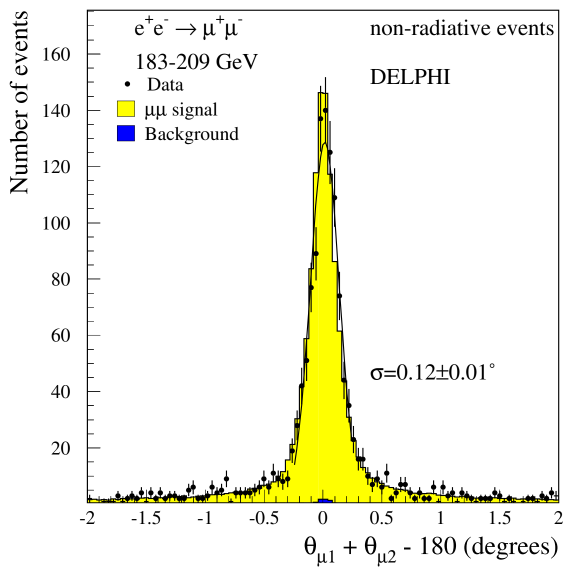

Figure 4.7: The distribution of the polar angles, $\theta_{\mu 1}+\theta_{\mu 2}-180°$, of the two highest momentum muons in data and simulation after applying the boost.

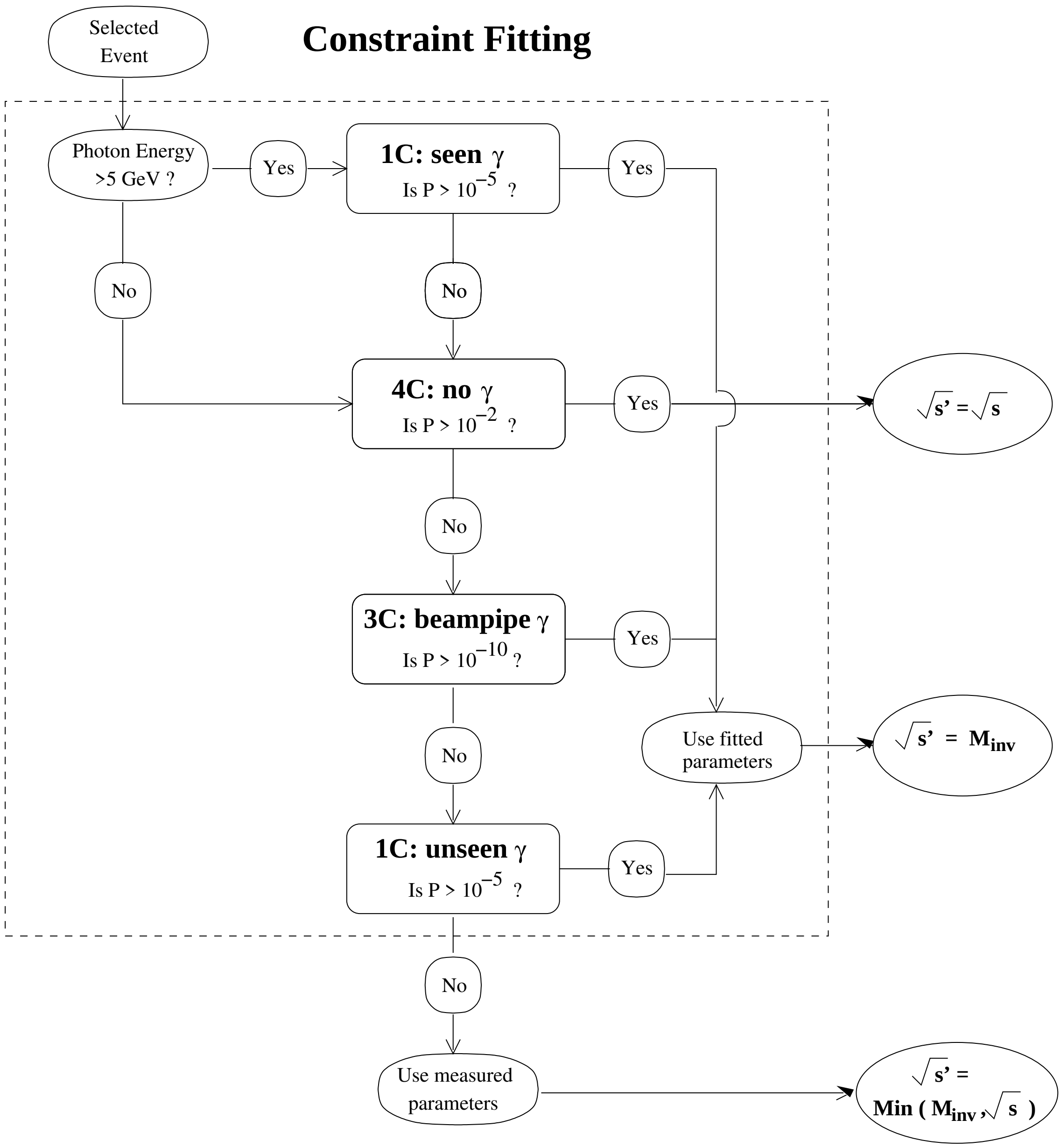

Figure 4.8: A flow diagram showing the application scheme of the constraint fitting procedure used on $e^+e^- \to \mu^+\mu^-(\gamma)$ events.

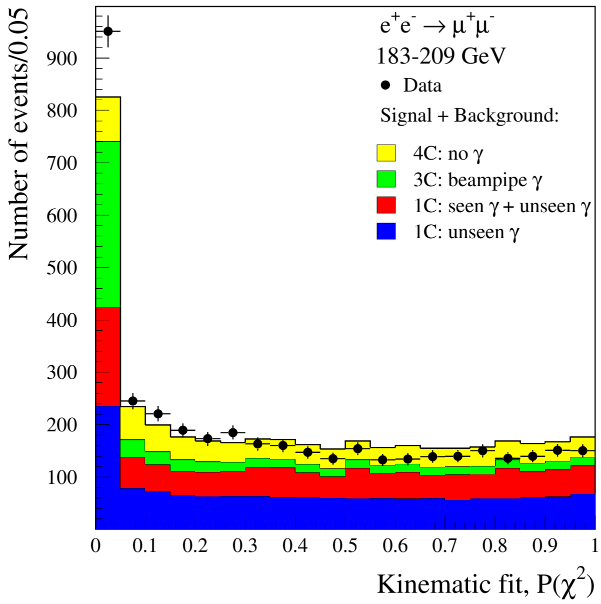

Figure 4.9: Distribution of probabilities obtained with the kinematic fit.

Application Scheme

The constraint fits with the four considered event topologies were applied successively in a scheme diagrammed in Figure 4.8. An event was successfully reconstructed if one of the fits had converged and the obtained χ^2 passed the probability cut. In this case, the fitted track parameters were used to calculate $\sqrt{s'}$. First, if a selected event had a detected photon in the calorimetry with an energy $E_\gamma > 5$ GeV, a 1C fit was applied assuming that a second photon had been emitted, because this was more likely the case. In case the fit failed, the 4C fit with no emitted photon was applied, assuming that the measured photon may have been noise in the detector. If this was successful $\sqrt{s'}$ was taken to be $\sqrt{s}$. In the next step the 3C fit with an unseen photon in the beam pipe was probed. Finally, a 1C fit with one photon in any direction was applied that, in most cases, was successful as this fit has the ability to compensate missing energy and momentum. In case none of the fits were successful the measured track parameters were used to calculate $\sqrt{s'}$, which is required to be $\leq \sqrt{s}$. Those events were assumed to be partly dimuon events with double radiative returns which were not implemented in the topologies, or background processes like leptonic W^+W^- events, whose kinematic does not match to any of the assumed topologies. About $\approx 7\%$ of the events remain unfitted, $\approx 85\%$ of those are expected to be background events with low invariant masses.

The probability cut values used for each fit were derived from previous tests [35] using generated event samples with a given topology that had to pass the different fits. Those were modified for the 3C and 4C fit since the boost of the events was implemented. The overall

[3]Note that beam energy spread is equal to center-of-mass energy spread divided by a factor of $\sqrt{2}$

distribution of probabilities[4] for events that passed the kinematic fit is illustrated in Figure 4.9 and shows an agreement between data and simulation. The excess in data seen at low probabilities is assumed to come from slightly underestimated errors in simulation and remaining differences after the boost corrections. However, the agreement of the number of events fitted with the 4C fit after the boost corrections between data and simulation was sufficient.

4.3.4 Results

Figure 4.10 shows the distributions of the 'true' $\sqrt{s'}$ in comparison to the reconstructed $\sqrt{s'}$ for the angular method and the constrained fit. As expected the angular method favours high values of $\sqrt{s'}$ as its assumption of one ISR photon radiated in the beam pipe is not always true, whilst the constrained fit allows the $\sqrt{s'}$ to be reconstructed over the whole range of effective mass. Figure 4.11 shows the residuals between the generated and reconstructed values of $\sqrt{s'}$ for the three different methods that were presented here: the use of measured track parameters (1), the angular method (2) and the constraint fit (3). It can clearly be seen that the constraint fitting reduces the *rms* of the distribution in comparison to (1), as well as the bias from the mean which is observed in method (2).

Figure 4.12 shows the distribution of the reconstructed $\sqrt{s'}$ for low invariant masses and $\sqrt{s'}/\sqrt{s}$ for high invariant masses for all data from 183-209 GeV after the constrained fitting in comparison to simulation. For very low invariant masses the background processes dominate over the signal. These are processes like fully leptonic W^+W^-, ZZ decays, *Zee*-like and two-photon events. A cut was applied defining an event sample, henceforth called the *inclusive sample*, which is:

$$\sqrt{s'} \; > \; 75 \text{ GeV}$$

Accordingly a *non-radiative sample* was defined, where only small photon radiation is allowed, requiring:

$$\sqrt{s'}/\sqrt{s} \; > \; 0.85$$

The cosmic background would have been increased by a factor of 2 in this sample if the angular method was used, as the cosmics have $\theta_{acol} \approx 0°$ and therefore, with formula (4.6), would have been reconstructed close to $\sqrt{s}$. The contamination of wrongly reconstructed events from below $\sqrt{s'}/\sqrt{s} = 0.85$ into the non-radiative sample has to be taken into account when calculating the cross sections in Section 5.1. The distribution of $\sqrt{s'}/\sqrt{s}$ for the different nominal center-of-mass energies from 183 GeV to 207 GeV are shown in Figure 4.13 and 4.14.

[4]The number of constraints is equal to the number of degrees of freedom used to evaluate $P(\chi^2)$

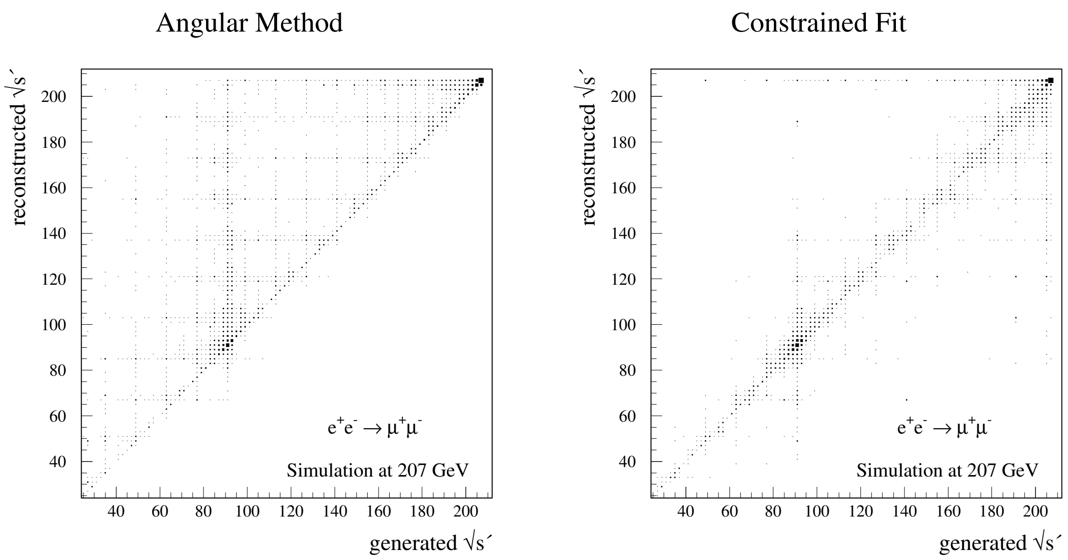

Figure 4.10: The distribution of reconstructed $\sqrt{s'}$ versus generated $\sqrt{s'}$ in simulation at 207 GeV: (left) angular method, (right) constrained fit.

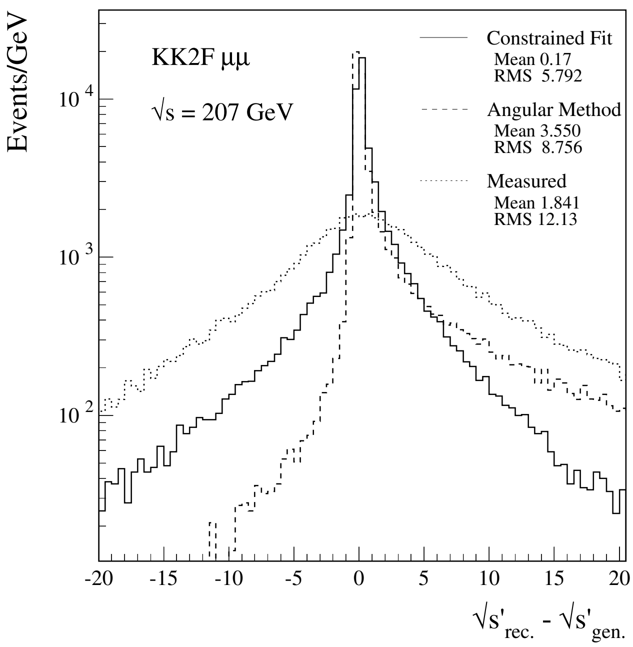

Figure 4.11: The residuals between the generated and reconstructed values of $\sqrt{s'}$ with the use of the measured track parameters, the *angular method* and the *constrained fit.*

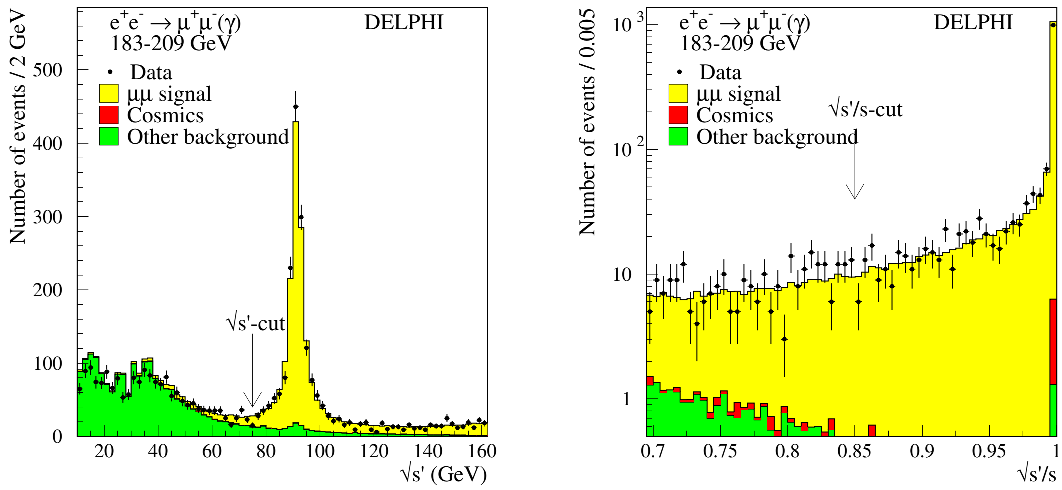

Figure 4.12: The distribution of the reconstructed invariant mass, as absolute values $\sqrt{s'}$ (left), and relative values to the beam energy $\sqrt{s'}/\sqrt{s}$ (right), for the constrained fit. The arrows mark the cut on $\sqrt{s'} > 75$ GeV and $\sqrt{s'}/\sqrt{s} > 0.85$, respectively.

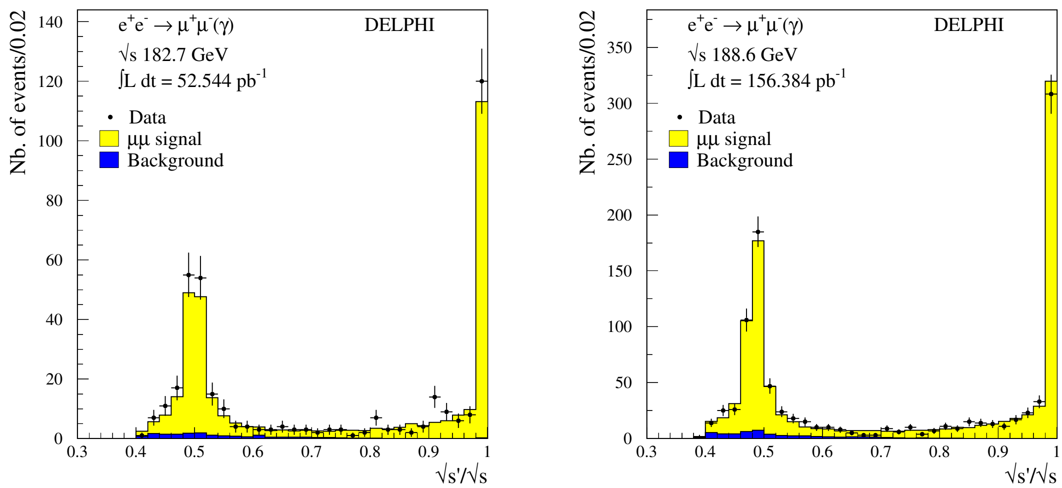

Figure 4.13: The distribution of the reconstructed $\sqrt{s'}/\sqrt{s}$ from the constraint fit for nominal energies at 183-189 GeV.

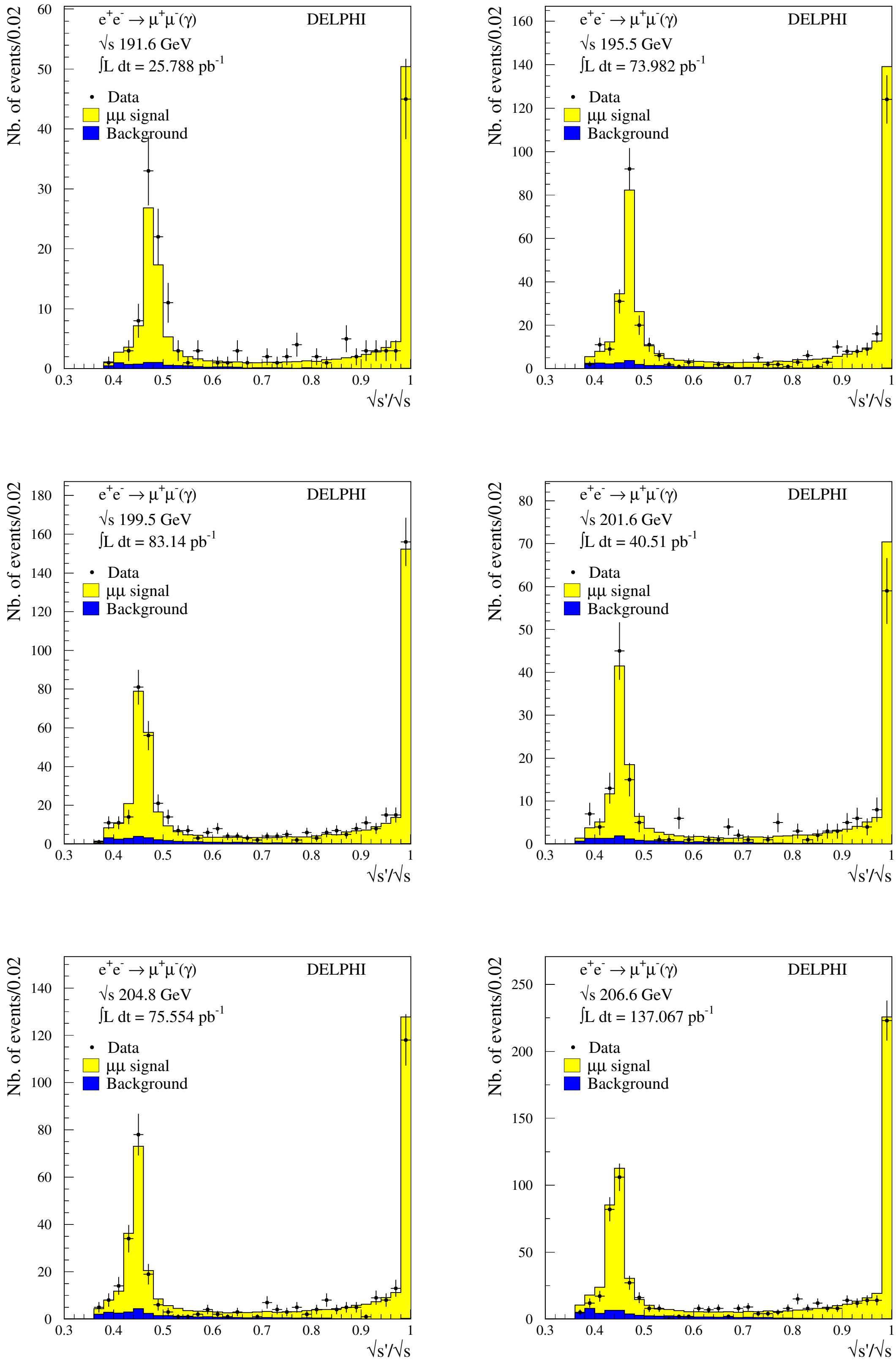

Figure 4.14: The distribution of the reconstructed $\sqrt{s'}/\sqrt{s}$ from the constraint fit for nominal energies at 192-207 GeV.

Chapter 5

Cross Sections and Asymmetries

5.1 The total Cross Section

The total cross section for a certain process, in this analysis the reaction $e^+e^- \to \mu^+\mu^-(\gamma)$, is simply defined as the number of produced events divided by the integrated luminosity of the beams:

$$\sigma = \frac{N}{\mathcal{L}}. \tag{5.1}$$

However, in the experimental determination of the cross section one has to expect that the observed number is not the 'true' number of events. Some corrections have to be considered, like efficiency losses or impurities due to background contaminations. So one has to take into account for several corrections that are reflected in the following formula:

$$\sigma_{\mu\mu} = \frac{N_{sel} - N_{bgd}}{\epsilon_{sel} \cdot \epsilon_{trig} \cdot \mathcal{L}} \cdot F_{mig} \cdot \eta_{4\pi}, \tag{5.2}$$

where

$$\begin{aligned}
N_{sel} &= \text{number of events selected} \\
N_{bgd} &= \text{number of background events expected} \\
\epsilon_{sel} &= \text{selection efficiency} \\
\epsilon_{trig} &= \text{trigger efficiency} \\
\mathcal{L} &= \text{integrated luminosity} \\
F_{mig} &= \text{migration factor} \\
\eta_{4\pi} &= \text{angular acceptance correction}
\end{aligned}$$

The integrated luminosities were taken from Table 4.2. The evaluation of the listed components are discussed in the next sections.

5.1.1 Selection Efficiency

The easiest way to calculate the selection efficiency is to use simulation and look for the ratio of numbers of accepted events, after generation and detector simulation, to the number of generated events, which should be the 'true' number of events.

$$\epsilon \ (Simulation) = \frac{N_{accepted}}{N_{generated}} \tag{5.3}$$

However, to do that, one has to be sure of a good agreement between real data and simulation. Previous studies (see [36]) have shown that the agreement is only valid on a 0.5% level for the *single arm efficiency.* An overestimation of the total efficiency in simulation by $\approx 1\%$ was observed.

A better method is to estimate the selection efficiency directly from the real data itself, as far as possible. Since 1997, at 183 GeV and higher energies, statistics was high enough to calculate the *single arm efficiency* from real data. The detailed procedure is described below.

Single Arm Efficiency

The *single arm efficiency* can be derived from data directly using events from a very clean subsample of muon pairs with a clear back-to-back topology. The evaluation was done by separating two parts:

$$\epsilon(\text{Single Arm}) \ = \ \epsilon(\text{Track Reconstruction}) \ \cdot \ \epsilon(\text{Muon Identification}). \tag{5.4}$$

Both, the *track reconstruction efficiency* and the *muon identification efficiency* were calculated separately as described in the following.

Track Reconstruction Efficiency The idea to determine the track reconstruction efficiency from data is motivated by the fact that a dimuon event can be identified with only a single muon track. A definitely reconstructed muon track and at least one associated or un-associated hit in the muon chambers in the opposite hemisphere is a good trigger for a dimuon event. As at LEP II one has to deal with topologies that are not always 'back-to-back' due to photon radiation, the procedure has to be modified to that used in LEP I. In order to minimize background contamination a sample with high momentum and reduced photon radiation was required.

The following cuts were used to select a trigger[1]:

- One or two tracks with $p_{1/2} \geq 15$ GeV/c
- The energy of a seen photon was $E_\gamma < 3$ GeV
- The momentum of the trigger track was $p_{trig} > 0.8 \cdot E_{Beam}$
- Tight impact cuts, $IP_z/2$ and $IP_{r\phi}/3$ of values in Table 4.1
- No Bhabha veto, $E_{ECAL} < 1.5$ GeV
- $N_{MUCH} \geq 1$ for the trigger track
- Associated or un-associated MUCH hits in opposite hemisphere to trigger side with $\theta_{acol} < 90°$

[1] An event can contain two trigger tracks if they both fulfill the criteria listed

The track reconstruction efficiency is then defined as:

$$\epsilon(\text{Track Reconstruction}) = \frac{\text{number of 2nd tracks found}}{\text{number of trigger tracks}}, \tag{5.5}$$

where the enumerator counts the number of second tracks that were found for an event in the opposite hemisphere.

Muon Identification Efficiency The muon identification efficiency was calculated in a similar way as for the track reconstruction. Here two tracks with high momentum were required, one of which is well identified as a muon. Events were chosen with the following cuts:

- Two high momentum tracks with p_1 and $p_2 \geq 0.8\ E_{Beam}$
- The acollinearity is small, $\theta_{acol} < 10\,^\circ$
- Tight impact cuts, $IP_z/2$ and $IP_{r\phi}/3$ to values in Table 4.1
- For the muon identification on the trigger side:
  - $N_{MUCH} \geq 1$
  - No Bhabha veto, $E_{ECAL} < 1.5$ GeV
  - $E_{ECAL} < 0.3$ GeV or 0.2 GeV $< E_{HCAL}/(N_{layer} \cdot \cos(\theta)) < 2.0$ GeV

The event was accepted as a muon pair if one of the muon identification criteria as described in section 4.1.2 for the track in the opposite hemisphere was fulfilled (MUCH or ECAL or HAC).

The muon identification efficiency is then defined as:

$$\epsilon(\text{Muon Identification}) = \frac{\text{number of 2nd tracks with muon id found}}{\text{number of trigger tracks}}, \tag{5.6}$$

where the enumerator counts the number of second tracks that were found for an event in the opposite hemisphere with muon identification. The background contamination for both subsamples of events that are used for the calculation of the track reconstruction and the muon identification was found to be negligible.

Figure 5.1 shows the distribution of the track reconstruction efficiency (left), the muon identification efficiency (right) and the single arm efficiency (bottom) as a function of theta for all selected tracks from 183 to 207 GeV.

Detector Cracks The detector contains several so-called '*cracks*' which are caused by small gaps in the boundaries inside or between subdetectors. As there are angular correlations between back-to-back tracks, the losses due to those cracks are not taken into account when calculating the single arm efficiency. If a track was lost in a crack in one hemisphere it was most likely lost in the other hemisphere too. The losses in the detector cracks are modeled in the DELSIM package, thus, the inefficiencies can be derived from simulation as long as the agreement to data is good. Studies have been performed comparing data with simulation in order to evaluate extra corrections in case of discrepancies.

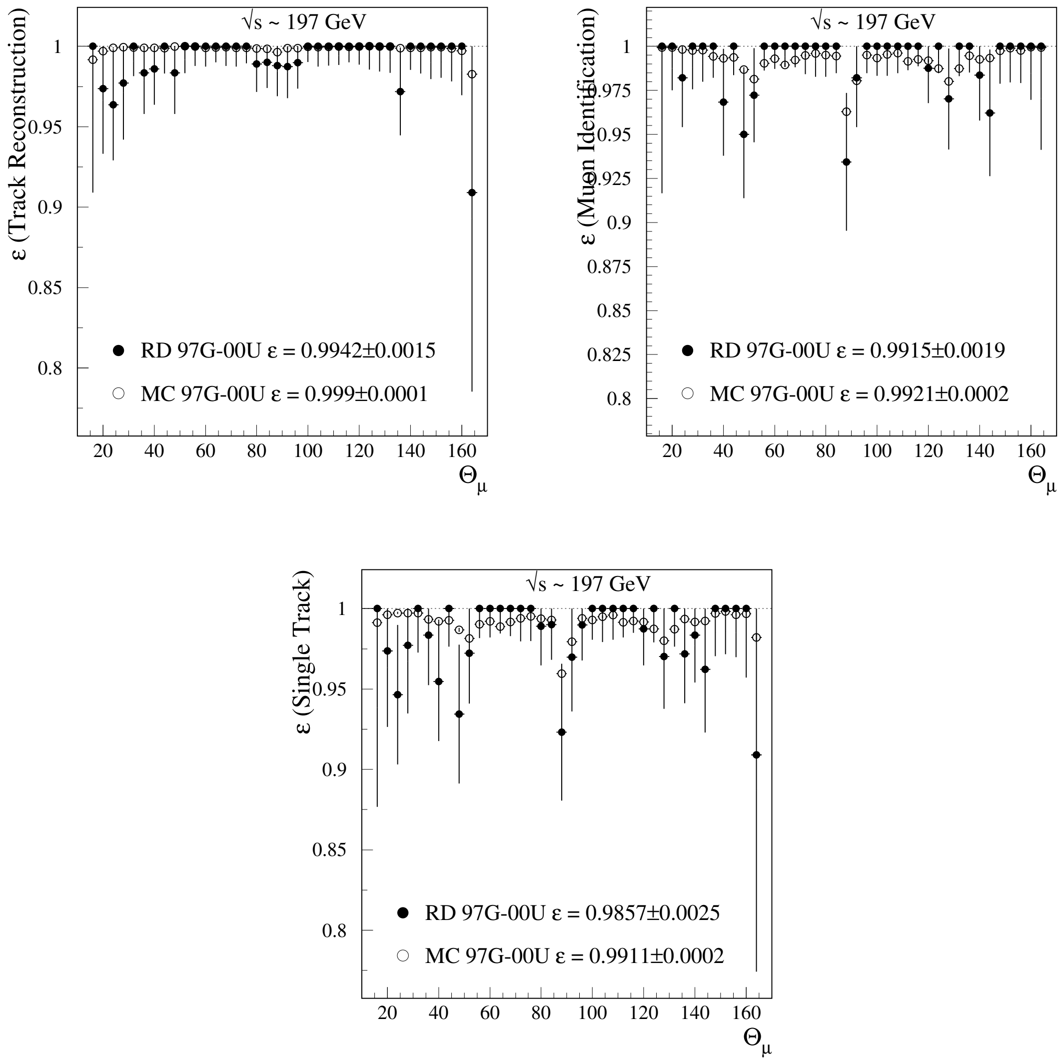

Figure 5.1: Track reconstruction (left), muon identification (right) and single arm efficiency (bottom) as a function of the polar angle, θ, using all data from 183-207 GeV.

Losses in θ The losses in θ are caused by the structure of the DELPHI detector, which is split into two halves. The TPC as well as the muon chambers have sector boundaries at $90°$. The boundary from the barrel to the forward and backward parts of the detector led to inefficiencies at $\approx 40°$ and $\approx 140°$. This can be seen in Figure 5.1. A comparison of the $\cos\theta$ distribution of data and simulation showed a good agreement.

Losses in ϕ The TPC is divided into 6 sectors in the $r\phi$-plane on each side, covering an angle of 60 degrees. Between these sectors the detector has an insensitive zone of $\approx$ $4°$ which is inefficient for the tracking. A distribution of tracks in $\mathrm{mod}(\phi, 60)$ is shown in Figure 5.2. The track loss within the cracks was calculated by interpolating the number of tracks outside the crack region and comparing with the actual number of found tracks. An overall loss of

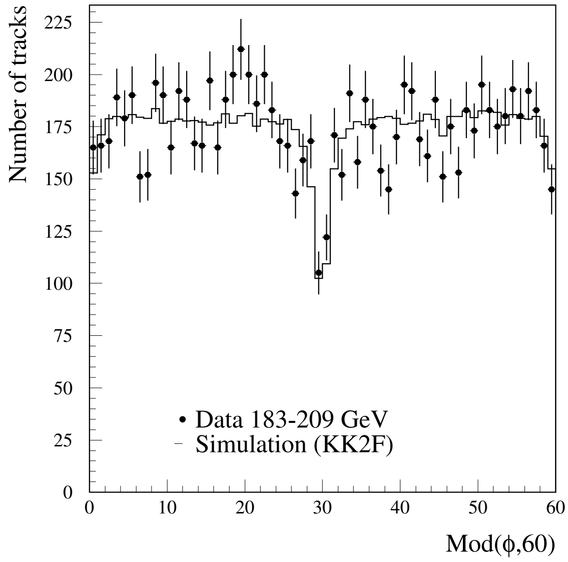

Figure 5.2: A folded distribution in the azimuthal angle, mod(ϕ, 60), of all selected muon tracks in the 183-209 GeV data.

tracks in ϕ of $\approx$ 2.5% was found.

As the agreement between data and simulation is good, no extra corrections due to losses in the detector cracks were applied to the single arm efficiency. The angular correlations such as both tracks disappearing in a gap can only be estimated from simulation. This is taken into account when computing total selection efficiency.

The results for the track reconstruction, muon identification and single arm efficiency are summarized in Table 5.1 and Figure 5.3 (left). The errors given are statistical only. Systematic effects were mainly due to backgrounds and were found to be negligible. Numbers for each energy point within one year of data taking were consistent with each other, therefore, it was reasonable to use all tracks of one year to calculate year-by-year efficiencies. The differences between data and simulation for each year is shown in Figure 5.3 (right). The largest difference was found for the track reconstruction in 1998 and 2000, which is not significant, but consistent within the different years. On average this is found to be (0.48 $\pm$ 0.15)% higher in simulation than in data, whereas the efficiencies for the muon identification agree very well within 0.06%. An overall difference for the single arm efficiency, using all tracks from 183 to 207 GeV combined, by (0.54 $\pm$ 0.2)% is found.

A different method that determines the single arm efficiency directly by combining track reconstruction and muon identification was investigated in an other analysis [37] and showed a good agreement between the obtained results. Nevertheless, the method accepted a higher level of background and was used as a cross check.

In total the selection efficiency can be estimated by separating the following parts:

$$\epsilon_{sel} = \mathcal{C} \cdot \epsilon \text{ (Cuts)} \cdot \epsilon^2 \text{ (Single Arm)}, \tag{5.7}$$

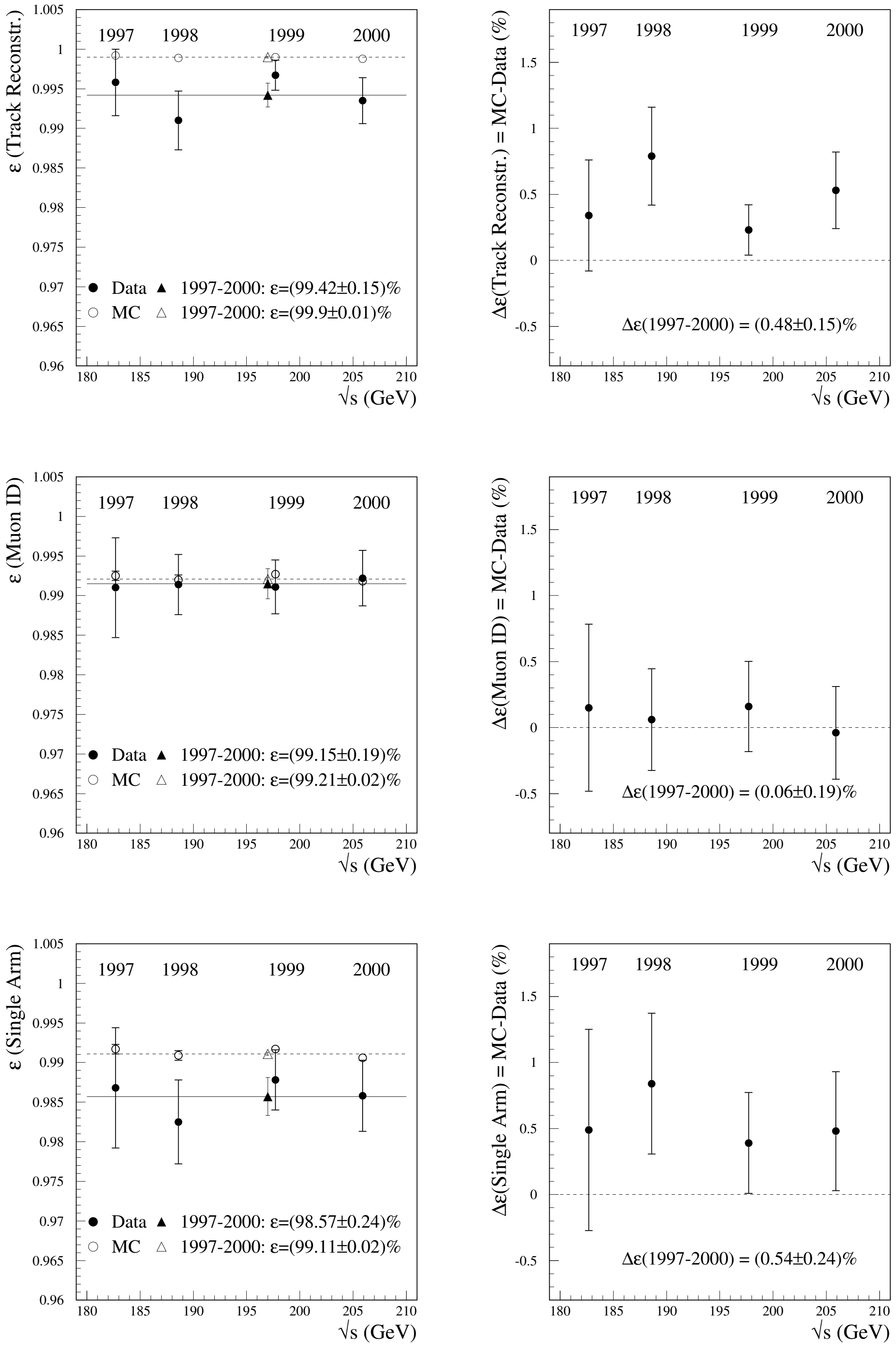

Figure 5.3: Track reconstruction, muon identification and single arm efficiencies (left) and differences between data and simulation (right) as a function of the energy. The triangles reflect the results using all tracks from 183 to 207 GeV.

Year	Energy (GeV)		Efficiency ϵ (%)		
			Track Reconstruction	Muon Identification	Single Arm
1997	183	Data	99.58 $\pm$ 00.42	99.10 $\pm$ 00.63	98.68 $\pm$ 00.76
		KK2F	99.92 $\pm$ 00.02	99.25 $\pm$ 00.06	99.17 $\pm$ 00.06
1998	189	Data	99.10 $\pm$ 00.37	99.14 $\pm$ 00.38	98.25 $\pm$ 00.53
		KK2F	99.89 $\pm$ 00.02	99.20 $\pm$ 00.06	99.09 $\pm$ 00.06
1999	192-	Data	99.67 $\pm$ 00.19	99.11 $\pm$ 00.34	98.78 $\pm$ 00.38
	202	KK2F	99.90 $\pm$ 00.01	99.27 $\pm$ 00.04	99.17 $\pm$ 00.04
2000	205-	Data	99.35 $\pm$ 00.29	99.22 $\pm$ 00.35	98.58 $\pm$ 00.45
	207	KK2F	99.88 $\pm$ 00.01	99.18 $\pm$ 00.03	99.06 $\pm$ 00.03
1997-	183-	Data	99.42 $\pm$ 00.15	99.15 $\pm$ 00.19	98.57 $\pm$ 00.24
2000	207	KK2F	99.90 $\pm$ 00.01	99.21 $\pm$ 00.02	99.11 $\pm$ 00.02

Table 5.1: Results for the track reconstruction, muon identification and single arm efficiencies obtained for the different years from 1997 to 2000 and the global values achieved from using all tracks from 183 to 207 GeV combined.

with $\mathcal{C}$ being a correction factor taking into account topological considerations such as 'cracks' within detector boundaries and angular correlations, ϵ(Cuts) is the efficiency obtained due to the losses by the cuts used in the analysis. Those components have to be evaluated with simulation.

To simplify the method, the components of the selection efficiency derived from simulation were summarised using Equation (5.3) taking into account all losses that were fully described by simulation and correct for the differences observed for the single arm efficiency. Thus, Equation (5.7) can be transformed into:

$$\epsilon_{sel} = \epsilon(\text{Simulation}) \cdot \mathcal{C}_{SA} \tag{5.8}$$

with

$$\mathcal{C}_{SA} = \frac{\epsilon^2_{data}(\text{Single Arm})}{\epsilon^2_{sim}(\text{Single Arm})}. \tag{5.9}$$

where $\mathcal{C}_{SA}$ is the correction factor. Using the results obtained above yielded to the correction factors shown in Figure 5.4. The values for the different years agree well within the errors, therefore, it was reasonable to compute one mean correction factor for all years and energies using the global single arm efficiency calculated from all tracks. This yielded to a correction factor of (98.92 $\pm$ 0.49)% in total.

The following definitions have been used to compute the efficiency from Equation (5.3) for the inclusive sample:

$$\epsilon^{incl}_{sim} = \frac{N_{acc}(\sqrt{s'} > 75\text{GeV})}{N_{gen}(\sqrt{s'} > 75\text{GeV})} \ ,$$

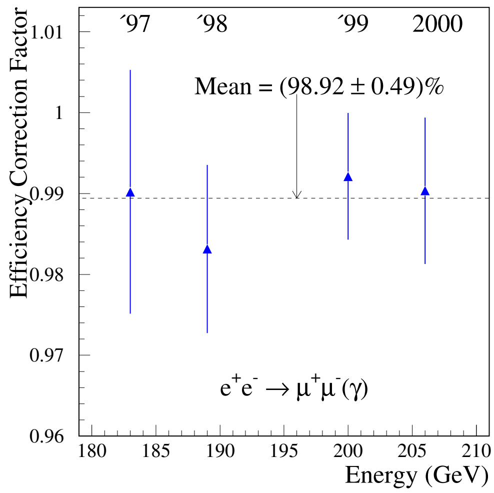

Figure 5.4: Efficiency correction factors, $\mathcal{C}_{SA}$, obtained from the ratio ϵ^2_{data}(Single Arm)/ϵ^2_{sim}(Single Arm) for the different years 1997-2000. The mean value is the one achieved from using the global values for the single arm efficiency.

and for the non-radiative sample:

$$\epsilon^{nrad}_{sim} = \frac{N_{acc}(\sqrt{s'} > 75\text{GeV})}{N_{gen}(\sqrt{s'} > 0.85\sqrt{s})} \ .$$

within the angular acceptance[2]. The definition for the non-radiative events does not take into account the losses due to migration of events down to the inclusive sample ($\sqrt{s'}/\sqrt{s} < 0.85$). This was done with the so-called *Migration Factor*, described in Section 5.1.3.

The results obtained for the corrected selection efficiencies, using simulation samples of the size of $\approx$ 100k generated events, except for 183 GeV and 189 GeV with $\approx$ 50k events, are summarised in Table 5.2.

5.1.2 Trigger Efficiency

The inefficiencies originating from the trigger system are not simulated in the DELSIM package and have to be estimated separately from data. For that, a subsample of events was selected sensitive to two independent trigger components, T_1, T_2, defining N_1 and N_2, the number of events selected with the referring subtrigger, and N_{12}, the number of events selected with both. The efficiency can then be estimated with (for subtrigger configurations and mathematical treatment of two or more independent subtriggers, see [25] and references therein):

$$\epsilon_{trig} = \frac{N_{obs}}{N_{tot}}, \quad \text{where} \quad N_{obs} = N_1 + N_2 - N_{12}, \quad N_{tot} = \frac{N_1 N_2}{N_{12}} \tag{5.10}$$

The trigger efficiencies have been calculated with the muon pairs selected at each energy and in bins of $\cos\theta$ [38]. The numbers were found to be consistent with each other, within

[2]All calculations were done within the angular acceptance of $14° \leq \theta_{\mu^\pm} \leq 166°$.

$\sqrt{s}$	Efficiency ϵ_{sel} (%)		ISR Migration
(GeV)	$\sqrt{s'} > 75$ Gev	$\sqrt{s'}/\sqrt{s} > 0.85$	$\sqrt{s'}/\sqrt{s} > 0.85$
183	90.11 ± 0.47	92.69 ± 0.49	1.0207 ± 0.0021
189	91.69 ± 0.47	93.68 ± 0.50	1.0154 ± 0.0017
192	90.91 ± 0.46	93.11 ± 0.48	1.0179 ± 0.0013
196	91.15 ± 0.46	93.45 ± 0.48	1.0207 ± 0.0013
200	90.92 ± 0.46	93.22 ± 0.48	1.0222 ± 0.0014
202	90.86 ± 0.46	93.22 ± 0.48	1.0217 ± 0.0013
205	91.48 ± 0.46	93.57 ± 0.48	1.0157 ± 0.0013
207E	91.52 ± 0.46	93.60 ± 0.48	1.0164 ± 0.0013
207U	90.36 ± 0.46	92.68 ± 0.48	1.0363 ± 0.0016

Table 5.2: The selection efficiency and the ISR migration factor at different nominal center-of-mass energies. The errors result from the statistics of MC samples and from the correction of the single arm efficiency.

different bins as well as between the different energies, as shown in Figure 5.5. For the 97G and for A0U processing a slight drop in efficiency was seen that was covered by the relatively large errors given by the low statistics. Therefore, it was reasonable to use a global value for the trigger efficiency that was calculated from the total number of events from all energies. The global trigger efficiency used for this analysis is:

$$\epsilon_{trig} = (99.82 \pm 0.07)\%. \tag{5.11}$$

5.1.3 ISR Migration

The number of events selected in the non-radiative class are contaminated by events with a lower true invariant mass ($\sqrt{s'}/\sqrt{s} < 0.85$) due to photon radiation, on the other hand the total number is decreased by events that are lost with a lower invariant mass computed. Those 'up' and 'down' migrations of events that have a wrong reconstructed $\sqrt{s'}$ have to be taken into account when calculating the non-radiative cross section. Figure 5.6 shows the distribution of the reconstructed $\sqrt{s'}/\sqrt{s}$ versus the generated $\sqrt{s'}/\sqrt{s}$ from simulation at 207 GeV with three characteristic regions. Region A contains the ISR impurities from radiative events. Region C reflects the inefficiency for the non-radiative sample. This can be expressed as[3]:

$$\rho_{nr} = \frac{B}{A+B} \qquad \text{and} \qquad \epsilon_{nr} = \frac{B}{B+C}. \tag{5.12}$$

[3]Events are required to have $\sqrt{s'} > 75$ GeV

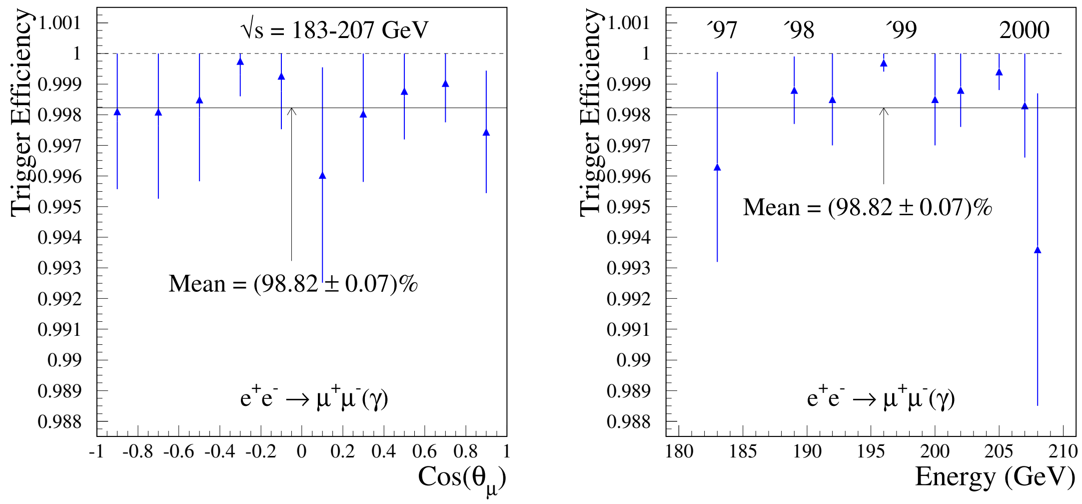

Figure 5.5: Trigger efficiencies in bins of $\cos\theta$, averaged over all energies (left), and trigger efficiencies for different energies (right). The mean value gives the result obtained using the sum of all tracks at different energies and bins.

Typical values are, e.g. at 207 GeV $\rho_{nr} = (98.33 \pm 0.07)\%$ and $\epsilon_{nr} = (96.74 \pm 0.10)\%$. The purity and efficiency were combined as a so-called *ISR Migration Factor*, which is defined as:

$$F_{mig} = \frac{\rho_{nr}}{\epsilon_{nr}} \tag{5.13}$$

Using the definitions of Equation (5.12) this can simply be expressed as:

$$F_{mig} = \frac{\text{total number of generated events with } \sqrt{s'}/\sqrt{s} > 0.85}{\text{total number of reconstructed events with } \sqrt{s'}/\sqrt{s} > 0.85} \tag{5.14}$$

The values for F_{mig} calculated for the different energies from simulation are given in Table 5.2. Impurities for the inclusive sample from events having a $\sqrt{s'}$ below 75 GeV are taken into account as a systematic error given in Section 5.1.6.

5.1.4 Background Estimation

The background contamination from events of other processes than the reaction $\mathrm{e}^+\mathrm{e}^- \to \mu^+\mu^-(\gamma)$ has been reduced to a large extend with the $\sqrt{s'}$-cut and the selection criteria described in Section 4.1.2. Figure 5.7 shows the $\sqrt{s'}$ distribution for events that passed all the selection criteria except that on $\sqrt{s'} = 75$ GeV, above that cut most of the background processes have been rejected. Nevertheless, there was still a certain amount of background events that were selected above the $\sqrt{s'}$-cut and that had to be estimated. The following processes were considered:

- Tau pair production

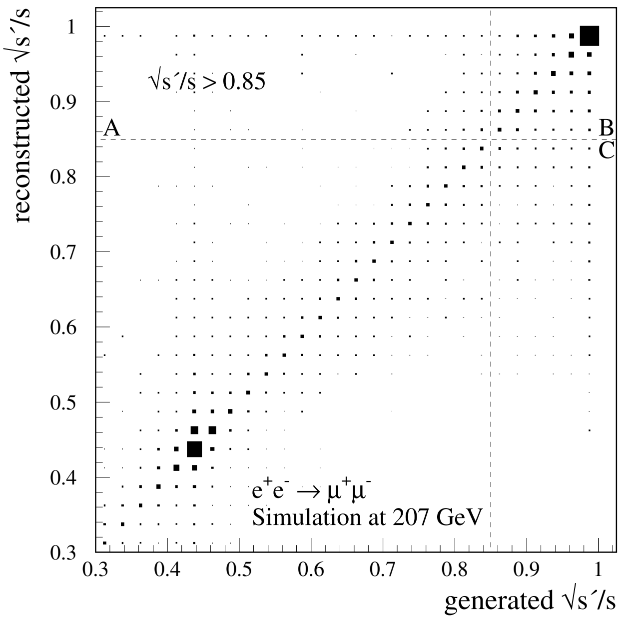

Figure 5.6: Efficiency and purity of the non-radiative events calculated from the distribution of reconstructed versus generated $\sqrt{s'}/\sqrt{s}$.

- 4-Fermion events
- Cosmic ray muons

The estimation of background originating from cosmic ray muons that were passing the detector in coincidence with the BCO[4] signal was done using the real data. As described in Section 4.1.2 the cosmics have an anti-correlated impact distribution in the $r\phi$-plane (see Figure 4.2). This can be used to select those events that passed all selection cuts except for the combined $IP_{r\phi}$-cut, given in Equation (4.1) with cut values given in table 4.1. Assuming them to be cosmic ray muons that are uniformly distributed in $r\phi$, the numbers outside the interaction region can be extrapolated to the central region inside the $IP_{r\phi}$-cut. The number of cosmic background events expected are given in Table 5.4 as a ratio to the number of muon pairs selected.

Except for the cosmic ray muons all backgrounds have been estimated using simulation. The tau pair production, $e^+e^- \to \tau^+\tau^-(\gamma)$, has been simulated with the KK Generator [28]. The 4-fermion events have been divided into 3 separate samples using WPHACT [39]: one sample containing all processes which have only charge currents diagrams (CC), e.g. $\mu^+\mu^-\nu\bar{\nu}$, that is called W^+W^--like, one sample containing all processes which have only neutral current diagrams (NC4F), e.g. $e^+e^-\mu^+\mu^-$, and where the multi-peripheral diagrams are not dominant that is named ZZ-like and a third sample containing neutral current processes that have $\gamma\gamma$-compatible final states that are called Zee-like. The cuts in the phase space used

[4]Beam Cross Over

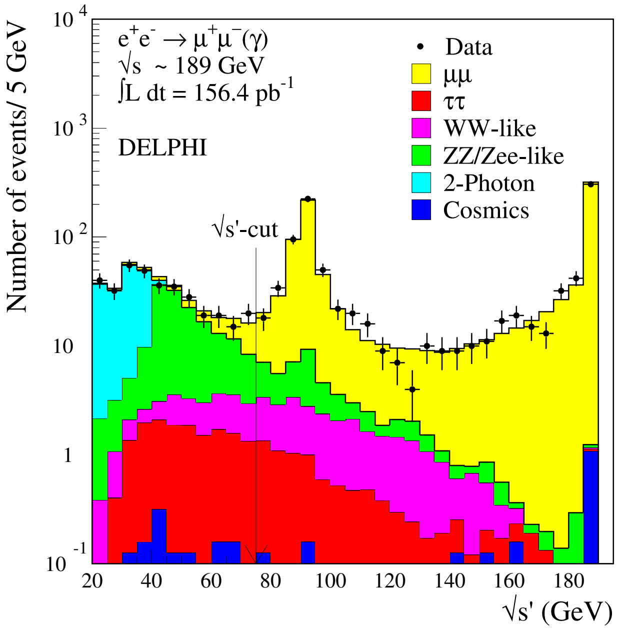

Figure 5.7: Distribution of $\sqrt{s'}$ for all events that passed the selection criteria except that on the $\sqrt{s'}$-cut of 75 GeV at the nominal energy of 189 GeV. The background is shown for the different channels separately.

for the generation of these different subsamples of 4-fermion events can be found in [40]. The pure $\gamma\gamma$ region, the two-photon collisions, that are not included in the WPHACT samples are generated by the dedicated BDKRC [41] code. The amount of background events coming from this process, with having a relatively low invariant mass ($m_{\mu\mu} < 40\,\mathrm{GeV}/c^2$), are negligible after applying the $\sqrt{s'}$-cut as can be seen in Figure 5.7. Events coming from the Bhabha process and hadronic decays, simulated with the BHWIDE [42] and KK generator, respectively, were found to be negligible. The generators used and the equivalent integrated luminosity for the signal and the different background channels for each energy are shown in table 5.3.

The background contamination from the physics processes was estimated by calculating the efficiency of selecting those events with respect to the total number of events generated. This gave the expected background in pico barns as the cross section for the simulated events was known. In addition, a correction had to be applied for the ZZ-like and Zee-like samples, where the expected background from $ee\mu\mu$-events with generated $m_{ee} < 0.2\,\mathrm{GeV}/c^2$ was missing in simulation. The missing background had to be estimated by extrapolating the selection efficiency for $ee\mu\mu$-events from the known to the unknown region. For that purpose a bigger sample of 400k Zee-like events was used. This yielded to $\epsilon = (26.7 \pm 2.6)\%$ (NC4F) and $\epsilon = (54.7 \pm 1.9)\%$ (NCGG) using all MC of the energies considered, see Figure 5.8. As the cross section for these processes is increasing with low m_{ee}, this was a not negligible amount of background. A fraction of $\sim 8\%$ and $\sim 21\%$ of the calculated background from the ZZ-like and Zee-like samples had to be added at all energies, respectively. The error on the correction arises from the uncertainty of the efficiency determination.

Equivalent integrated luminosity of the generators used $(fb)^{-1}$						
Channel	$\mu^+\mu^-$	$\tau^+\tau^-$	W$^+$W$^-$-like	ZZ-like	Zee-like	2-Photon
Energy	KK2f		WPHACT			BDKRC
(GeV)	$\mu\mu$	$\tau\tau$	CC	NC4F	NCGG	
183	~ 5	~ 23	~ 6	~ 12	~ 3	~ 0.1
189	~ 5	~ 24	~ 5	~ 12	~ 3	~ 0.1
192	~ 11	~ 25	~ 5	~ 7	~ 3	~ 0.1
196	~ 12	~ 26	~ 5	~ 12	~ 4	~ 0.1
200	~ 12	~ 28	~ 5	~ 14	~ 7	~ 0.1
202	~ 13	~ 28	~ 3	~ 13	~ 3	~ 0.1
205	~ 13	~ 29	~ 5	~ 13	~ 3	~ 0.1
207E	~ 13	~ 19	~ 5	~ 13	~ 3	~ 0.1
207U	~ 13	~ 22	~ 5	~ 6	~ 3	~ 0.1

Table 5.3: Generators and equivalent luminosities used for the simulation of the signal and each background channel at different center-of-mass energies.

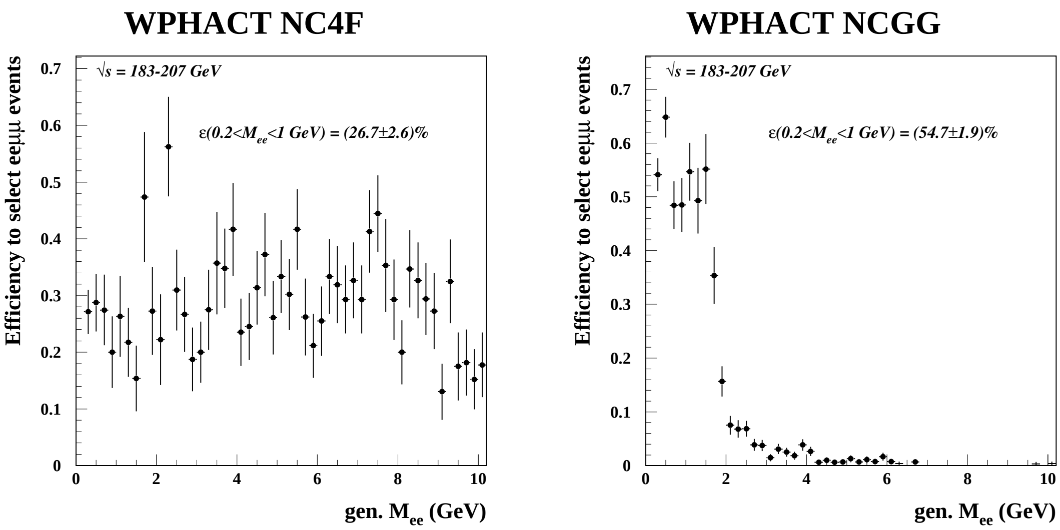

Figure 5.8: The efficiency to select $ee\mu\mu$ events in the ZZ-like (left) and Zee-like (right) samples of WPHACT as a function of the generated $m(ee)$.

For the non-radiative class of events the background contamination caused by physics processes is very small. Therefore, the single channels of background that were found were added up at each energy and the total background, except cosmic ray muons, was computed from a linear fit to the sum of all backgrounds, in order to reduce fluctuations from the statistics of simulation. The largest contribution comes from the ZZ-like events and, with increasing energy, from W^+W^--like events. The contamination caused by cosmics was estimated in the same way as for the inclusive class by evaluating the ratio of cosmic events that were reconstructed above $\sqrt{s'}/\sqrt{s} > 0.85$.

The obtained results for the background estimation for the inclusive and non-radiative class can be found in Table 5.4. The number of events related to the cross sections given in pico barns can be computed with $N_{bgd} = \mathcal{L} \cdot \sigma_{bgd}$. The error is mainly due to the statistics of the MC samples used. An extra error on the theoretical uncertainty of the generators was included, which is 0.4% on the $\tau\tau$-channel, a 5% error on the W^+W^--like and ZZ-like samples and a 15% error on the Zee-like sample [43]. For the non-radiative class a global theoretical uncertainty of 10% was included. The resulting total background together with the single channels is illustrated in Figure 5.9.

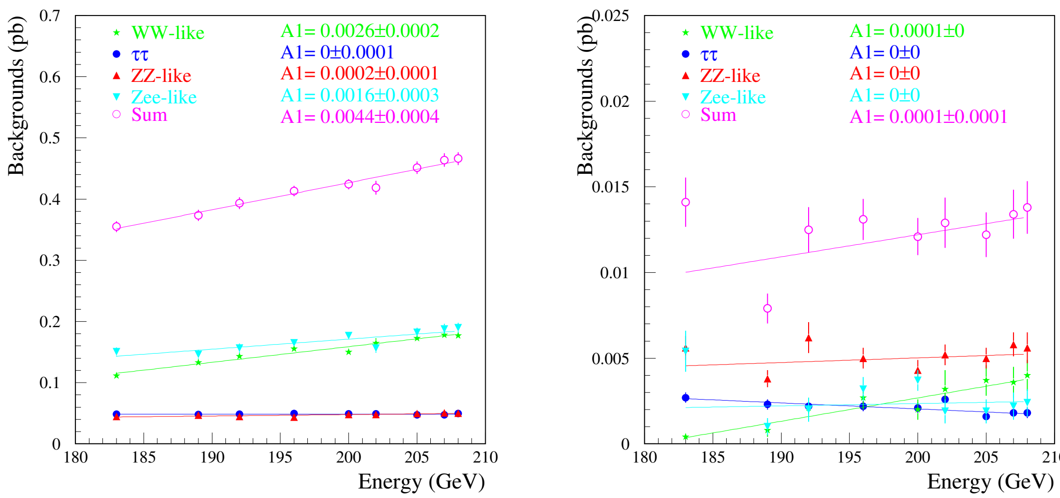

Figure 5.9: The background cross sections expected for the inclusive (left) and non-radiative (right) class for the different energies.

5.1.5 Angular Acceptance

In order to obtain comparable results for the total cross section to the predictions from the ZFITTER program [33], the number of events selected in the angular acceptance of $14° \leq \theta_{\mu^\pm} \leq 166°$ had to be corrected to the full solid angle. ZFITTER allows only three options: (1) no cuts are used, (2) a cut on the maximum acollinearity and the minimum of the fermion's momenta were placed or (3) a cut on the minimum invariant mass of the fermion pair is done. When using one of the cut options the angular acceptance of the anti-fermion can be defined, but not on both fermions as applied in this analysis. Thus, it is reasonable to make the comparison to the predictions within the full solid angle. The acceptance corrections were done with the fully simulated KK MC samples of the size given in Table 5.3, computing the ratio of number of generated events within the full polar angle

Background Contamination of the $e^+e^- \to \mu^+\mu^-(\gamma)$ process, $\sqrt{s'} > 75$ GeV					
Energy (GeV)	$\tau^+\tau^-$ (pb)	W^+W^--like (pb)	ZZ-like (pb)	Zee-like (pb)	Cosmics (%)
183	0.048 ± 0.001	0.112 ± 0.004	0.044 ± 0.002	0.150 ± 0.007	0.35 ± 0.05
189	0.047 ± 0.001	0.133 ± 0.005	0.047 ± 0.002	0.150 ± 0.007	0.42 ± 0.04
192	0.049 ± 0.001	0.143 ± 0.009	0.045 ± 0.003	0.156 ± 0.025	0.31 ± 0.03
196	0.049 ± 0.001	0.155 ± 0.010	0.043 ± 0.003	0.165 ± 0.026	0.31 ± 0.03
200	0.049 ± 0.001	0.150 ± 0.009	0.048 ± 0.003	0.177 ± 0.027	0.31 ± 0.03
202	0.049 ± 0.001	0.165 ± 0.012	0.048 ± 0.003	0.156 ± 0.025	0.31 ± 0.03
205	0.048 ± 0.001	0.172 ± 0.010	0.049 ± 0.003	0.182 ± 0.028	0.45 ± 0.04
207E	0.047 ± 0.002	0.178 ± 0.011	0.051 ± 0.003	0.188 ± 0.029	0.45 ± 0.04
207U	0.050 ± 0.002	0.177 ± 0.011	0.050 ± 0.004	0.190 ± 0.030	0.45 ± 0.04

Background Contamination at $\sqrt{s'}/\sqrt{s} > 0.85$		
Energy (GeV)	$\sum(\tau\tau, WW, \mathrm{ZZ}, Zee)$ (pb)	Cosmics (%)
183	0.010 ± 0.003	0.35 ± 0.05
189	0.011 ± 0.002	0.49 ± 0.05
192	0.011 ± 0.003	0.32 ± 0.03
196	0.012 ± 0.003	0.32 ± 0.03
200	0.012 ± 0.003	0.32 ± 0.03
202	0.012 ± 0.003	0.32 ± 0.03
205	0.013 ± 0.003	0.44 ± 0.04
207E	0.013 ± 0.003	0.44 ± 0.04
207U	0.013 ± 0.003	0.44 ± 0.04

Table 5.4: Expected background cross sections for the different physics channels for the inclusive class and as a sum of all for the non-radiative class at different center-of-mass energies. The cosmic events are given as a ratio to the number of selected muon pairs.

to the number of generated events within the angular acceptance. The obtained correction factors used for the calculation of the cross section at each energy are summarised in Table 5.5. The corrections are higher for the inclusive class as due to the photon radiation more events are expected to be in the very forward and backward region. The errors given arise from the statistics of the MC samples.

Energy	Correction factors to the full solid angle, $\eta_{4\pi}$	
(GeV)	$\sqrt{s'} > 75$ GeV	$\sqrt{s'}/\sqrt{s} > 0.85$
183	1.1053 ± 0.0015	1.0513 ± 0.0017
189	1.1034 ± 0.0015	1.0462 ± 0.0016
192	1.1093 ± 0.0011	1.0499 ± 0.0012
196	1.1084 ± 0.0011	1.0473 ± 0.0011
200	1.1154 ± 0.0011	1.0497 ± 0.0012
202	1.1183 ± 0.0011	1.0518 ± 0.0011
205	1.1206 ± 0.0011	1.0510 ± 0.0012
207	1.1202 ± 0.0011	1.0488 ± 0.0012

Table 5.5: Correction factors to the full solid angle, $\eta_{4\pi}$, used for the calculation of the cross section for both classes, the inclusive and the non-radiative events.

5.1.6 Systematic Errors

The uncertainties of the different components of corrections propagating into the systematic error of $\sigma_{\mu\mu}$ and other possible sources have been investigated and are discussed below.

Selection Efficiency One of the largest contributions to the systematic error on $\sigma_{\mu\mu}$ is originating from the selection efficiency, especially for the non-radiative measurement. The error on the efficiency is dominated by the uncertainty on the difference that was found for the single arm efficiency between data and simulation. The accuracy was limited by the statistics in data usable for its determination, which is 0.49%. Smaller contributions come from the statistics of the simulation (0.11%) and the trigger efficiency (0.07%).

Angular Acceptance The error on the angular acceptance corrections originates from the statistics of simulated $e^+e^- \rightarrow \mu^+\mu^-(\gamma)$ events that were used for the evaluation and yields to a value between 0.14% and 0.10%. These errors are uncorrelated.

ISR Purity The uncertainty on the reconstruction of $\sqrt{s'}$ is taken into account when calculating the Migration Factor, F_{mig}, whose error arises from the statistics of the KK MC. This yielded to an error on $\sigma_{\mu\mu}$ of 0.1-0.2%, which is not correlated. The difference in F_{mig} when switching on and off the beam energy spread in the simulation is an additional systematic error on the $\sqrt{s'}$ reconstruction for the non-radiative measurement. This amounts to 0.1% and is correlated between energies and years. For the inclusive measurement the impurity of radiative events below 75 GeV leads to an estimated error of 0.2%.

Background The errors due to background physics processes were explained above. They originate from the statistics of simulation, the theoretical precision of the generators and the missing background events in the WPHACT generator. The error from the cosmic rays arises from the uncertainty on the extrapolation from the outside region of vertex cuts to the inside vertex region. The detailed errors on $\sigma_{\mu\mu}$ from the single background channels can be found in 5.12.

QED radiative Corrections Differences due to missing higher orders in the QED radiative corrections have been calculated using the Coherent Exclusive Exponentiation (CEEX) scheme [44] implemented in the KK MC generators. The error quoted, 0.09%, is estimated by comparing the $\mathcal{O}(\alpha^1)$ to the $\mathcal{O}(\alpha^2)$ calculations. Corrections due to Initial-Final state QED Interference (IFI) are not necessary since IFI at $\mathcal{O}(\alpha^2)$ is included in the KK MC generator. This is the main benefit from the CEEX scheme with respect to the EEX matrix element, that is implemented in the KORALZ generator [45] (no IFI) used in previous analyses.

Luminosity The uncertainties from the determination of the luminosity have three sources:

- The statistical error of the number of selected Bhabha events that were used for the evaluation of the luminosity
- The systematic error arising from the experimental evaluation, coming from uncertainties to the STIC acceptance, errors in the position of the beam spot, the error in the beam energy and imprecision in the simulation of the STIC detector, which is in total evaluated to be 0.5%
- The systematic error on the theoretical prediction of the $e^+e^- \to e^+e^-$ process arising from the photonic corrections, which is 0.12% [46]

5.1.7 Results

The number of selected events at different center-of-mass energies are summarised in Table 5.6, for the inclusive and the non-radiative sample. The total number of events correspond to the selection criteria described in Section 4.1. The number of events selected in the forward and backward hemisphere, defined as being forward or backward when $\cos\theta_{\mu^-} > 0$ or $\cos\theta_{\mu^-} < 0$, respectively, include in addition those events that were selected in runs where no luminosity information was available, as for the A_{FB} measurement this is not a necessary information.

The results for the total cross section measured for the reaction $e^+e^- \to \mu^+\mu^-(\gamma)$ are shown in Table 5.7, together with the Standard Model prediction computed with the ZFITTER program (version 6.36). The result for 207 GeV is obtained by averaging the cross section at 207E and 207U using the BLUE [47] technique. The error on the measurement of $\sigma_{\mu\mu}$ at a single energy is dominated by the statistical error. However, combining all events at the considered energies from 183 to 207 GeV yields to a statistical error of $\sim 1.8\%$. The systematic effects relevant for this level of precision have been investigated.

All errors, statistical and systematic, together with their correlations are summarised in Table 5.12. The different systematic sources are divided into those that are either fully correlated between energies or years, and those that are not correlated at all. In addition, the correlation between different channels or experiments is given which is relevant when using these results combined with other 2-fermion channels as in fits beyond the Standard Model.

Number of events selected, N_{sel}						
	for $\sigma_{\mu\mu}$		for $A_{FB}^{\mu\mu}$			
Energy	$\sqrt{s'} > 75$ GeV	$\sqrt{s'}/\sqrt{s} > 0.85$	$\sqrt{s'} > 75$ GeV		$\sqrt{s'}/\sqrt{s} > 0.85$	
(GeV)	tot	tot	fwd	bwd	fwd	bwd
183	379	165	250	131	129	36
189	991	424	668	323	337	87
192	167	64	109	58	52	12
196	389	179	256	133	141	38
200	506	223	345	163	172	51
202	205	88	142	65	68	21
205	373	155	249	129	131	29
207E	426	181	299	127	140	41
207U	248	116	172	79	93	24
total	3684	1595	2490	1208	1263	339

Table 5.6: The number of events selected in total and in the forward/backward hemisphere for the inclusive and the non-radiative sample at different nominal energies from 183 to 207 GeV. The number of events in forward/backward hemisphere contain also events from runs which have no luminosity information.

5.2 The Forward-Backward Asymmetry

The forward-backward asymmetry, A_{FB}, can simply be expressed in terms of the cross sections in the forward and backward hemisphere:

$$A_{FB} = \frac{\sigma_f - \sigma_b}{\sigma_f + \sigma_b}, \tag{5.15}$$

where the forward region is being defined as $\cos\theta_{\mu^-} > 0$ and the backward region with $\cos\theta_{\mu^-} < 0$. The luminosity cancels down and σ can be replaced by the number of selected events in the according hemisphere:

$$A_{FB} = \frac{N_f - N_b}{N_f + N_b}. \tag{5.16}$$

σ ($e^+e^- \to \mu^+\mu^-$) (pb)				
$\sqrt{s}$	$\sqrt{s'} > 75$ GeV		$\sqrt{s'}/\sqrt{s} > 0.85$	
(GeV)	Measurement	Theory	Measurement	Theory
183	$8.387 \pm 0.455 \pm 0.074$	7.560	$3.618 \pm 0.284 \pm 0.030$	3.304
189	$7.157 \pm 0.243 \pm 0.063$	7.007	$3.053 \pm 0.150 \pm 0.024$	3.072
192	$7.410 \pm 0.613 \pm 0.069$	6.760	$2.832 \pm 0.357 \pm 0.023$	2.967
196	$5.882 \pm 0.325 \pm 0.057$	6.452	$2.751 \pm 0.207 \pm 0.022$	2.837
200	$6.935 \pm 0.333 \pm 0.065$	6.162	$3.069 \pm 0.207 \pm 0.024$	2.713
202	$5.704 \pm 0.436 \pm 0.057$	6.017	$2.486 \pm 0.267 \pm 0.020$	2.650
205	$5.477 \pm 0.314 \pm 0.057$	5.807	$2.320 \pm 0.188 \pm 0.019$	2.560
207	$5.457 \pm 0.233 \pm 0.058$	5.702	$2.470 \pm 0.145 \pm 0.019$	2.515

Table 5.7: The obtained results for the cross section measurements together with the ZFITTER predictions. The first error given is statistical, the second the systematic error. The result for 207 GeV was obtained by averaging the cross section at 207E and 207U.

Therefore, the A_{FB} measurement becomes a simple counting experiment of $e^+e^- \to \mu^+\mu^-(\gamma)$ events. Some corrections have to be applied to the number of selected events:

$$N_{f/b} = (N^{sel}_{f/b} - N^{bgd}_{f/b} - N^{Qmis}_{f/b}) \cdot \eta^{2\pi}_{f/b} \cdot \mathcal{C}^{\epsilon}_{f/b}, \qquad (5.17)$$

where

$$\begin{aligned} N^{sel} &= \text{number of events with } \mu^- \text{ in forward/backward} \\ N^{bgd} &= \text{number of background events expected} \\ N^{Qmis} &= \text{number of charge misidentified events expected} \\ \eta^{2\pi} &= \text{angular acception correction} \\ \mathcal{C}^{\epsilon} &= \text{efficiency correction factor} \end{aligned}$$

5.2.1 Background Estimation

The subtraction of background events was done in a similar way as for the cross section, here in the forward and backward hemisphere separately. The number of events selected from the simulation of the different physics background channels was normalised to the luminosity of the according data samples and then subtracted from the number observed in the data. The cosmic ray muons have $A^{\mu\mu}_{FB} = 0$, therefore, the ratio of background estimated for the cross section was subtracted from both hemispheres. Migrations from events with $\sqrt{s'}/\sqrt{s}$ well below 0.85 to the non-radiative class may also shift $A^{\mu\mu}_{FB}$ to lower values. Thus, the ratio of expected *radiative returns* ($A^{\mu\mu}_{FB}(Z^0) \approx 0$), calculated with simulation, was subtracted from both hemispheres.

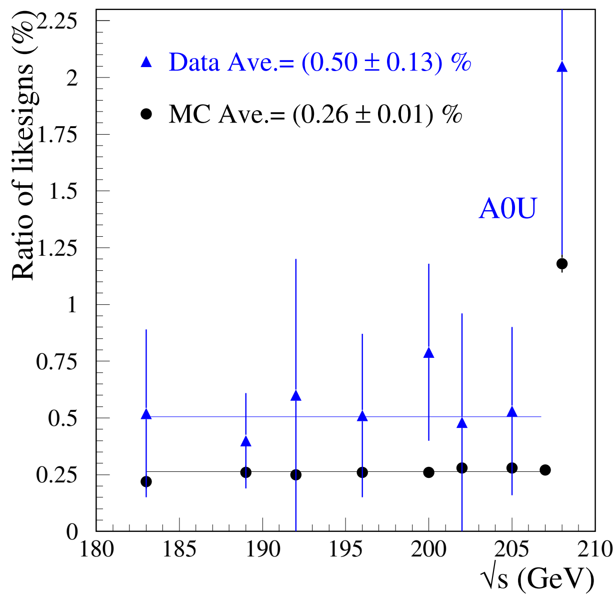

Figure 5.10: The like-sign ratio found in real data and expected with simulation for the different energies. The average given is obtained without the 207U sample.

5.2.2 Like-sign Events

Events where both tracks have the same charge due to mismeasurement of the curvature of one of the tracks are so-called like-sign events. Those events were selected in this analysis as well. For the cross section measurement those events don't cause any bias, as for the total number of events the charge is not relevant (as long as a real dimuon event was selected). For the $\mathrm{A}_{\mathrm{FB}}^{\mu\mu}$ measurement, the polar angle of the negatively charged muon is of major importance. Thus, a redefinition of the sign for both tracks had to be made when a like-sign event was selected. The sign of the track with the worse momentum resolution ($\Delta p/p$), compared to the other track was changed in such an event[5]. The charge reclaim efficiency using this method was probed with simulation showing stable values at the the different energies and yielding to $\epsilon_Q = (96.4 \pm 0.6)\%$ on average.

The ratio of like-signs in data was found to be $(0.50 \pm 0.13)\%$ on average (without 207U: $2.1 \pm 0.8\%$), whereas in simulation only $(0.26 \pm 0.01)\%$ were expected, a factor of two smaller, this is shown in Figure 5.10. The difference is supposed to come from insufficient simulated short tracks and a residual overestimation of the momentum resolution in simulation (after smearing of the momentum of the tracks as described in Section 4.1.3). In the barrel region the number of tracks which have an association to the OD and, thus, a good $1/p$ resolution is smaller in data than in simulation. Furthermore, an excess of like-signs was found at a polar angle of 90°, the gap between the detector halves, and in the very forward end-caps.

The number of misidentified like-sign events was evaluated by splitting the ratio into two halves, one half with a computed charge reclaim efficiency, and one half, not simulated, for

[5] This was consistent with using Δp

which the reclaim efficiency had to be estimated:

$$R_{Qmisid} = (1 - \epsilon_Q^{sim}) \cdot \frac{R_{LS}}{2} + (1 - \epsilon_Q^{notsim}) \cdot \frac{R_{LS}}{2}.$$

The ratio of inefficient reconstructed like-signs from simulation on average is $(3.6 \pm 0.6)\%$. The reclaim efficiency for the unknown half was estimated from the polar angle region where the excess of like-signs was found. There, a slight drop was seen and was estimated to $\epsilon_Q^{notsim} = (90 \pm 10)\%$. The expected ratio of events where the charge reconstruction failed, is then:

$$R_{Qmisid} = (0.035 \pm 0.025)\%.$$

Assuming the ratio of misidentified like-signs to be relatively constant over the polar angle - as the statistics is very low this can be stated within the given error - one will expect more events moving from the forward to the backward hemisphere than vice versa. Thus, the number of misidentified events expected can be determined by:

$$N_{f/b}^{Qmis} = (N_{b/f}^{sel} - N_{f/b}^{sel}) \cdot R_{Qmisid}, \tag{5.18}$$

which means that those events are added to the forward region and subtracted from the backward region. The amount of events where the charge of both tracks were incorrectly assigned was found to be negligible.

5.2.3 Angular Acceptance

The correction to the full solid angle was done with the KK MC for the forward and backward hemisphere separately with the same method as described for $\sigma_{\mu\mu}$ in Section 5.1.5. The obtained values can be found in Table 5.8.

5.2.4 Efficiency Correction

The simplification used in Equation (5.16) by counting the events in the forward and backward region is only true if the corrections, as the efficiency and the ISR migration, is the same for both hemispheres. This is not necessarily so, as one can see in Figure 5.11, where the selection efficiency from simulation for the total number of events as well as for the forward and the backward hemisphere at different energies is shown. For the inclusive class a difference of $\sim 1\%$ between forward and backward on average was found.

A correction has been done taking into account a lower efficiency expected in the backward region, by correcting the number of events in the backward with respect to the number of events in the forward. The following factor has been used for the energies from 183 to 207E GeV:

$$\mathcal{C}_b^\epsilon = \epsilon_f / \epsilon_b = 1.011 \pm 0.003 \qquad \text{and} \qquad \mathcal{C}_f^\epsilon = 1 \pm 0.$$

For 207U the correction was larger: $\mathcal{C}_b^\epsilon = 1.024 \pm 0.006$. No correction was necessary for the non-radiative class, as on average the difference between forward and backward hemisphere for ϵ and F_{mig}, the ISR migration factor, is compatible to 0, see Figure 5.11 (right). The uncertainty on this differences was taken into account as a systematic error.

Correction factors to the full solid angle, $\eta_{2\pi}$				
Energy	$\sqrt{s'} > 75$ GeV		$\sqrt{s'}/\sqrt{s} > 0.85$	
(GeV)	fwd	bwd	fwd	bwd
183	1.0992 ± 0.0018	1.1172 ± 0.0027	1.0603 ± 0.0020	1.0183 ± 0.0023
189	1.0946 ± 0.0018	1.1207 ± 0.0027	1.0514 ± 0.0019	1.0272 ± 0.0027
192	1.0992 ± 0.0013	1.1298 ± 0.0020	1.0566 ± 0.0014	1.0251 ± 0.0018
196	1.0978 ± 0.0013	1.1296 ± 0.0020	1.0525 ± 0.0013	1.0287 ± 0.0019
200	1.1082 ± 0.0013	1.1296 ± 0.0020	1.0571 ± 0.0014	1.0235 ± 0.0018
202	1.1109 ± 0.0013	1.1331 ± 0.0020	1.0596 ± 0.0014	1.0234 ± 0.0017
205	1.1125 ± 0.0013	1.1367 ± 0.0020	1.0588 ± 0.0014	1.0240 ± 0.0018
207	1.1116 ± 0.0013	1.1373 ± 0.0020	1.0553 ± 0.0014	1.0250 ± 0.0018

Table 5.8: Correction factors to the full solid angle, $\eta_{2\pi}$ used for the determination of the forward-backward asymmetry for both classes, the inclusive and the non-radiative events.

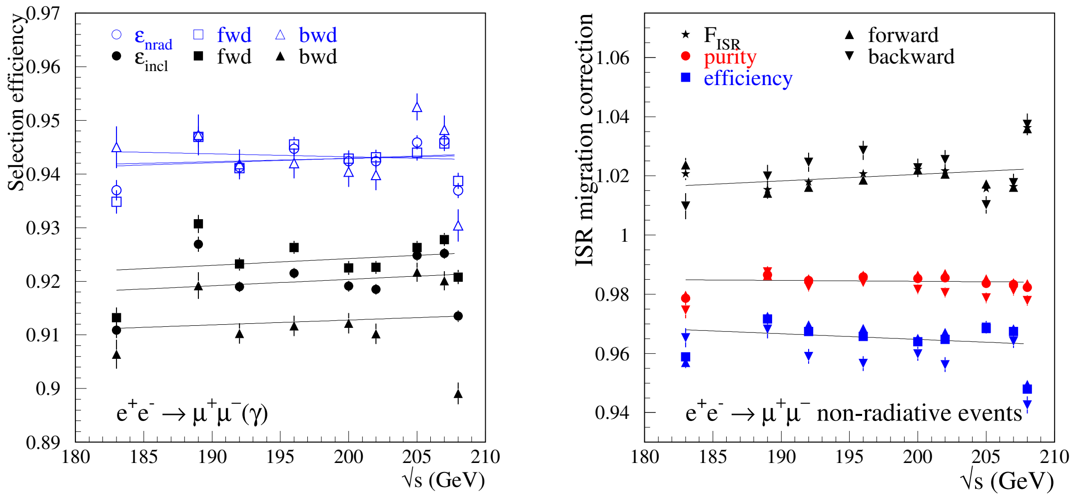

Figure 5.11: The efficiencies (left) and ISR migration correction factors (right) in total, in the forward and in the backward hemisphere for the different energies.

5.2.5 Systematic Errors

The different sources of systematic errors are discussed in the following, a summary of all errors together with their correlations can be found in Table 5.13.

Background As described in Section 5.1.6 the error on the subtraction of the background has three sources, one is due to the statistics of simulation alone, one is the error of the prediction of the background cross section, and a third error is quoted for the WPHACT NC4F and NCGG samples where events with generated $m_{ee} < 0.2$ GeV were missing in simulation. The error from the cosmic ray subtraction originates from the extrapolation to the beam spot region.

Charge Misidentification The error on the number of events with a wrong charge identification after reconstruction of the like-signs is dominated by the uncertainty of the reclaim efficiency for the non-simulated half of like-sign events. The error propagating to the uncertainty on $\mathrm{A}_{\mathrm{FB}}^{\mu\mu}$ amounts to $2 \cdot 10^{-4}$ and $3 \cdot 10^{-4}$ for the inclusive and non-radiative sample, respectively ($4/6 \cdot 10^{-4}$ in 207U).

$\sqrt{s'}$ **Reconstruction** The error on the correction of mismeasurement of $\sqrt{s'}$ that led to migrations from the inclusive to the non-radiative class is coming from the statistics in simulation used at each energy to calculate the contamination. The error is $< 3 \cdot 10^{-4}$ and is not correlated between energies.

Angular Acceptance and Efficiency Correction The uncertainty on the angular acceptance correction applied on both hemispheres separately comes from the statistics of the $\mathrm{e}^+\mathrm{e}^- \to \mu^+\mu^-(\gamma)$ MC at each energy used for the evaluation. The error on $\mathrm{A}_{\mathrm{FB}}^{\mu\mu}$ caused by the efficiency correction in the inclusive class arises from the error of the averaged correction factor for the backward hemisphere. It is therefore correlated between energies and years and amounts to $12 \cdot 10^{-4}$. For the non-radiative class the differences in the forward and backward efficiency was very small and was taken into account as a systematic error of $4 \cdot 10^{-4}$.

QED radiative Corrections Possible differences in $\mathrm{A}_{\mathrm{FB}}^{\mu\mu}$ due to missing higher orders in the QED radiative corrections have been estimated by using the old EEX scheme in simulation for the calculations of corrections. The uncertainty amounts to be $1 \cdot 10^{-4}$.

5.2.6 Results

The number of the selected events in the forward and the backward hemisphere for the $\mathrm{A}_{\mathrm{FB}}^{\mu\mu}$ measurement is summarised in Table 5.6, together with the total number of events. The obtained results for $\mathrm{A}_{\mathrm{FB}}^{\mu\mu}$, together with the predictions from theory, can be found in Table 5.9.

5.3 The differential Cross Section

In addition to the total cross section and the forward-backward asymmetry, a measurement of the non-radiative differential cross section in bins of $\cos\theta_{\mu^-}$ has been made, where θ_{μ^-} is the polar angle of the negatively charged muon with respect to the beam axis. The calculation

A_{FB} ($e^+e^- \rightarrow \mu^+\mu^-$)				
$\sqrt{s}$	$\sqrt{s'} > 75$ GeV		$\sqrt{s'}/\sqrt{s} > 0.85$	
(GeV)	Measurement	Theory	Measurement	Theory
183	$0.301 \pm 0.051 \pm 0.003$	0.329	$0.583 \pm 0.064 \pm 0.001$	0.596
189	$0.334 \pm 0.032 \pm 0.003$	0.327	$0.601 \pm 0.039 \pm 0.001$	0.589
192	$0.289 \pm 0.078 \pm 0.003$	0.327	$0.638 \pm 0.098 \pm 0.001$	0.586
196	$0.298 \pm 0.052 \pm 0.004$	0.326	$0.586 \pm 0.061 \pm 0.001$	0.582
200	$0.347 \pm 0.044 \pm 0.003$	0.324	$0.558 \pm 0.056 \pm 0.001$	0.578
202	$0.361 \pm 0.069 \pm 0.004$	0.324	$0.544 \pm 0.090 \pm 0.001$	0.577
205	$0.300 \pm 0.053 \pm 0.004$	0.323	$0.652 \pm 0.061 \pm 0.001$	0.574
207	$0.382 \pm 0.039 \pm 0.006$	0.323	$0.579 \pm 0.048 \pm 0.001$	0.573

Table 5.9: The results from the $A_{FB}^{\mu\mu}$ measurement for the inclusive and non-radiative class together with the prediction from ZFITTER for the different energies considered.

was done in 10 bins within the angular acceptance of $|\cos\theta| < 0.97$, using the following formula:

$$\frac{d\sigma_i}{d\cos\theta_i} = \frac{N_i^{sel} - N_i^{bgd} - N_i^{Qmis}}{\epsilon_i^{tot} \cdot \Delta_i \cdot \mathcal{L}} \cdot F_i^{mig} \quad , \tag{5.19}$$

where for each bin i:

$$\begin{aligned} N^{sel} &= \text{number of events selected} \\ N^{bgd} &= \text{number of background events expected} \\ N^{Qmis} &= \text{number of charge misidentified events expected} \\ \epsilon^{tot} &= \text{total efficiency} \\ F^{mig} &= \text{migration factor} \\ \Delta &= \text{bin width of} \cos\theta \\ \mathcal{L} &= \text{integrated luminosity} \end{aligned}$$

Most of the corrections, like the selection efficiency, the background subtraction and the ISR migration, were evaluated bin-by-bin, in the same way as for the total cross section as described in detail in Section 5.1. The values for each bin used for the corrections can be found in the Appendix B. For the efficiency correction, which accounts for the differences in data and simulation, and the trigger efficiency the global values were used for all bins. The correction for charge misidentified muon pairs that were not correctly reconstructed from like-sign events was applied for each bin. Assuming a clear back-to-back signature for non-radiative events the migration of μ^- to μ^+ and vice versa is expected to end up in opposite bins of $\cos\theta$. The correction is similar to Equation (5.18) used for the A_{FB} measurement:

$$N_i^{Qmis} = (N_{nbin-i+1}^{sel} - N_i^{sel}) \cdot R_{Qmisid}, \quad \text{with nbin} = 10. \tag{5.20}$$

As a normalisation to the bin width was done, 0.2 and 0.17 for bin 2-9 and bin 1,10, respectively, no acceptance correction was necessary. Corrections were made on the experimental cuts on the polar angle of both muons using simulation. These were significant only in the bins with largest $|\cos\theta|$. The obtained angular distributions for the non-radiative, and for completeness for the inclusive events, within the angular acceptance in comparison to simulation are given in Figures 5.12 to 5.14.

5.3.1 Systematic Errors

The systematic errors on $\frac{d\sigma_{\mu\mu}}{d\cos\theta}$ were divided in those completely uncorrelated uncertainties due to bin-by-bin corrections and those that are completely correlated between bins, energies, years, channels or experiments. The errors are dominated by the efficiency and ISR migration corrections for each bin which depend on the statistics in simulation used for their evaluation and which differ from bin to bin. Another important contribution comes from the error on the efficiency correction, taking into account for the differences in the single arm efficiency in data and simulation, and the uncertainty from the luminosity measurement. Both are fully correlated between bins.

Bin-by-bin migrations that are due to wrongly reconstructed events in θ and leading to distortions in the differential distributions, are very small, because the angular resolution of 0.01° is much smaller than the bin width. From simulation the migrations were found to be negligible.

5.3.2 Results

The obtained results in 10 bins of $\cos\theta$ for the different energies from 183 to 207 GeV are summarised in Tables 5.10 and 5.11 together with their theoretical predictions for each bin. The results for the A0E and A0U processing at 207 GeV have been averaged using the BLUE method. The first error given is the measured statistical error, the second error is the uncorrelated systematic error which resulted from the bin-by-bin corrections. The total systematic error is obtained by adding the correlated errors, given in Table 5.12 for the total cross section, in quadrature. Figures 5.15 and 5.16 illustrate the results in comparison with the Standard Model predictions given from the ZFITTER program.

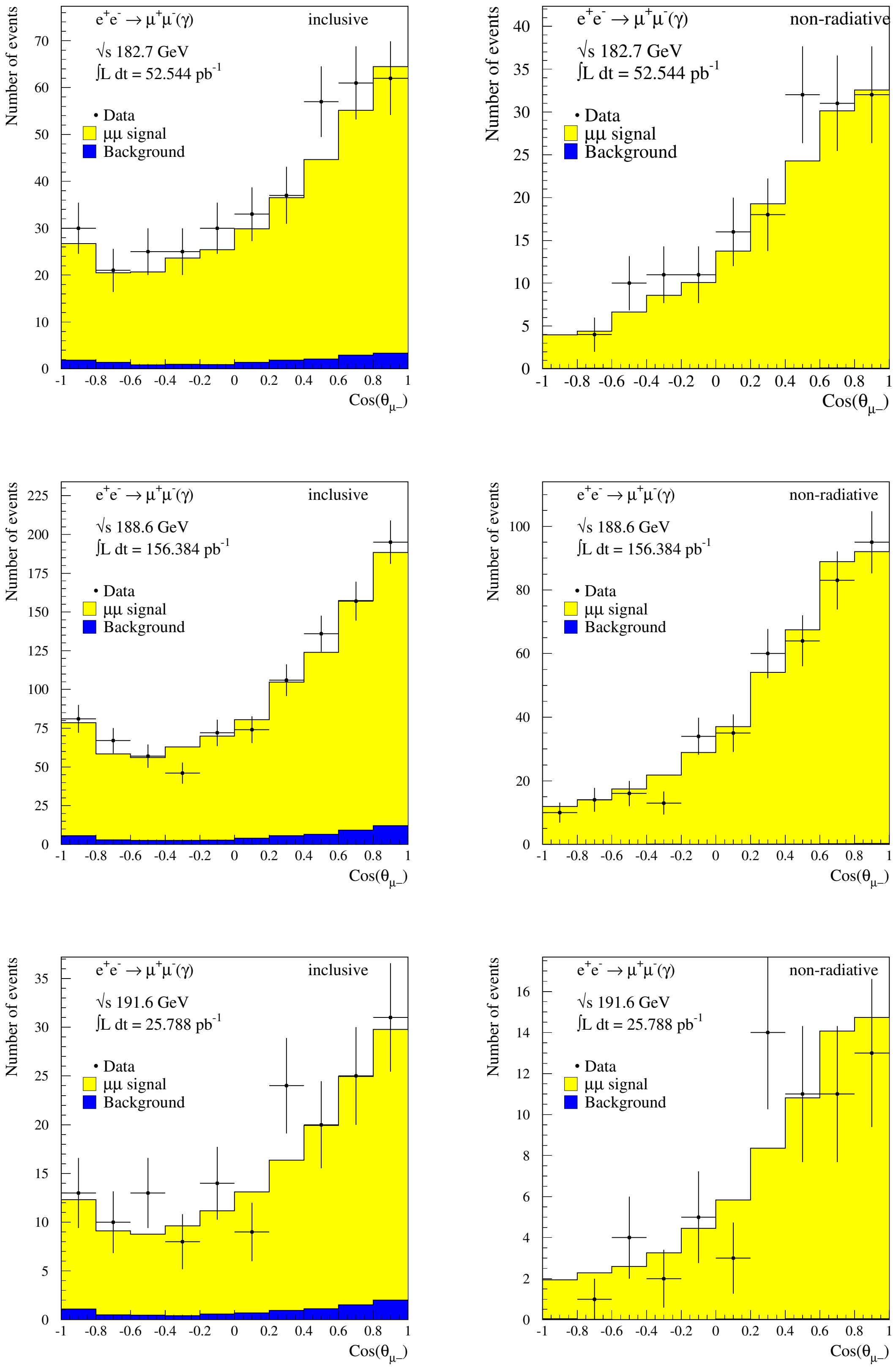

Figure 5.12: Angular distributions for the inclusive (left) and non-radiative (right) events in comparison to the simulation of signal and background at 183-192 GeV, $|\cos\theta_\mu| \leq 0.97$.

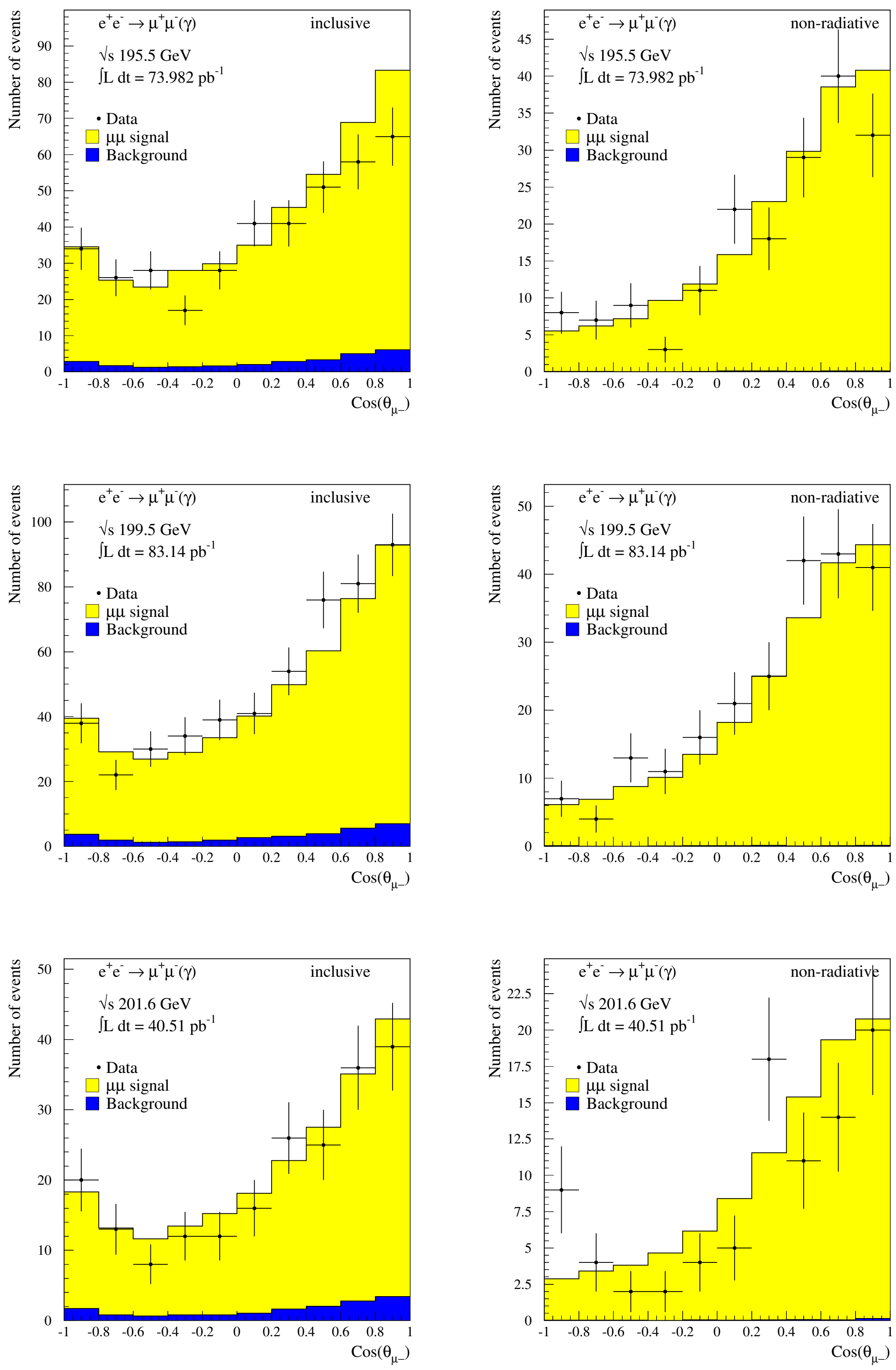

Figure 5.13: Angular distributions for the inclusive (left) and non-radiative (right) events in comparison to the simulation of signal and background at 196-202 GeV, $|\cos\theta_\mu| \leq 0.97$.

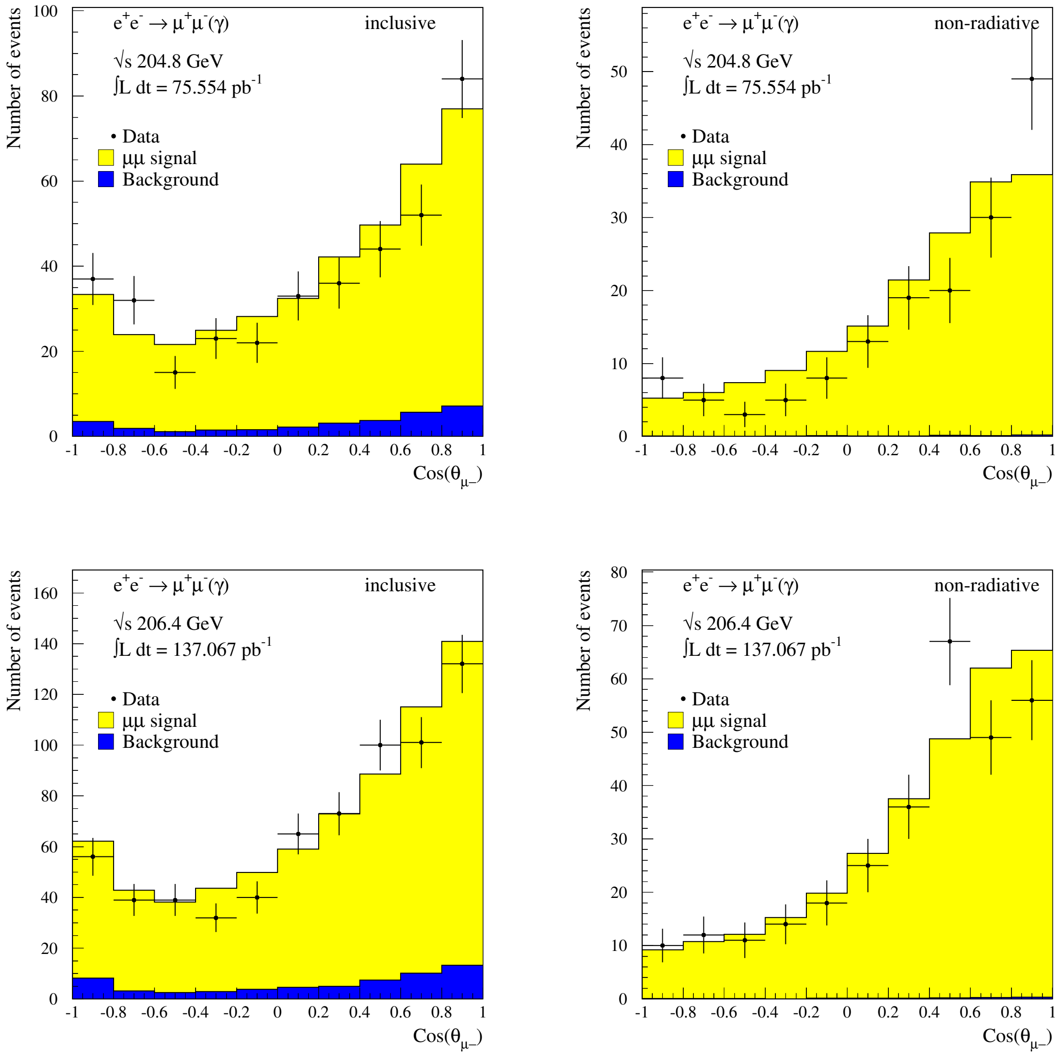

Figure 5.14: Angular distributions for the inclusive (left) and non-radiative (right) events in comparison to the simulation of signal and background at 205-207 GeV, $|\cos\theta_\mu| \leq 0.97$.

$\sqrt{s} \sim 183$ GeV		
	$d\sigma/d\cos\theta$ (pb)	
$\cos\theta$	Theory	Measurement
[-0.97,-0.80]	0.473	-0.006±0.000±0.001
[-0.80,-0.60]	0.481	0.412±0.211±0.007
[-0.60,-0.40]	0.574	1.000±0.321±0.014
[-0.40,-0.20]	0.763	1.065±0.330±0.010
[-0.20, 0.00]	1.049	1.141±0.347±0.012
[0.00, 0.20]	1.436	1.687±0.426±0.017
[0.20, 0.40]	1.923	1.794±0.426±0.012
[0.40, 0.60]	2.515	3.339±0.592±0.024
[0.60, 0.80]	3.219	3.296±0.595±0.022
[0.80, 0.97]	3.998	4.067±0.721±0.030

$\sqrt{s} \sim 189$ GeV		
	$d\sigma/d\cos\theta$ (pb)	
$\cos\theta$	Theory	Measurement
[-0.97,-0.80]	0.460	0.408±0.130±0.007
[-0.80,-0.60]	0.463	0.469±0.129±0.006
[-0.60,-0.40]	0.544	0.539±0.139±0.007
[-0.40,-0.20]	0.714	0.435±0.123±0.004
[-0.20, 0.00]	0.976	1.211±0.210±0.013
[0.00, 0.20]	1.330	1.247±0.212±0.012
[0.20, 0.40]	1.779	2.025±0.263±0.013
[0.40, 0.60]	2.327	2.191±0.275±0.013
[0.60, 0.80]	2.980	2.862±0.315±0.016
[0.80, 0.97]	3.704	3.903±0.402±0.023

$\sqrt{s} \sim 192$ GeV		
	$d\sigma/d\cos\theta$ (pb)	
$\cos\theta$	Theory	Measurement
[-0.97,-0.80]	0.453	-0.014±0.000±0.001
[-0.80,-0.60]	0.454	0.206±0.213±0.002
[-0.60,-0.40]	0.530	0.830±0.416±0.007
[-0.40,-0.20]	0.692	0.420±0.303±0.004
[-0.20, 0.00]	0.942	1.094±0.491±0.009
[0.00, 0.20]	1.282	0.672±0.395±0.006
[0.20, 0.40]	1.715	2.979±0.799±0.017
[0.40, 0.60]	2.243	2.269±0.689±0.009
[0.60, 0.80]	2.873	2.295±0.696±0.009
[0.80, 0.97]	3.572	3.220±0.896±0.013

$\sqrt{s} \sim 196$ GeV		
	$d\sigma/d\cos\theta$ (pb)	
$\cos\theta$	Theory	Measurement
[-0.97,-0.80]	0.444	0.683±0.244±0.008
[-0.80,-0.60]	0.442	0.506±0.194±0.005
[-0.60,-0.40]	0.512	0.649±0.217±0.005
[-0.40,-0.20]	0.664	0.218±0.131±0.002
[-0.20, 0.00]	0.900	0.843±0.257±0.008
[0.00, 0.20]	1.223	1.709±0.368±0.014
[0.20, 0.40]	1.634	1.333±0.318±0.008
[0.40, 0.60]	2.137	2.078±0.388±0.008
[0.60, 0.80]	2.740	2.915±0.463±0.012
[0.80, 0.97]	3.409	2.753±0.489±0.011

Table 5.10: Results for the differential cross sections obtained with non-radiative $e^+e^- \to \mu^+\mu^-$ events at 183-196 GeV together with the predictions. The first error given is the measured statistical error, the second error is the uncorrelated systematic error.

$\sqrt{s} \sim 200$ GeV		
	$d\sigma/d\cos\theta$ (pb)	
$\cos\theta$	Theory	Measurement
[-0.97,-0.80]	0.434	0.527±0.204±0.007
[-0.80,-0.60]	0.431	0.256±0.131±0.003
[-0.60,-0.40]	0.495	0.831±0.232±0.007
[-0.40,-0.20]	0.638	0.709±0.217±0.006
[-0.20, 0.00]	0.861	1.099±0.277±0.010
[0.00, 0.20]	1.167	1.439±0.317±0.011
[0.20, 0.40]	1.558	1.658±0.335±0.010
[0.40, 0.60]	2.038	2.718±0.421±0.011
[0.60, 0.80]	2.614	2.797±0.428±0.011
[0.80, 0.97]	3.254	3.180±0.498±0.014

$\sqrt{s} \sim 202$ GeV		
	$d\sigma/d\cos\theta$ (pb)	
$\cos\theta$	Theory	Measurement
[-0.97,-0.80]	0.429	1.433±0.480±0.017
[-0.80,-0.60]	0.425	0.536±0.271±0.006
[-0.60,-0.40]	0.486	0.255±0.184±0.002
[-0.40,-0.20]	0.624	0.264±0.192±0.002
[-0.20, 0.00]	0.841	0.557±0.283±0.005
[0.00, 0.20]	1.139	0.709±0.321±0.005
[0.20, 0.40]	1.520	2.446±0.580±0.013
[0.40, 0.60]	1.988	1.447±0.440±0.006
[0.60, 0.80]	2.550	1.874±0.504±0.008
[0.80, 0.97]	3.176	3.137±0.706±0.012

$\sqrt{s} \sim 205$ GeV		
	$d\sigma/d\cos\theta$ (pb)	
$\cos\theta$	Theory	Measurement
[-0.97,-0.80]	0.421	0.671±0.239±0.008
[-0.80,-0.60]	0.415	0.354±0.163±0.004
[-0.60,-0.40]	0.473	0.202±0.120±0.001
[-0.40,-0.20]	0.605	0.344±0.157±0.003
[-0.20, 0.00]	0.812	0.565±0.204±0.004
[0.00, 0.20]	1.098	0.946±0.266±0.007
[0.20, 0.40]	1.465	1.329±0.307±0.007
[0.40, 0.60]	1.916	1.401±0.317±0.006
[0.60, 0.80]	2.459	2.161±0.397±0.009
[0.80, 0.97]	3.064	4.232±0.607±0.019

$\sqrt{s} \sim 207$ GeV		
	$d\sigma/d\cos\theta$ (pb)	
$\cos\theta$	Theory	Measurement
[-0.97,-0.80]	0.417	0.468±0.146±0.005
[-0.80,-0.60]	0.411	0.474±0.129±0.003
[-0.60,-0.40]	0.466	0.419±0.129±0.004
[-0.40,-0.20]	0.595	0.542±0.144±0.005
[-0.20, 0.00]	0.798	0.712±0.158±0.007
[0.00, 0.20]	1.078	0.998±0.197±0.008
[0.20, 0.40]	1.438	1.390±0.231±0.006
[0.40, 0.60]	1.881	2.614±0.320±0.010
[0.60, 0.80]	2.413	1.930±0.278±0.008
[0.80, 0.97]	3.008	2.646±0.256±0.011

Table 5.11: Results for the differential cross sections obtained with non-radiative $e^+e^- \to \mu^+\mu^-$ events at 200-207 GeV together with the predictions. The first error given is the measured statistical error, the second error is the uncorrelated systematic error.

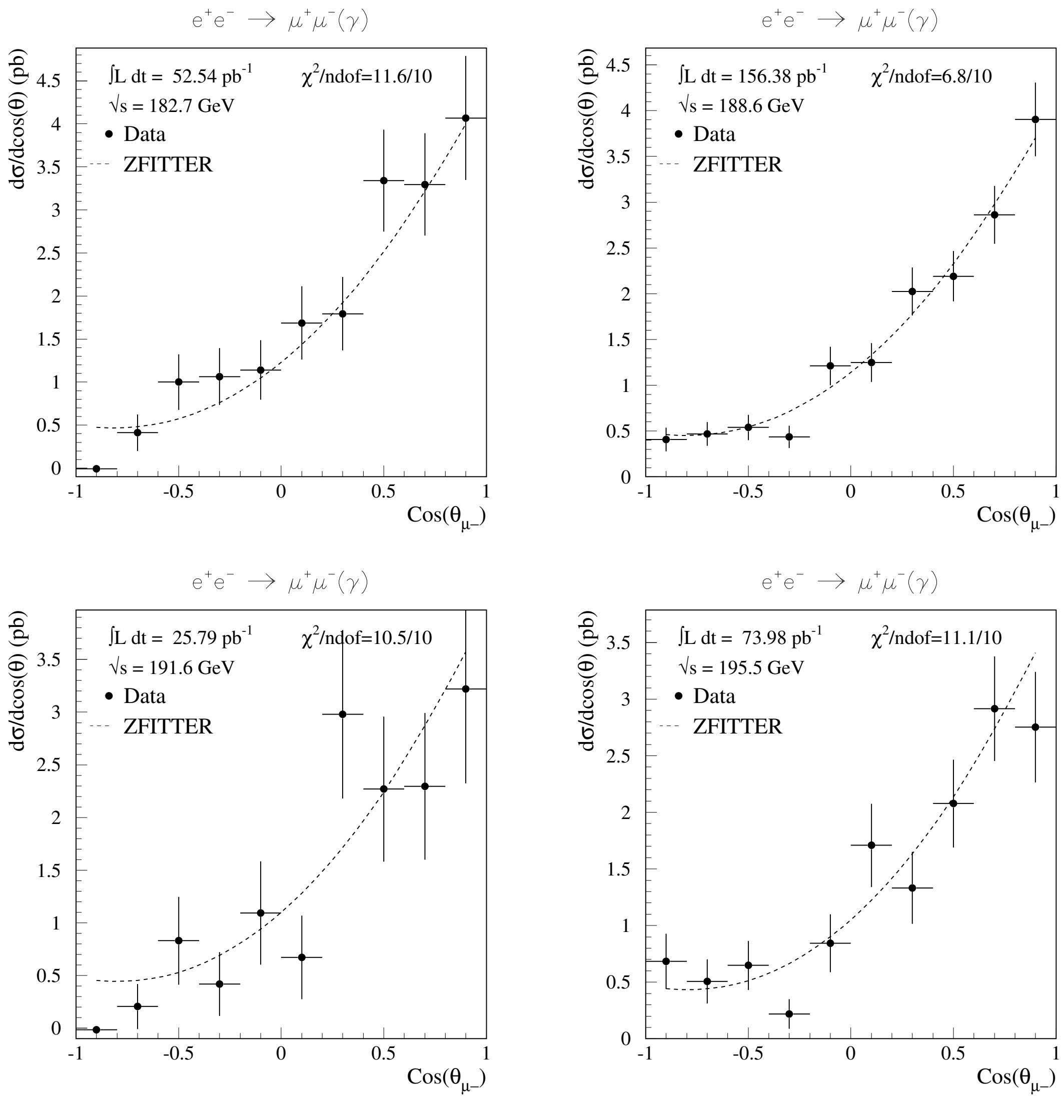

Figure 5.15: The differential cross sections obtained with non-radiative events in comparison to the ZFITTER prediction at 183-196 GeV.

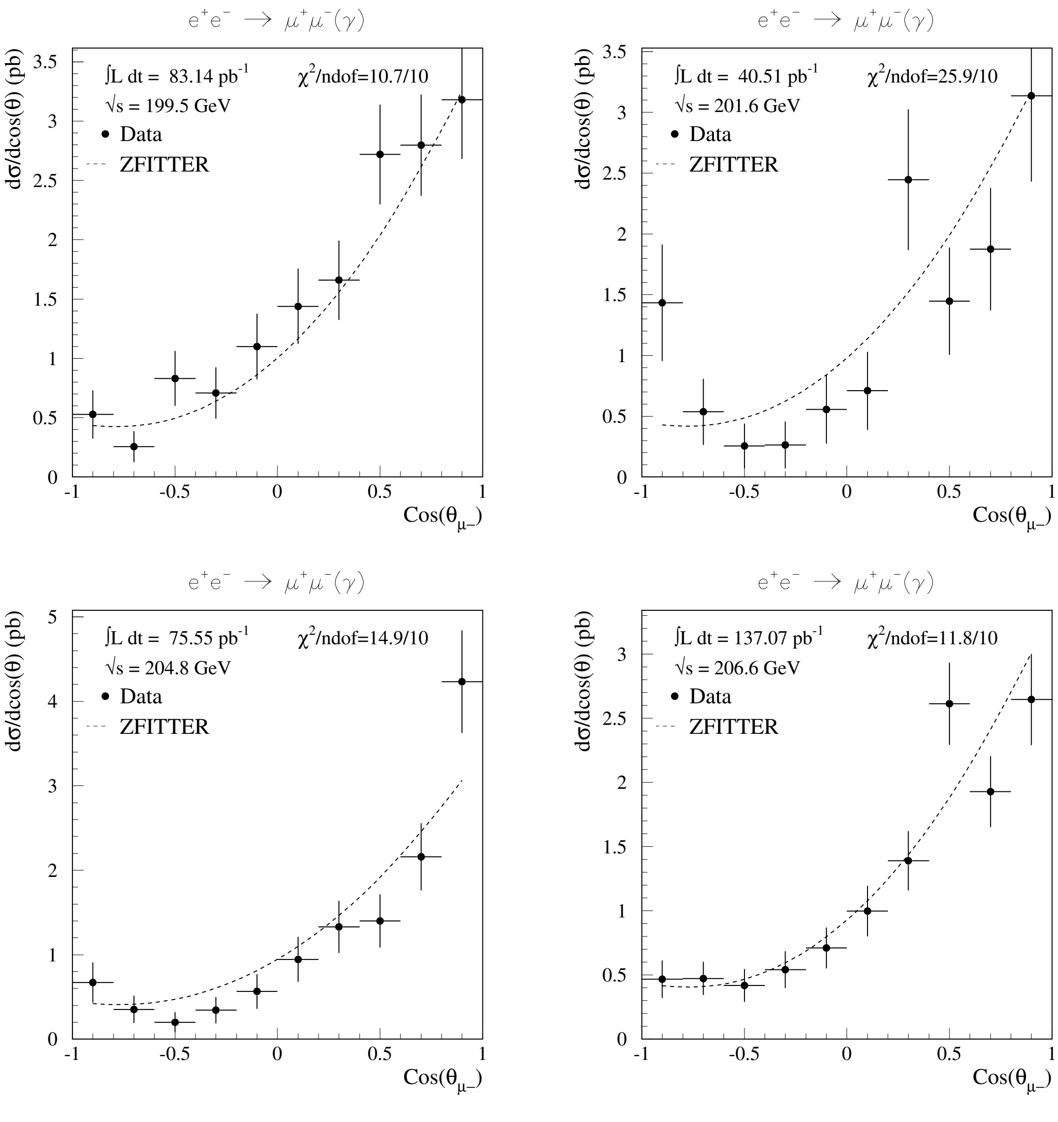

Figure 5.16: The differential cross sections obtained with non-radiative events in comparison to the ZFITTER prediction at 200-207 GeV.

Statistical and systematic errors on the inclusive $\sigma_{\mu\mu}(\%)$										
Error		Corr YECX	Energy (GeV) 183	189	192	196	200	202	205	207
$\Delta\sigma_{\mathrm{stat}}$		UUUU	5.43	3.39	8.27	5.52	4.79	7.64	5.73	4.27
$\Delta\sigma_{\mathrm{syst}}$		—	0.88	0.89	0.93	0.97	0.94	1.00	1.04	1.06
eff	mc	UUUU	0.16	0.15	0.11	0.11	0.11	0.11	0.11	0.10
	dif	CCUU	0.49	0.49	0.49	0.49	0.49	0.49	0.49	0.49
	trig	CCUU	0.07	0.07	0.07	0.07	0.07	0.07	0.07	0.07
	4π	UUUU	0.14	0.14	0.10	0.10	0.10	0.10	0.10	0.10
ISR mig.		CCUU	0.20	0.20	0.20	0.20	0.20	0.20	0.20	0.20
WW	mc	UUUU	0.06	0.08	0.09	0.11	0.10	0.18	0.13	0.10
	thry	CCCC	0.08	0.11	0.12	0.16	0.13	0.18	0.19	0.20
ZZ	mc	UUUU	0.03	0.03	0.04	0.04	0.03	0.04	0.04	0.03
	thry	CCCC	0.03	0.04	0.04	0.05	0.04	0.05	0.06	0.06
	miss	CCUU	0.01	0.01	0.01	0.01	0.01	0.01	0.01	0.01
Zee	mc	UUUU	0.09	0.10	0.10	0.11	0.08	0.13	0.15	0.11
	thry	CCCC	0.33	0.37	0.39	0.51	0.47	0.51	0.61	0.64
	miss	CCUU	0.06	0.07	0.07	0.07	0.06	0.09	0.10	0.11
$\tau\tau$	mc	UUUU	0.02	0.02	0.02	0.03	0.02	0.03	0.03	0.03
	thry	CCCC	0.00	0.00	0.00	0.00	0.00	0.00	0.00	0.00
Cosmics		CUUU	0.06	0.04	0.03	0.03	0.03	0.03	0.04	0.04
QED ISR		CCCC	0.09	0.09	0.09	0.09	0.09	0.09	0.09	0.09
Statistical and systematic errors on the non-radiative $\sigma_{\mu\mu}(\%)$										
Error		YECX	183	189	192	196	200	202	205	207
$\Delta\sigma_{\mathrm{stat}}$		UUUU	7.84	4.90	12.60	7.53	6.75	10.76	8.12	5.87
$\Delta\sigma_{\mathrm{syst}}$		—	0.82	0.80	0.83	0.79	0.79	0.82	0.82	0.80
eff	mc	UUUU	0.20	0.19	0.14	0.14	0.14	0.14	0.14	0.10
	dif	CCUU	0.49	0.49	0.49	0.49	0.49	0.49	0.49	0.49
	trig	CCUU	0.07	0.07	0.07	0.07	0.07	0.07	0.07	0.07
	4π	UUUU	0.16	0.15	0.11	0.11	0.11	0.10	0.10	0.10
F_{mig}		UUUU	0.21	0.17	0.13	0.13	0.14	0.13	0.13	0.10
ISR mig.		CCUU	0.10	0.10	0.10	0.10	0.10	0.10	0.10	0.10
Bgd	mc	UUUU	0.06	0.05	0.10	0.09	0.07	0.11	0.11	0.08
	thry	CCCC	0.03	0.04	0.05	0.05	0.05	0.06	0.06	0.06
	miss	CCUU	0.03	0.03	0.05	0.04	0.04	0.06	0.06	0.06
Cosmics		CUUU	0.05	0.05	0.03	0.03	0.03	0.03	0.04	0.04
QED ISR		CCCC	0.02	0.02	0.02	0.02	0.02	0.02	0.02	0.02
Common error on luminosity (%)										
lumi	stat	UUCU	0.17	0.11	0.30	0.19	0.18	0.26	0.20	0.15
	syst	CCCU	0.50	0.50	0.50	0.50	0.50	0.50	0.50	0.50
	thry	CCCC	0.12	0.12	0.12	0.12	0.12	0.12	0.12	0.12

Table 5.12: The statistical and systematic errors with a breakdown of the different sources of the systematic error for the inclusive and non-radiative total cross section, together with their correlations between different years (Y), energies (E), final states (C) and experiments (X). (U) has no correlation, (C) is fully correlated.

Statistical and systematic errors on the inclusive A_{FB} (in units of 10^{-2})										
Error		Corr YECX	Energy (GeV) 183	189	192	196	200	202	205	207
ΔA_{FB}stat		UUUU	5.08	3.15	7.80	5.18	4.42	6.96	5.31	3.94
ΔA_{FB}syst		—	0.31	0.33	0.32	0.38	0.34	0.39	0.42	0.56
eff	mc	CCUU	0.12	0.12	0.12	0.12	0.12	0.12	0.12	0.17
	4π	UUUU	0.16	0.16	0.12	0.12	0.12	0.12	0.12	0.11
Q_{misid}		UUUU	0.01	0.02	0.01	0.02	0.02	0.02	0.02	0.04
WW	mc	UUUU	0.05	0.06	0.06	0.08	0.07	0.12	0.09	0.08
	thry	CCCC	0.05	0.06	0.07	0.09	0.07	0.09	0.10	0.12
ZZ	mc	UUUU	0.02	0.03	0.04	0.03	0.03	0.04	0.04	0.03
	thry	CCCC	0.02	0.02	0.02	0.03	0.02	0.03	0.03	0.03
	miss	CCUU	0.01	0.01	0.01	0.01	0.01	0.01	0.01	0.01
Zee	mc	UUUU	0.09	0.10	0.10	0.11	0.07	0.13	0.14	0.15
	thry	CCCC	0.18	0.20	0.21	0.28	0.25	0.27	0.32	0.46
	miss	CCUU	0.08	0.08	0.08	0.08	0.08	0.08	0.08	0.08
Cosmics		CUUU	0.03	0.03	0.02	0.02	0.02	0.02	0.03	0.02
QED ISR		CCCC	0.01	0.01	0.01	0.01	0.01	0.01	0.01	0.01
Statistical and systematic errors on the non-radiative A_{FB} (in units of 10^{-2})										
Error		YECX	183	189	192	196	200	202	205	207
ΔA_{FB}stat		UUUU	6.43	3.92	9.76	6.12	5.63	9.02	6.09	4.79
ΔA_{FB}syst		—	0.14	0.13	0.10	0.10	0.11	0.11	0.11	0.12
eff	mc	CCUU	0.04	0.04	0.04	0.04	0.04	0.04	0.04	0.04
	4π	CCUU	0.10	0.11	0.07	0.08	0.08	0.08	0.07	0.08
Q_{misid}		UUUU	0.03	0.03	0.03	0.03	0.03	0.03	0.03	0.06
F_{mig}		UUUU	0.03	0.02	0.01	0.01	0.02	0.01	0.02	0.02
WW	mc	UUUU	0.00	0.01	0.02	0.01	0.01	0.04	0.01	0.02
WW	thry	CCCC	0.00	0.00	0.00	0.00	0.00	0.00	0.00	0.00
ZZ	mc	UUUU	0.02	0.02	0.02	0.02	0.02	0.02	0.03	0.02
ZZ	thry	CCCC	0.00	0.00	0.00	0.00	0.00	0.01	0.01	0.01
Zee	mc	UUUU	0.04	0.01	0.04	0.02	0.03	0.01	0.004	0.04
Zee	thry	CCCC	0.01	0.00	0.01	0.01	0.01	0.00	0.01	0.01
Cosmics		CUUU	0.05	0.04	0.03	0.02	0.02	0.03	0.04	0.03
QED ISR		CCCC	0.01	0.01	0.01	0.01	0.01	0.01	0.01	0.01

Table 5.13: The statistical and systematic errors with a breakdown of the different sources of the systematic error for the inclusive and non-radiative forward-backward asymmetry, together with their correlations between different years (Y), energies (E), final states (C) and experiments (X). (U) has no correlation, (C) is fully correlated.

Chapter 6

Interpretation of the Measurements

In this chapter the results obtained from the measurements described in the previous chapter are interpreted in several ways. First, a comparison of the results to the Standard Model predictions are made. Deviations may be hints for new physics phenomena. Second, the measurements for the non-radiative samples which are the most sensitives to physics beyond the Standard Model are used together with results from other $f\bar{f}$ final states to probe two from the variety of models which include new physics phenomena: the possible existence of an additional heavy gauge boson, the Z', and the virtual exchange of a spin-2 graviton in the framework of gravity in large extra dimensions.

6.1 Comparison with the Standard Model

The results for the cross section and forward-backward asymmetry measurements, given in Tables 5.7 and 5.9, were compared to the theoretical predictions of the Standard Model shown in Figure 6.2 and 6.3. The predictions for $\sigma_{\mu\mu}$ and $A_{FB}^{\mu\mu}$ were computed with the ZFITTER program [33] version 6.36. In addition to the direct comparison (curves) the ratio $\mathcal{R}$ of the cross section measurement to the predictions was calculated for each energy:

$$\mathcal{R} = \frac{\sigma_{\mu\mu}}{\sigma_{\mu\mu}(\mathrm{SM})}$$

For the asymmetry measurement it is more useful to study the difference to the prediction as this observable is limited between -1 and 1.

$$\mathcal{D} = A_{FB}^{\mu\mu} - A_{FB}^{\mu\mu}(\mathrm{SM})$$

Overall, $\sigma_{\mu\mu}$ and $A_{FB}^{\mu\mu}$ are in a good agreement to the Standard Model predictions. The deviations seen in the different measurements can be better illustrated in terms of the so-called *pulls*:

$$\mathrm{Pull} = \frac{\mathrm{Measurement} - \mathrm{Prediction}}{\Delta\mathrm{Measurement}}, \tag{6.1}$$

where the deviation from the prediction is compared to the total error, statistical and systematical, achieved for a certain measurement. Figure 6.4 shows the pulls for the 32 measurements performed in this analysis. The main discrepancies were found for the inclusive cross sections at 183, 196 and 200 GeV, where the pull amounts to 1.8σ[1] (high), 1.7σ (low) and 2.3σ (high), respectively. At the other energy points the deviations for this measurement are within or very close to 1σ. The deviations of the non-radiative cross sections mainly have the same sign as for the inclusive measurements, with the biggest discrepancy being at 200 GeV with 1.7σ (high). The asymmetry measurements, in most cases, are within 1σ deviation (high and low), with the biggest discrepancy seen at 207 GeV (1.5σ high) for the inclusive sample and at 205 GeV (1.3σ high) for the non-radiative sample.

The distribution of the pulls for all $\sigma_{\mu\mu}$ and $\mathrm{A}_{\mathrm{FB}}^{\mu\mu}$ measurements is shown in Figure 6.1, the absolute value of the pull for each measurement averaged over all energies is given in Table 6.1, together with the χ^2's and probabilities from the comparison of each measurement to the Standard Model predictions. The χ^2 was computed taking into account the full error matrix with all correlations using following formula:

$$\chi^2 = \sum_{i,j} (x_i - y_i)\, W_{ij}\, (x_j - y_j), \tag{6.2}$$

where $x_{i,j}$ are the measurements, $y_{i,j}$ their predictions and W_{ij} the weight matrix containing the inverse covariance. The errors include the theoretical uncertainties associated to the SM predictions which amount to 0.4% for $\sigma_{\mu\mu}$ and 0.004 for $\mathrm{A}_{\mathrm{FB}}^{\mu\mu}$ [7]. The lowest probability with 4.4% is found for the inclusive cross section, the non-radiative cross section yielded to 58.0%. For the forward-backward asymmetry probabilities of 87% and 97% were achieved.

Measurement	$\sigma_{\mu\mu}$		$\mathrm{A}_{\mathrm{FB}}^{\mu\mu}$	
183-207 GeV	incl.	nrad.	incl.	nrad.
$\langle$Abs(Pulls)$\rangle$	1.30	0.74	0.60	0.40
χ^2/NdoF	15.9/8	6.6/8	3.8/8	2.3/8
$P(\chi^2)$	4.4%	58.0%	87.0%	97.0%

Table 6.1: The Pull, averaged over the energies 183-207 GeV, the χ^2/NdoF and the probability for each measurement from the comparison to the Standard Model.

A good test of the compatibility of the measurements to the theoretical predictions is to perform the average of the ratio $\mathcal{R}$ and the difference $\mathcal{D}$ over all energies considered. The average was obtained with a χ^2 fit to the $\sigma_{\mu\mu}$ and $\mathrm{A}_{\mathrm{FB}}^{\mu\mu}$ measurements using the full error matrix, with $\mathcal{R}$ and $\mathcal{D}$ being a free parameter, respectively. The fit yielded to:

$$\begin{array}{lll} \boldsymbol{\sigma_{\mu\mu}}: & \boldsymbol{\langle\mathcal{R}\rangle_{incl} = 1.004 \pm 0.020} & \boldsymbol{\langle\mathcal{R}\rangle_{nrad} = 0.997 \pm 0.026} \\ \boldsymbol{\mathrm{A}_{\mathrm{FB}}^{\mu\mu}}: & \boldsymbol{\langle\mathcal{D}\rangle_{incl} = 0.008 \pm 0.017} & \boldsymbol{\langle\mathcal{D}\rangle_{nrad} = 0.010 \pm 0.021} \end{array}$$

The averages are compatible with $\mathcal{R} = 1$ and $\mathcal{D} = 0$. The uncertainty of the average is dominated by the statistical errors of the measurements.

The angular distributions of the non-radiative cross section, shown in Figures 5.15 and 5.16, are overall in a good agreement with the Standard Model. The biggest discrepancies were seen at 202 GeV and 205 GeV, yielding to a χ^2 probability of 0.4% and 14.5% compared to

[1] given in standard deviations

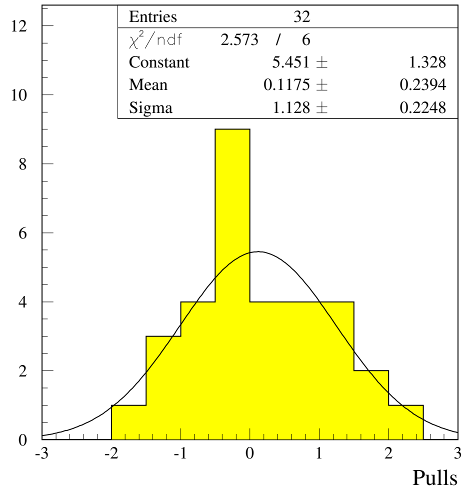

Figure 6.1: The pull distribution for all $\sigma_{\mu\mu}$ and $\mathrm{A}_{\mathrm{FB}}^{\mu\mu}$ measurements considered. It follows the expected Gaussian with unit variance, centered on 0.

the ZFITTER predictions, respectively. At 202 GeV this is specially caused by the excess of events in the first bin. At 205 GeV the shape of the distribution shows an excess of events in the two very forward bins and a lack of events in-between. The differences were investigated, but no systematic effects - like an excess of like-signs, cosmic muons or backgrounds from migrations from low $\sqrt{s'}$ to the non-radiative sample - were found. Thus, the discrepancies are considered a statistical fluctuation. An overall χ^2 of 103.3/80 (4.1% probability) for all energies was computed using the expected statistical errors and the full error matrix. Figure 6.5 shows the bin-by-bin average of the differential cross sections and the averaged ratios.

Overall, the results of the $\sigma_{\mu\mu}$, $\mathrm{A}_{\mathrm{FB}}^{\mu\mu}$ and $\frac{d\sigma_{\mu\mu}}{d\cos\theta}$ measurements for the $\mu^+\mu^-$ final state are in a good agreement to the predictions of the Standard Model, computed with the ZFITTER program. Discrepancies seen were investigated and found to have statistical nature. The relatively large fluctuations in the inclusive cross sections led to a low χ^2 probability. Nevertheless, the ratio $\mathcal{R}$, that compensates for the fluctuations, is compatible to the value of 1, expected from the SM.

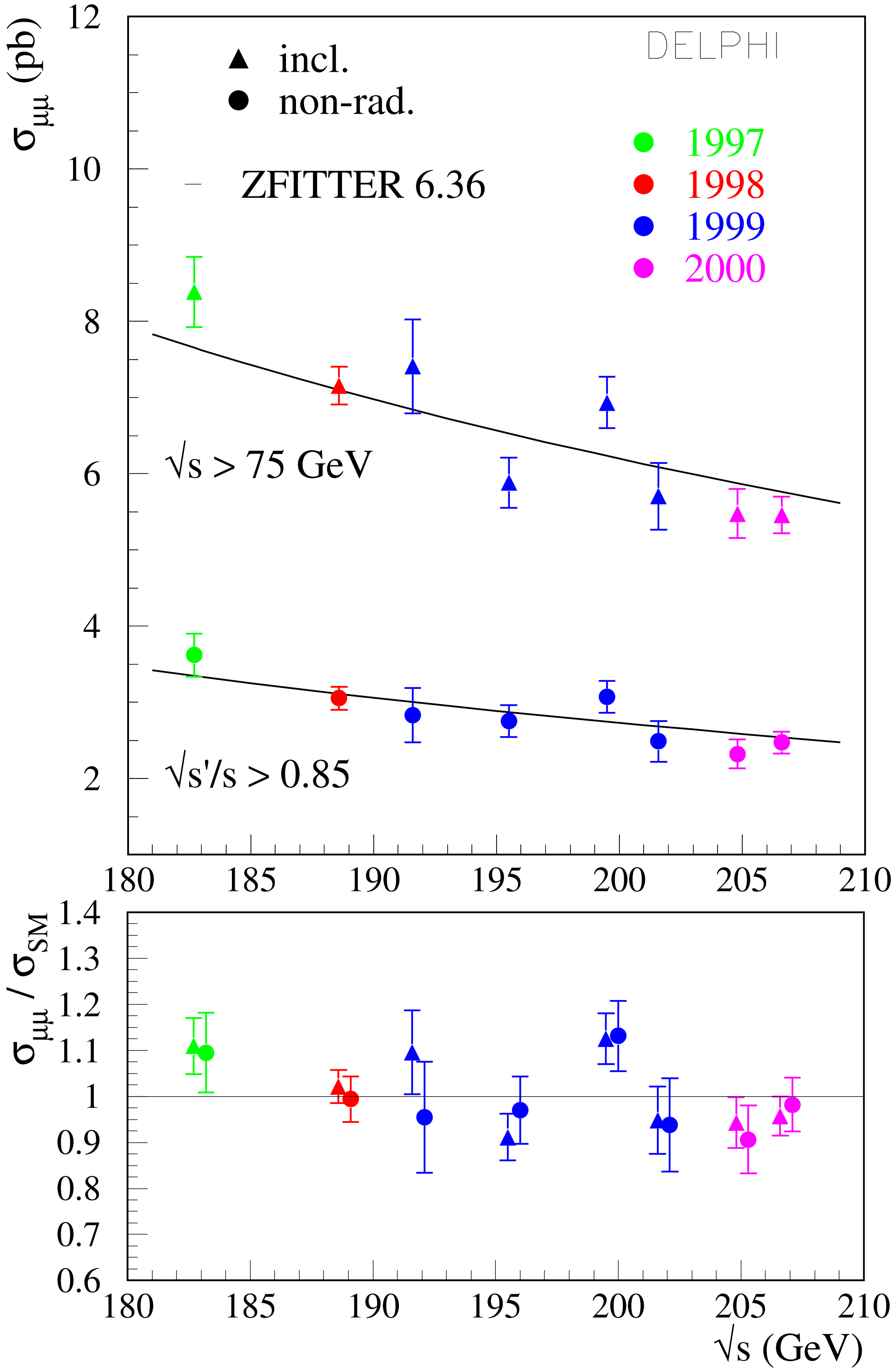

Figure 6.2: Comparison of the cross sections to the Standard Model predictions from ZFITTER for the inclusive and the non-radiative measurement of the $\mu^+\mu^-$ final states as curves (top) and as the ratio to the SM (bottom).

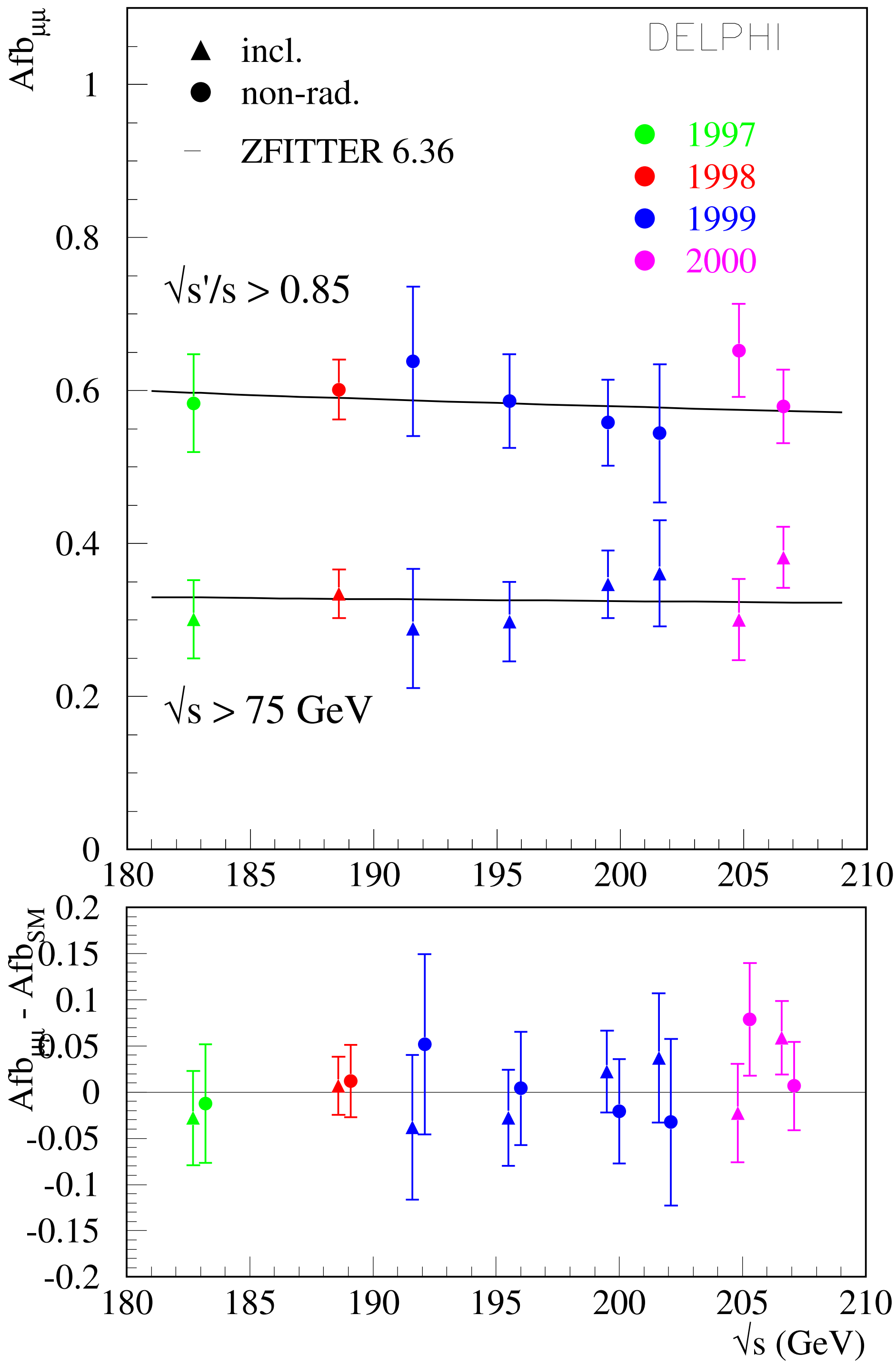

Figure 6.3: Comparison of the forward-backward asymmetries to the Standard Model predictions from ZFITTER for the inclusive and the non-radiative measurement of the $\mu^+\mu^-$ final states as curves (top) and as the difference to the SM (bottom).

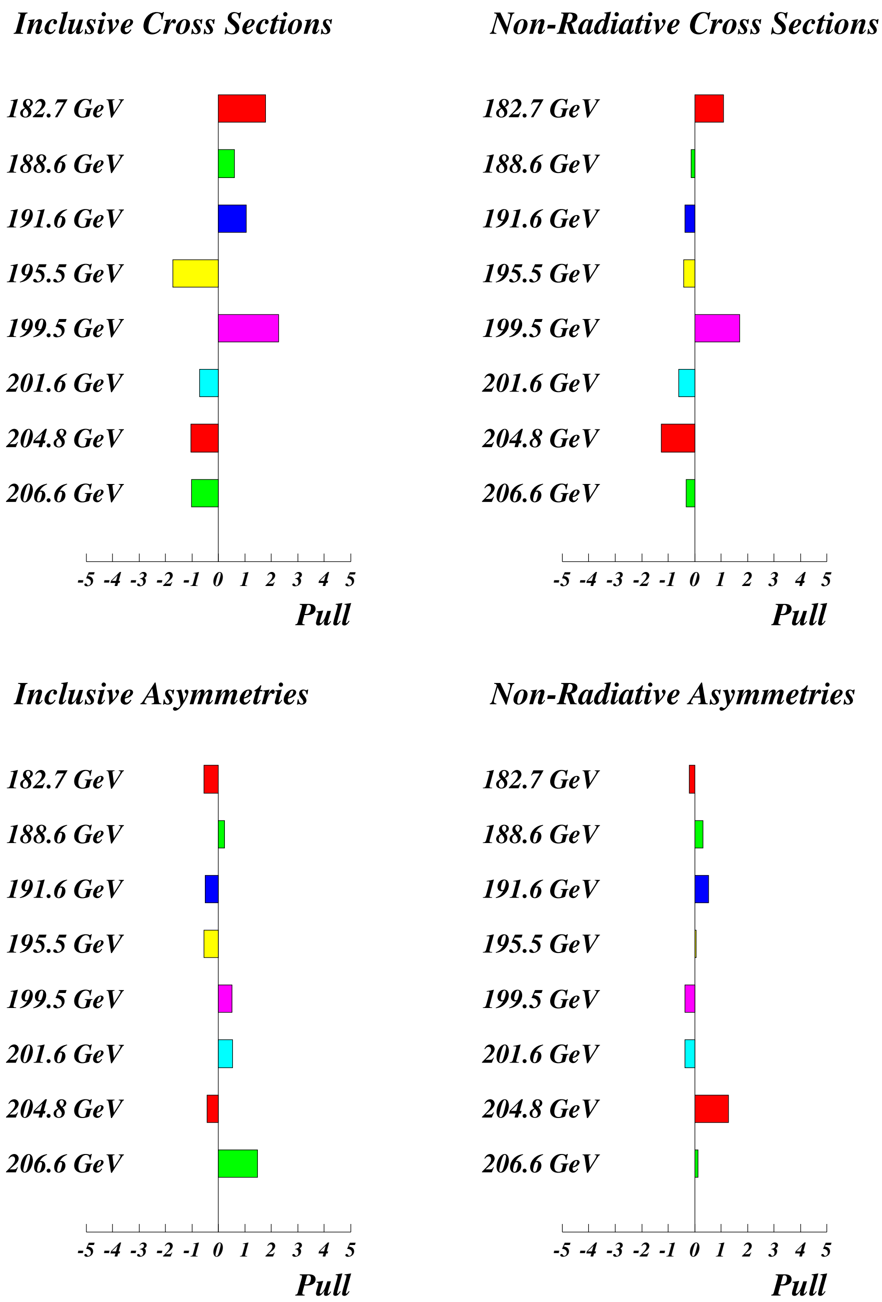

Figure 6.4: Pull plots for the inclusive and non-radiative measurements of $\sigma_{\mu\mu}$ and $A_{FB}^{\mu\mu}$ for all energies considered. The error on the data was taken from the statistical and systematic contributions, the SM prediction was taken from ZFITTER.

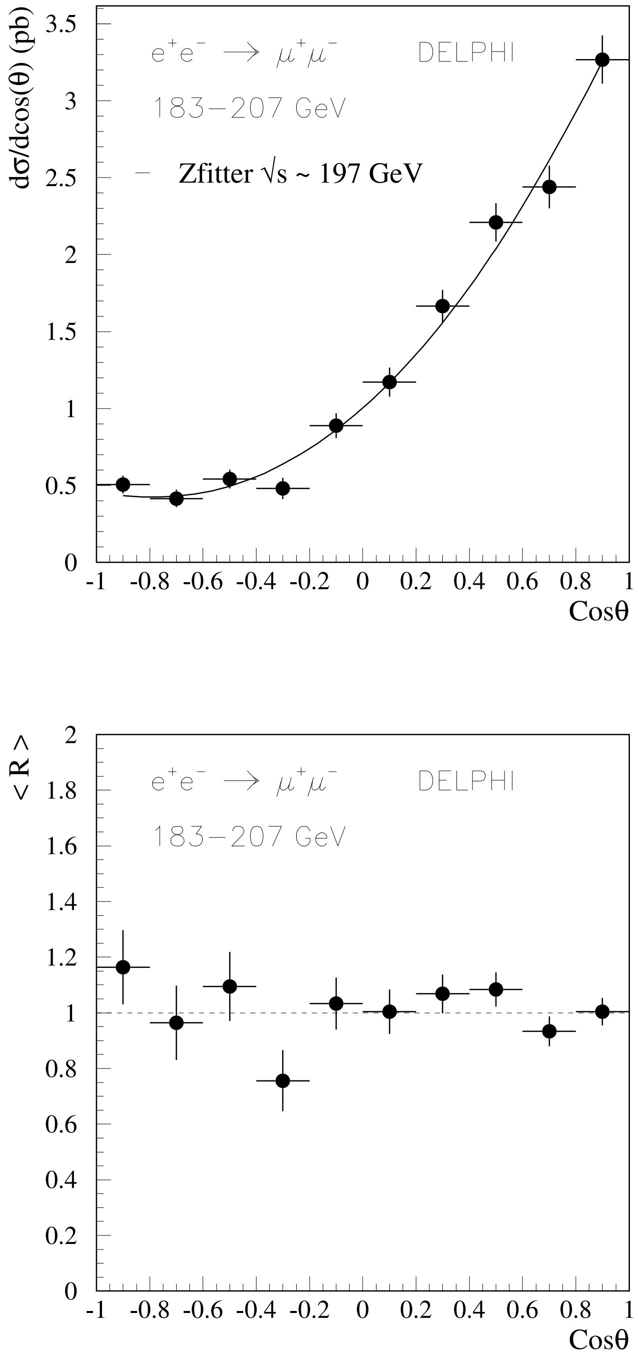

Figure 6.5: Differential cross sections for non-radiative events as bin-by-bin averages of the ratio, $\langle \mathcal{R} \rangle$, (lower plot), and as average $d\sigma/d\cos\theta$ measurements obtained by multiplying $\langle \mathcal{R} \rangle$ by the predictions at the luminosity weighted center-of-mass energy (upper plot).

6.2 Search for a Z′ Boson

A possible Z′ exchange in the fermion pair production would modify the observed cross sections and asymmetries with respect to the predictions from the Standard Model, e.g. for the cross section one would expect additional contributions originating from the Z′:

$$\sigma = \sigma_\gamma + \sigma_{\gamma \mathrm{Z}} + \sigma_{\mathrm{Z}} + \sigma_{\gamma \mathrm{Z}'} + \sigma_{\mathrm{ZZ}'} + \sigma_{\mathrm{Z}'}.$$

The first, second and third term are the known SM processes with γ/Z propagator, term three and four represent the interference of the Z′ to the SM and the last part is the pure Z′ exchange. At LEP I the measured cross sections and asymmetries at energies around the Z Peak allowed a very precise determination of the Z boson parameters. If this particle is not the Standard Model Z^0, but a mixture with the Z_0' boson, the line-shape would change. Therefore, the LEP I data are very sensitive to the the mixing angle, $\theta_{\mathrm{ZZ}'}$. At energies well above the Z resonance, the interference between the Z and the Z′ becomes increasingly important and thus, the obtained data are sensitive to the mass of the Z′.

The predictions including a Z′ boson are computed with the program ZEFIT [48], [49], an extension to the ZFITTER package. It contains routines that originate from ZFITTER and that are modified for the Z′ properties. ZEFIT can be used to either perform a model independent fit to the data and derive limits on the effective couplings of Z′ to the fermions or, to compare the cross sections and forward-backward asymmetries directly to the predictions in presence of a Z′ boson. Input parameters to the routines are the masses of Z and Z′, the mixing angle between them, $\theta_{\mathrm{ZZ}'}$, and the model angle, θ_{E6} or α_{LR} and, in case of the model independent fit, the vector and axial vector couplings of the Z′. In addition the usual ZFITTER input parameters are used, the masses of the top quark, $\mathrm{m_{top}}$, and the Higgs boson, $\mathrm{M_H}$, and the strong coupling constant, α_s and the hadronic vacuum polarization, $\Delta\alpha_{had}^{(5)}$[2]. In order to reduce the number of free parameters the following values were chosen [50]:

$$\begin{aligned} \mathrm{m_{top}} &= 175 \pm 5\ \mathrm{GeV}/c^2 \\ \mathrm{M_H} &= 150^{+850}_{-36}\ \mathrm{GeV}/c^2 \\ \alpha_s &= 0.118\ \pm 0.002 \\ \Delta\alpha_{had}^{(5)} &= 0.02761 \pm 0.00036. \end{aligned}$$

Those were fixed to their default values. The changes in the fits varying them within the error given were found to be negligible.

6.2.1 Model dependent Fits

The different E_6 models, the L-R model and the SSM, described in section 2.2.1, were investigated. The expected deviations from the Standard Model prediction for the $\mathrm{q\bar{q}}$ and $\mathrm{e^+e^-} \to \mu^+\mu^-$ process for different Z′ models are shown in figure 6.6. It can clearly be seen that the width of the Z changes in both processes due to a non-zero mixing angle ($\theta_{\mathrm{ZZ}'} = 10\,\mathrm{mrad}$, $\mathrm{M_{Z'}} = 750\ \mathrm{GeV/c^2}$). At LEP II energies the flavor independent hadronic cross sections would shift to higher values for the $\mathrm{E}_6\chi$ and $\mathrm{E}_6\eta$ models, whereas for the sequential Standard Model the ratio would drop significantly. The muon cross section at

[2] which should be used in new ZFITTER versions instead of α_{em}

LEP II changes in a different manner, in all models a decrease at energies above 150 GeV is expected ($M_{Z'}$ = 300 GeV/c^2 and $\theta_{ZZ'} = 0$ mrad assumed). For the muon asymmetries the largest deviations are found below the Z peak and above 150 GeV/c^2. In order to illustrate the sensitivity to a Z′ boson some data points are given as well, obtained from analyses at LEP I and at lower energies from LEP II together with the results presented in Chapter 5. More Figures from the models considered assuming different values for $M_{Z'}$ and $\theta_{ZZ'}$ are given in the Appendix C.

In order to derive limits on the Z′ parameters, leptonic and hadronic cross sections and the leptonic asymmetries measured at LEP I and LEP II energies were used:

LEP I: $\sigma\ (e^+e^- \to e^+e^-, \mu^+\mu^-, \tau^+\tau^-, q\bar{q}) \quad + \quad A_{FB}\ (e^+e^- \to e^+e^-, \mu^+\mu^-, \tau^+\tau^-)$

LEP II: $\sigma\ (e^+e^- \to \mu^+\mu^-, \tau^+\tau^-, q\bar{q}) \quad + \quad A_{FB}\ (e^+e^- \to \mu^+\mu^-, \tau^+\tau^-)$

Data not presented here were taken from [51], [54] and [53]. In order to improve the sensitivity of this analysis, only the non-radiative measurements with a cut of $\sqrt{s'}/\sqrt{s} > 0.85$ were used at LEP II energies. Here, the e^+e^- final states are not considered, due to the complication with the t-channel effects. To take into account for different signal definition of $\sqrt{s'}$ for the leptonic and hadronic final states, the ZFITTER flags had to be set accordingly[3]. In $q\bar{q}$ final states, due to the difficulty to clearly separate final state radiation from initial state radiation, the ISR-FSR was subtracted and thus, $\sqrt{s'}$ was taken to be the invariant mass of the s-channel propagator. The E_6 model angles were chosen to be $\theta_{E6} = 0,\ \pi/2,\ -\arctan\sqrt{5/3}$ for the χ, ψ and η model, respectively. In case of the L-R model α_{LR} was set to 1.1, the SSM is assumed to have the same couplings as the standard Z boson.

Using formula (6.2), the χ^2 was calculated between the measurements and the predictions from the different models taking into account the correlations of the experimental errors. In addition, the uncertainties arising from the SM predictions were included when computing the error matrix. Those were 0.26% for σ_{qq}, 0.4% for $\sigma_{\mu\mu}$ and $\sigma_{\tau\tau}$, and 0.004 for A_{FB}^{ll} [7]. Correlations between LEP I and LEP II are very small and therefore neglected. The minimization of the χ^2 was done with the MINUIT program [56]. Results from fits using LEP I data alone with the Z mass left as a free parameter showed that it was compatible with the LEP combined value of 91.1875 ± 0.0021GeV/c^2 [57] within the experimental error, thus, M_Z has been fixed to this value. The limits on the two remaining parameters, $M_{Z'}$ and $\theta_{ZZ'}$, were derived from a 2-dimensional scan that was made in the possible range of $M_{Z'}$ and $\theta_{ZZ'}$ calculating the χ^2 for different values in the plane. The two-dimensional exclusion contour at 95% confidence level limit (CL) was then obtained with $\chi^2 < \chi^2_{min} + 5.99$. For each single parameter the 95% CL was derived from $\chi^2 < \chi^2_{min} + 3.84$ in that plane.

The one-dimensional limits for the different models are found in Table 6.2, the two-dimensional exclusion curves for the E_6 and the L-R model are shown in Figure 6.7. The limits for the Z′ mass range from 360 to 530 GeV/c^2 depending on the model. For the SSM a limit of 1300 GeV/c^2 was found. A fit using LEP II data alone with $\theta_{ZZ'}$ fixed to zero, yielded to very similar limits as these data strongly constraint the mass $M_{Z'}$. The limits improved significantly from previous analyses where only the LEP I data and lower LEP II energies were used [36],[54],[55]. The limits on $\theta_{ZZ'}$ range from 2.6 to 9.6 mrad and have not improved significantly as its bounds were already constraint by the LEP I data.

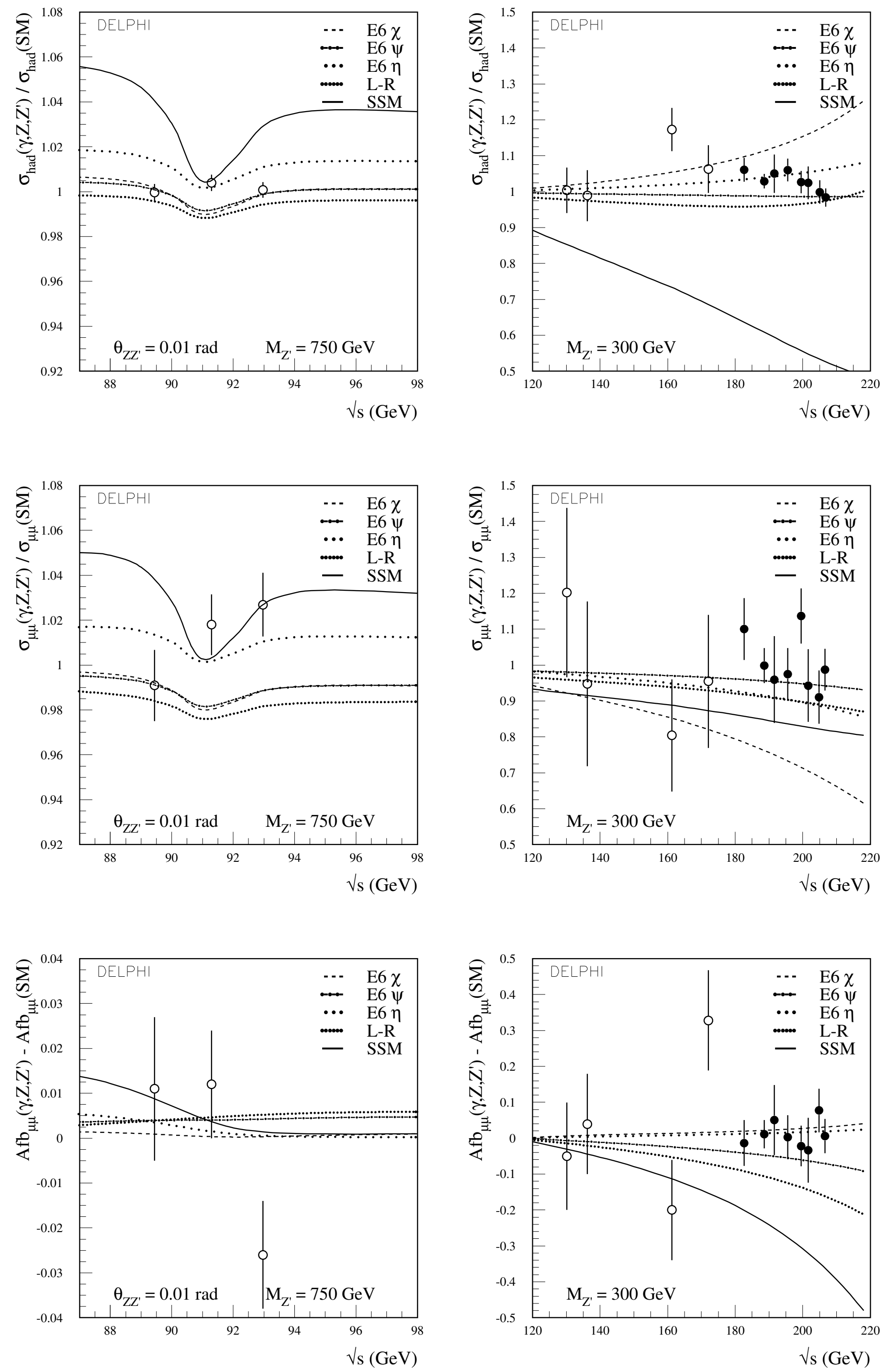

Figure 6.6: Comparison of the different Z′models and the Standard Model for the quark-pair production (top) and muon-pair production (middle and bottom) as a function of the center-of-mass energy, $\sqrt{s}$. The upper plots show the ratio $\mathcal{R}$ of the cross section and the lower plots the difference $\mathcal{D}$ of the forward-backward asymmetry to the SM. For LEP II energies $\theta_{ZZ'}$ was set to zero. The closed points are the results presented in [51] ($q\bar{q}$) and in this thesis ($\mu^+\mu^-$), the open points present previous results at lower energies from 1995-1996 ($\sqrt{s}$= 89.4, 91.2, 93.0, 130.2, 136.2, 161.3, 172.1 GeV) [53], [54].

Model	χ	ψ	η	L-R	SSM
$M_{Z'}^{low}$ (GeV/c^2)	530	485	360	455	1300
$\mid \theta_{ZZ'}^{up} \mid$ (mrad)	3.2	2.6	9.6	2.8	2.9

Table 6.2: 95% confidence level lower limits on the Z′ mass and upper limits on the ZZ′ mixing angle within the χ, ψ, η and L-R models.

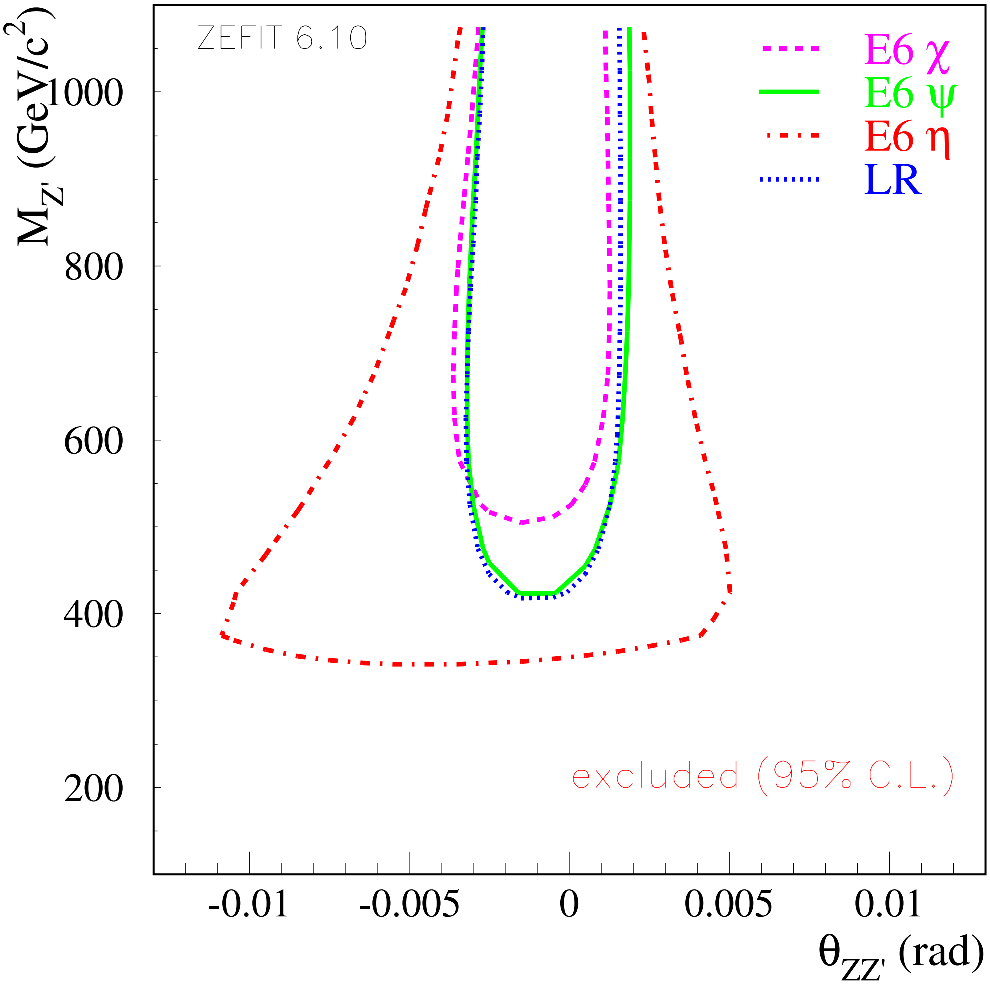

Figure 6.7: 95% CL exclusion curves in the $M_{Z'} - \theta_{ZZ'}$ plane for the χ, ψ, η and L-R models. The Standard Model parameters are fixed to their default values. The influence due to a free Z mass is negligible.

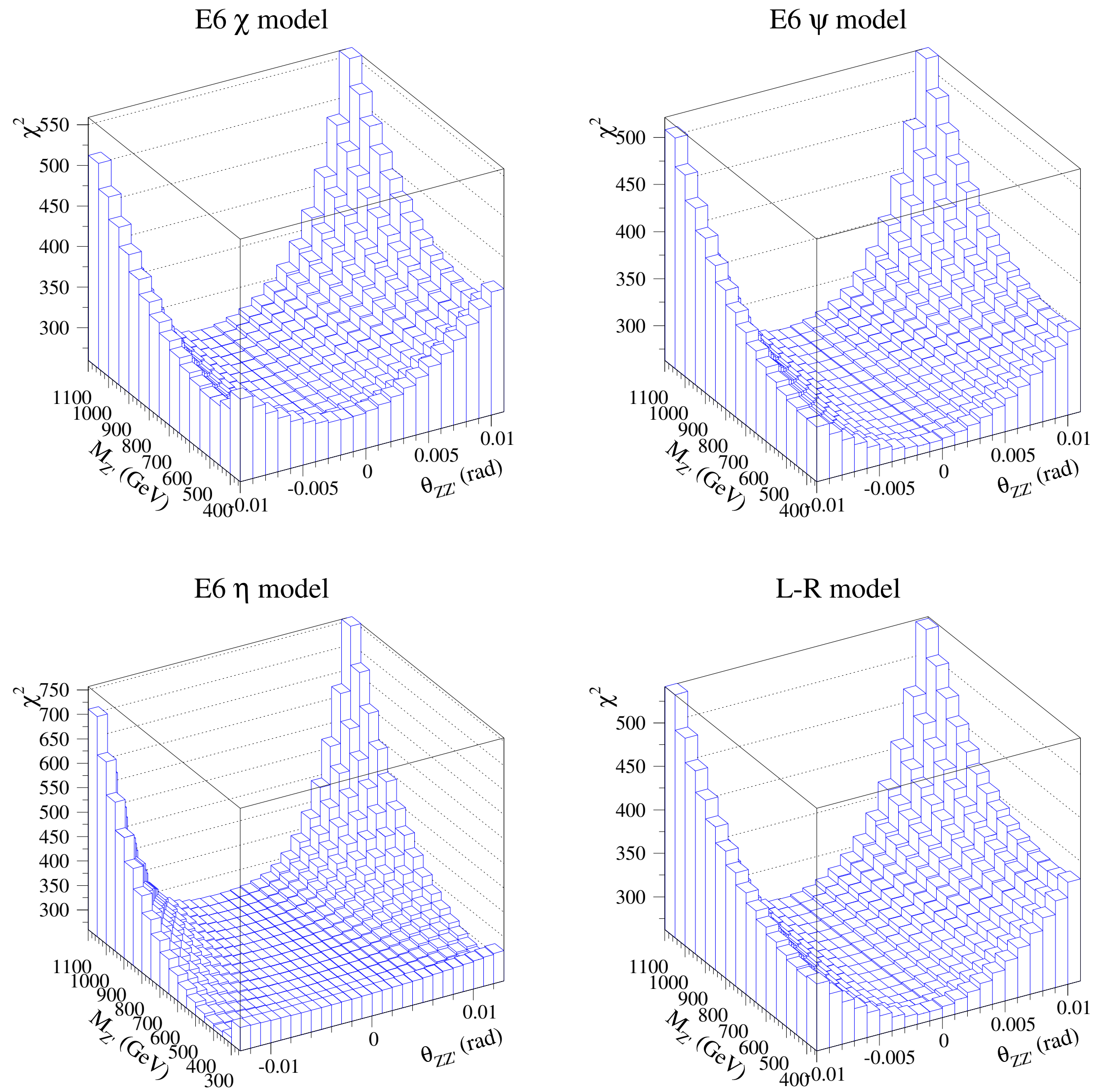

Figure 6.8: χ^2 surface in the $M_{Z'}$ - $\theta_{ZZ'}$ plane for the different models (E_6 and L-R).

A χ^2/ndof between 259.6/235 and 262.9/235 for the different models was achieved, referring to a χ^2 probability between (10.2 - 12.9)%. This is compatible with the χ^2 probability for the Standard Model that was found to be 11.9% (262.9/237). The obtained χ^2 surface for the E_6 models and the L-R model are shown in Figure 6.8. No clear minimum inconsistent with the Standard Model for any of the models that could be an evidence of the existence of a Z' boson was found.

[3]FINR=1, INTF=1 (leptons); FINR=0, INTF=0 (hadrons)

Limits from averaged measurements

The results for the $e^+e^- \to f\bar{f}$ process at LEP II obtained with the DELPHI detector have been averaged with the results achieved by the other LEP experiments, ALEPH, OPAL and L3, by the electroweak working group [58] (still preliminary). In order to improve the sensitivity on the Z′ mass, the same measurements, leptonic asymmetries and leptonic and hadronic cross sections (without electrons), were used as combined numbers to derive limits from the different models. The different experiments have not necessarily the same signal definition, therefore, the results had been corrected to a common definition which is $\sqrt{s'}$ being defined as the s-channel propagator. The ZFITTER flags had to be changed accordingly[4]. The full error matrix has been used when computing the χ^2, e.g. the systematic uncertainties fully correlated between energies, final states and experiments [59].

In order to improve the limits on $\theta_{ZZ'}$ as well, it would be very useful to have the same set of combined results from the LEP I period too. However, it is extremely complicated to average hundreds of measurements from the experiments using different phase space definitions and experimental errors and take into account all correlations between them. Therefore, instead of using the *"real observables"* like cross sections and asymmetries, the combination of the experimental results was done on the basis of the four sets of so-called *"pseudo observables"* (PO) [60]. Those were obtained by each experiment with a model independent fit to the measured observables extracting the properties of the Z boson such as its mass, total and partial decay widths, and coupling constants to the fermions. To reduce correlations among the fit parameters a set of nine parameters was chosen to describe the total hadronic and leptonic cross sections as well as the leptonic asymmetries around the Z peak. These are:

$$\mathrm{M_Z},\ \Gamma_\mathrm{Z},\ \sigma_h^0,\ R_{l(e,\mu,\tau)},\ A_{FB}^{0,l(e,\mu,\tau)}$$

Assuming lepton universality the set is reduced to five parameters. The combined PO can be either used to compare them directly to the predictions from ZEFIT or, to be transformed to realistic observables computing the hadronic and leptonic cross section and the leptonic asymmetry at the peak. In case of transformation of the PO the hadronic cross section was computed 2 GeV below and above the Z resonance, additionally. Fitting both, the PO themselves or the transformed σ_{ff} and $\mathrm{A_{FB}^{ll}}$, as well as the use of five or nine pseudo observables, yielded to results that were consistent with each other. In this analysis five PO transformed to the realistic observables were used.

In the strict sense, using the averaged PO is not correct as except for the ZZ′ mixing the effect of a Z′ mass to the line shape is neglected using the SM branch in ZEFIT. Nevertheless, for high Z′ masses and small $\theta_{ZZ'}$ this can be taken as a good approximation. A comparison fitting the pseudo observables obtained from DELPHI [53] alone showed a perfect agreement with fits using the measured cross sections and asymmetries themselves.

The results obtained from the fits to the combined LEP II measurements and averaged pseudo observables from LEP I are shown in Table 6.3 as one-dimensional 95% CL limits on $\mathrm{M_{Z'}}$ and $\theta_{ZZ'}$, and in Figure 6.9 as 95% two-dimensional exclusion limits in the $\mathrm{M_{Z'}}$ - $\theta_{ZZ'}$ plane. No evidence for the existence of an additional Z′ boson was found. The limits range from 435 to 665 GeV/c^2 dependent on the model, a Z′ predicted in the SMM must be $>$ 2170 GeV/c^2. The limits improve with respect to limits obtained by the DELPHI results alone and they are consistent with results obtained by the electroweak working group [58].

Model	χ	ψ	η	L-R	SSM
$M_{Z'}^{low}$ (GeV/c^2)	665	545	435	465	2170
$\mid \theta_{ZZ'}^{up} \mid$ (mrad)	2.0	1.3	8.2	1.7	3.0

Table 6.3: 95% confidence level lower limits on the Z′ mass and upper limits on the ZZ′ mixing angle within the χ, ψ, η and L-R models using LEP combined results.

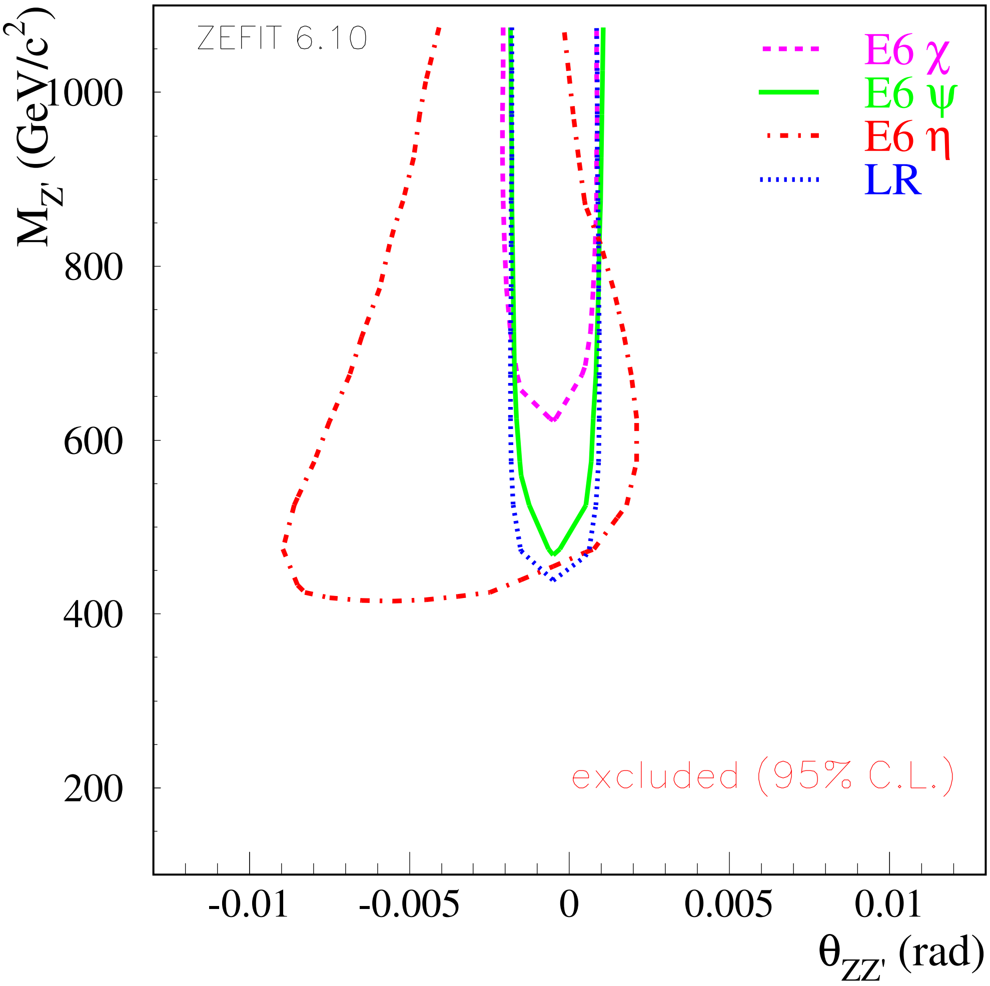

Figure 6.9: 95% CL exclusion curves in the $M_{Z'} - \theta_{ZZ'}$ plane for the χ, ψ, η and L-R models using LEP combined results. The Standard Model parameters are fixed to their default values. The influence due to a free Z mass is negligible.

Other experiments that perform a direct search for a Z′ are more sensitive like at the $p\bar{p}$ collider Tevatron. Analyses that used between 90 and 125 pb^{-1} of electron-pair and muon-pair production from the Drell-Yan process, obtained at CDF and DØ, excluded a Z′ with a mass between 610 to 740 GeV/c^2 depending on the model considered [61].

6.2.2 Model independent Fits

In addition to the test of specific Z′ model one can derive limits on the couplings of the Z′ to the fermions by a model independent fit. A new interaction of a Z′ boson would lead to an additional amplitude of fermion-pair production [62]:

$$\begin{aligned} \mathcal{M}(\mathrm{Z}') &= \frac{g_2^2}{s - m_{\mathrm{Z}'}^2} \bar{u}_e \gamma_\beta (\gamma_5 a'_e + v'_e) u_e \bar{u}_f \gamma^\beta (\gamma_5 a'_f + v'_f) u_f \\ &= -\frac{4\pi}{s} \bar{u}_e \gamma_\beta (\gamma_5 a_e^N + v_e^N) u_e \bar{u}_f \gamma^\beta (\gamma_5 a_f^N + v_f^N) u_f, \end{aligned}$$

with ($m_{\mathrm{Z}'}^2 \gg s$)

$$a_f^N = a'_f \sqrt{\frac{g_2^2}{4\pi} \frac{s}{m_{\mathrm{Z}'}^2 - s}}, \quad v_f^N = v'_f \sqrt{\frac{g_2^2}{4\pi} \frac{s}{m_{\mathrm{Z}'}^2 - s}}$$

$$\text{and} \qquad m_{\mathrm{Z}'}^2 = \mathrm{M_{Z'}}^2 - i \Gamma_{\mathrm{Z}'} \mathrm{M_{Z'}}.$$

Far away from the Z′ resonance fermion production is only sensitive to the normalised couplings, a_f^N and v_f^N. Therefore, the Z′ couplings cannot be measured independently of the Z′ mass. Generally, the couplings have to be evaluated for each fermion-pair separately. In order to reduce the number of free parameters only the lepton-pair production was considered, assuming lepton universality. In a model independent ansatz g_2 is not clearly defined, thus, $\frac{g_2^2}{4\pi} = 1$ is set conventionally. The normalised couplings are then defined in the following way:

$$a_l^N = a'_l \sqrt{\frac{s}{m_{\mathrm{Z}'}^2 - s}}, \quad v_l^N = v'_l \sqrt{\frac{s}{m_{\mathrm{Z}'}^2 - s}} \tag{6.3}$$

The program ZEFIT calculates cross sections and asymmetries dependent on the Z′ mass and the couplings to the fermions. Thus, a comparison between the predictions and the measured observables allows the determination of a'_l and v'_l. A fit was performed to the leptonic cross sections and asymmetries measured at LEP I and LEP II energies with the DELPHI detector. σ_{ll} constraints both couplings while A_{FB}^{ll} confines mainly the axial vector couplings. Figure 6.10 (left) shows the obtained exclusion contours for the couplings to leptons at 95% CL, using $\chi^2 < \chi^2_{min} + 5.99$, assuming different Z′ masses (i.e. $\mathrm{M_{Z'}}$ = 300, 500 and 1000 GeV/c^2). The limits on the normalised couplings were then derived from formula (6.3), using $\chi^2 < \chi^2_{min} + 3.84$ for a'_l and v'_l, and yields to:

$$|\mathbf{a_l^N}| < \mathbf{0.19} \qquad \text{and} \qquad |\mathbf{v_l^N}| < \mathbf{0.19} \qquad \text{for } \mathrm{M_{Z'}} \geq 300 \text{ GeV}.$$

The limits improve with respect to previous results where only LEP II data at low center-of-mass energies with low statistics together with LEP I data were used [36]. A decrease

[4] FINR=0, INTF=0

of 0.01 for a_l^N and 0.25 for v_l^N was found, approaching closely to the same value for both couplings. The limit on a_l^N is reduced to 0.11 when the lowest $M_{Z'}$ of 300 GeV/c^2 is excluded as indicated in the direct searches.

In addition to the DELPHI results, the combined leptonic cross sections and forward-backward asymmetries ($\mu^+\mu^-$, $\tau^+\tau^-$) from all LEP experiments at LEP II energies were used to derive limits as well. The obtained bounds on the normalised coupling using the full correlation matrix in the fits were reduced to:

$$|\mathbf{a_l^N}| < \mathbf{0.14} \qquad \text{and} \qquad |\mathbf{v_l^N}| < \mathbf{0.13},$$

where masses of Z′ between 500 and 1500 GeV/c^2 were considered. With a mass of 300 GeV/c^2 the limits would remain unchanged with respect to the DELPHI results. The 95% CL exclusion curves are shown in Figure 6.10 (right).

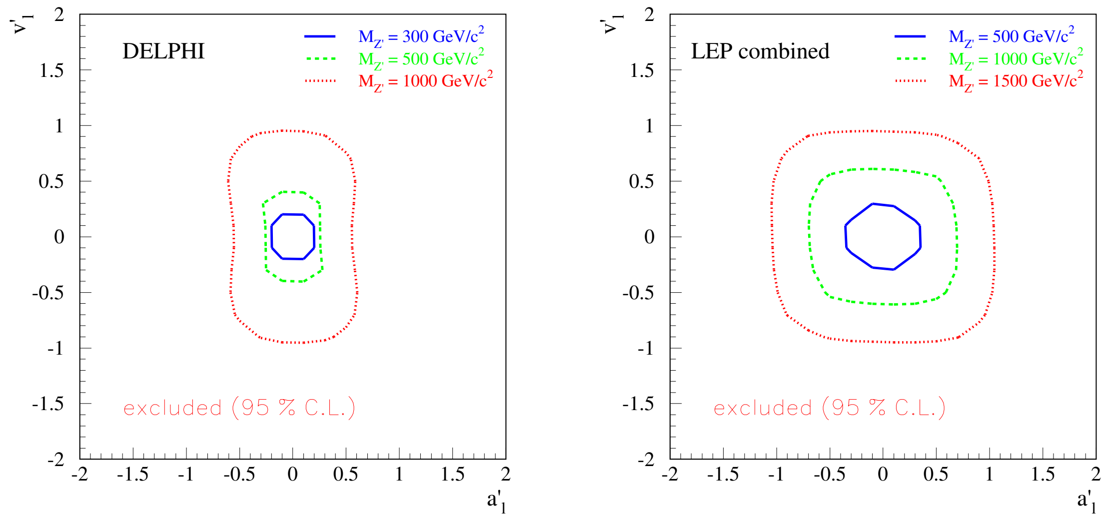

Figure 6.10: 95% exclusion curves in the $a_l' - v_l'$ plane, the couplings of the Z′ to the leptons, for the model independent approach assuming different masses of Z′, using DELPHI LEP I+II data (left) and LEP II combined numbers (right). The ZZ′ mixing was neglected.

6.3 Search for Quantum Gravity in large extra Dimensions

Gravitons may contribute to the two-fermion process via $e^+e^- \to G^* \to f\bar{f}$. The ratio of a single graviton state, in comparison to the Standard Model contribution, might be very small, but the many possible excitations modes in the extra dimensions may have an measurable effect. In this analysis the s-channel exchange of a Kaluza Klein (KK) tower of massive spin-2 gravitons is probed. It had been shown (see [21]) that spin-2 graviton exchange can easily be separated from that of new vector bosons. As described in chapter 2.2.2 the angular distribution for $e^+e^- \to f\bar{f}$ with massive fermions can be calculated in notation of Hewett (see Equation (2.46)):

$$\frac{d\sigma}{dz} = A(z) + B(z)(\frac{\lambda}{\mathrm{M_s^4}}) + C(z)(\frac{\lambda}{\mathrm{M_s^4}})^2, \tag{6.4}$$

where $z = \cos\theta$, the cosine of the scattering angle of the fermion. $\mathrm{M_s}$ denotes the string scale and

$$\epsilon = \frac{\lambda}{\mathrm{M_s^4}}$$

is defined as the free parameter. The coefficient λ is of $\mathcal{O}(1)$ and cannot be explicitly calculated without knowledge of the full quantum gravity theory. Its energy dependence can be neglected on the level of precision for the limits obtained here. The sign of λ, in principle, is undefined and both choices are considered when deriving limits. The first term in equation (6.4) is the bare SM cross section part, the second emerges from the interference between the graviton and the Z^0/γ propagators, the last part represents the pure graviton exchange.

The total cross section is not modified by the graviton exchange as integrating over $\cos\theta$ in Equation (6.4) the dominant $Z^0/\gamma - G$ interference part ($\sim \lambda/\mathrm{M_s^4}$) vanishes, leaving only the pure graviton part ($\sim \lambda^2/\mathrm{M}_s^8$), which gives only a negligible contribution to the cross section expected from the SM + gravity. Thus, only the angular distributions are sensitive to a graviton exchange. The shape of the angular distribution for spin-2 exchange is unique and provides a good signature for such new scenarios.

6.3.1 Sensitivity

The sensitivity to a graviton exchange of the data was investigated using following formula:

$$\Sigma = \frac{(d\sigma_{grav} - d\sigma_{SM})/d\sigma_{SM}}{\sqrt{\frac{d\sigma_{SM}}{\mathcal{L}}}/d\sigma_{SM}}, \tag{6.5}$$

where $d\sigma_{grav}$ and $d\sigma_{SM}$ denote the differential cross sections with and without graviton exchange, respectively. The numerator is the fractional difference of the expectations from virtual effects including a graviton to the SM prediction. The de-numerator is the fractional error of the SM expectation where $\Delta(d\sigma_{SM}) = \sqrt{\frac{d\sigma_{SM}}{\mathcal{L}}}$ scales with the integrated luminosity $\mathcal{L}$ considered. The sensitivity, thus, can be identified as a *pull* that is given in numbers of the standard deviations. An example is given in Figure 6.11 where the sensitivity to a possible graviton exchange in the process $e^+e^- \to \mu^+\mu^-$ as a function of $\cos\theta$ at 189 GeV with a corresponding integrated luminosity of 156 $(\mathrm{pb})^{-1}$ is shown. A string scale of $\mathrm{M_s}$=750 GeV

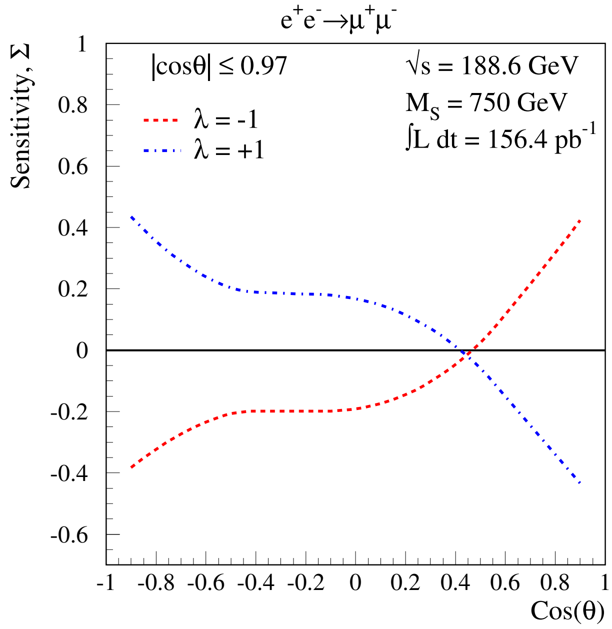

Figure 6.11: The sensitivity to a virtual graviton as a function of $\cos\theta$ to the process $e^+e^- \to \mu^+\mu^-$ for both choices of $\lambda = \pm 1$. An integrated luminosity of 156 $(\text{pb})^{-1}$ at $\sqrt{s} \simeq$ 189 GeV and a string scale of 750 GeV were assumed.

for both choices of $\lambda = \pm 1$ was assumed. It can clearly be seen that the region at large $|\cos\theta|$, the very forward/backward region, is most sensitive and the deviations from the SM here are the largest.

6.3.2 QED Corrections

The predictions for the $d\sigma/d\cos\theta$ including graviton exchange at Born level have been shown in Section 2.2.2. Radiative corrections have been taken into account using the *improved Born approximation* (MIBA) package [63] which calculates them to $\mathcal{O}(\alpha)$ semi-analytically. The differential cross section is given as:

$$\frac{d\sigma_{grav}(s)}{d\cos\theta} = \int_{0.85}^{1} d\nu \frac{d\sigma_{grav}^{IBA}(s')}{d\cos\theta} R(\nu), \tag{6.6}$$

where $\nu = \sqrt{s'}/\sqrt{s}$, $R(\nu)$ is the radiator function and $\frac{d\sigma_{grav}^{IBA}(s')}{d\cos\theta}$ is the differential cross section with both SM and graviton contributions, in the improved Born approximations. ISR corrections only had to be applied down to the $\sqrt{s'}/\sqrt{s}$ cut used for the non-radiative measurements. In order to provide a good agreement with the so obtained differential cross sections and the predictions from the latest ZFITTER version (6.36), the SM cross sections were computed with both programs for comparison. Differences were found originating from the more advanced radiator function in ZFITTER including ISR/FSR interference that affected mainly large $|\cos\theta|$, the sensitive region to a graviton exchange. Thus, scaling factors were computed taking into into account the difference in the QED corrections as follows:

$$X_{SCL} = \left(\frac{(\frac{d\sigma}{d\cos\theta})^{QED}_{ZFIT}}{(\frac{d\sigma}{d\cos\theta})^{BORN}_{ZFIT}} \right) \Bigg/ \left(\frac{(\frac{d\sigma}{d\cos\theta})^{QED}_{MIBA}}{(\frac{d\sigma}{d\cos\theta})^{BORN}_{MIBA}} \right) . \tag{6.7}$$

This was necessary for each bin in $\cos\theta$, for each energy point and final state considered. The correction was then applied when computing the predictions with MIBA.

6.3.3 Limits on the string scale, $\mathrm{M_s}$

The non-radiative measurements of the differential cross section for the $\mathrm{e^+e^-} \to \mu^+\mu^-$ process presented in Chapter 5 were used to probe the effects coming from a possible graviton exchange. In order to improve the limits, the results for the $\tau^+\tau^-$ final states obtained at LEP II energies (183-207 GeV) with $|\cos\theta| < 0.96$ were taken into account. Those can be found in [51]. The selection criteria and the referring calculations for $d\sigma/d\cos\theta$ of tau-pair production are described in detail in [64] and are not discussed here. The χ^2 was calculated between the measurements and the predictions resulting from different values for the free parameter ϵ $(-50.0 \leq \epsilon \leq 50.0)$ TeV^{-4}, using formula (6.2). Taking eight energy points, two channels and ten bins in $\cos\theta$ this corresponds to at most 160 entries when fitting all data. The full error matrix including all correlations was taken into account when computing the χ^2. The theoretical uncertainty on the prediction was taken account for as an error of 0.4%.

The statistical error was chosen to be the expected error (see Tables B.1 to B.3) from the prediction as the number of events selected for each bin was not always sufficiently high to compute the error as a Gaussian. In the worst case the number of selected events was $N_i = 0$ for a bin i, yielding to an error of zero. In fact, the errors are Poissonian and for low number of events not symmetric. Taking these into account would lead to a more complicated treatment in the fit procedure used here as well in deriving limits at a certain confidence level as the probabilities are not necessarily the same. In a previous check [65], the parameter ϵ was fitted to the angular distributions obtained by subsamples of generated muon pairs of a size corresponding to the statistics in data at the energy considered. A bias in the Gaussian of the pull distribution, $P = \epsilon_{best}/\delta\epsilon$, was observed when the measured errors were used. This disappeared completely using the expected errors. Therefore, taking the expected errors, seems to be a good compromise and will provide reasonable results.

The systematic errors on the differential cross section were described for the $\mu^+\mu^-$ final state in Section 5.3 where the uncorrelated errors due to bin-by-bin corrections were given in Tables 5.10 and 5.11. The fully correlated errors are given in Table 5.12 as a percentage. They account for correlations between energies and years, *e.g.* the error on the efficiency correction, correlations between final states, *e.g.* the statistical and systematical errors on the luminosity, and for completeness the correlations between different experiments which is not needed here, *e.g.* the error on the luminosity arising from the uncertainty on the prediction of the Bhabha cross section. The systematic errors on the $\tau^+\tau^-$ differential cross sections used are divided into correlated and uncorrelated errors in the same way as for the muons. The full set of errors can be found in [64].

The value of ϵ that minimised the χ^2 was found using either only the $\mu^+\mu^-$ final state at different energies year-by-year or using the complete data set, the combination with the $\tau^+\tau^-$ final state. For completeness the $\tau^+\tau^-$ final state only was probed as well. The one sigma error on ϵ_{best} was obtained by taking $\Delta\chi^2 = 1$ for both sides from the minimum. The lower limits on the scale of gravity in extra dimensions, M_s, at 95 % confidence level were derived as one-sided lower limits for both choices of λ that were computed as follows [65]:

$$\Xi_B = \frac{1}{(\Lambda + 1.64\,\sigma_\Lambda^+)^{\frac{1}{4}}}, \tag{6.8}$$

where $\Lambda = \epsilon_{best}/\lambda$ and σ_Λ^+ the upper one sigma error on this, with λ having the sign referring to ϵ_{best} (*e.g.* a negative value for ϵ_{best} corresponds to $\lambda = -1$). For λ with the opposite sign the lower limit was obtained from setting ϵ to zero, *i.e.* the Standard Model value, and using the average of the upper and lower uncertainties on ϵ_{best}:

$$\Xi_O = \frac{1}{(1.64\,\sigma_\Lambda)^{\frac{1}{4}}}, \tag{6.9}$$

where

$$\sigma_\Lambda = \frac{1}{2}(\sigma_\Lambda^+ + \sigma_\Lambda^-). \tag{6.10}$$

The best fit values obtained for ϵ, using both final states separately as well as the combination of them, are shown in Table 6.5, together with the extracted lower limits on the scale of quantum gravity, M_s, for both choices of λ, where $M_s > \Xi_B, \Xi_O$, respectively. Using all available data from all energies considered here yields to a value of ϵ_{best} consistent with the Standard Model ($\epsilon = 0$):

$$\epsilon_{best} = +0.12^{+1.46}_{-1.47} \quad \mathrm{TeV}^{-4}.$$

The lower limit on M_s in this case was found to be 794 GeV. Using the single final states alone or using only single energy points yielded, of course, to less stringent values for M_s^{low}. The value for ϵ_{best} in each case is as well consistent with $\epsilon = 0$. The obtained results improved with respect to previous analyses where only lower energies from LEP II were included [55], [65]. The best fit values and the 95% confidence level limits are shown as a function of $\cos\theta$ and as a ratio to the Standard Model predictions together with the data in Figures 6.12 ($\mu^+\mu^-$), 6.13 ($\tau^+\tau^-$), 6.14 (l^+l^-) and 6.15 (183-207 GeV). The χ^2 curves for the latter are shown in Figure 6.16. The asymmetry in the shape arises from the constructive and destructive interference from the sign of λ.

A fit to the differential cross sections of the $e^+e^- \to e^+e^-$ process from 183 to 207 GeV was performed by a different analysis in the DELPHI collaboration and yielded to [51]:

$$\epsilon_{best} = +0.00^{+0.38}_{-0.40} \quad \mathrm{TeV}^{-4},$$

with a lower limit on M_s of 1.06 TeV. Including both, the electron and the muon/tau final states resulted in a very similar bound. The electron channel, thus, is the most sensitive one for these effects as the t-channel contribution to the process yields to significant larger interference terms.

6.3.4 Limits from other Experiments

The limits presented here have been compared to the results obtained by the other experiments at LEP. The values achieved for ϵ_{best} are consistent with the Standard Model ($\epsilon = 0$).

Table 6.4 summarises the derived limits for $\mathrm{M_s}$ using different final states as well as a combination of them. Most of the results have been shown at winter conference in 2001, some have been updated meanwhile, specially the limits from the $e^+e^- \to e^+e^-$ and the $e^+e^- \to \gamma\gamma$ channels, but still are preliminary. The limits from ALEPH, L3 and OPAL for $\mu^+\mu^-$ and $\tau^+\tau^-$ as well as for the hadronic channel included data up to 189 GeV [66], [67]. The results from OPAL for l^+l^- includes also the $\gamma\gamma$ and the ZZ channel from 183 to 207 GeV [68]. The most sensitive channels at LEP, the $e^+e^- \to e^+e^-$ and the $e^+e^- \to \gamma\gamma$ process, have been averaged by the electroweak working group[5] using data from 183 to 209 GeV to derive limits, yielding to $\mathrm{M_s}^{\pm} > 1.13/1.28\,\mathrm{TeV}$ and $\mathrm{M_s}^{\pm} > 0.95/1.14\,\mathrm{TeV}$, respectively, combining both gives $\mathrm{M_s}^{\pm} > 1.13/1.39\,\mathrm{TeV}$ [69] .

Limits on the string mass scale, $\mathrm{M_s}$ (GeV), $\lambda = +/-1$ at 95% CL				
	LEP Experiment			
Final State	ALEPH	DELPHI	L3	OPAL
$\mu^+\mu^-$	669/652	**713/775**	690/560	600/630
$\tau^+\tau^-$	598/616	**675/604**	540/580	630/500
$\mu^+\mu^-/\ \tau^+\tau^-$	-	**794/804**	-	680/610
e^+e^-	813/1045	1007/1007	980/1060	1000/1150
l^+l^-	-	1008/1008	-	1030/1170
$q\bar{q}$	572/527	-	490/490	-
$\gamma\gamma$	800/850	830/910	840/990	805/956
ZZ	-	-	770/760	830/590
W^+W^-	-	-	790/680	-

Table 6.4: The limits on $\mathrm{M_s}$ at 95% CL obtained from the LEP experiments using different final states as well as a combination of them. The results for the $\mu^+\mu^-$ and $\tau^+\tau^-$ channel from DELPHI are from the analysis presented here.

Searches for virtual effects from theories with large extra dimensions have also been reported from Tevatron [70]. The DØ experiment considered the di-electron and di-photon angular distributions using the entire sample of data corresponding to $\approx 130(\mathrm{pb})^{-1}$. A lower limit on the mass scale $\mathrm{M_s}$ of 1.2 TeV at 95% CL was found where a different definition of the parameter $\frac{\lambda}{\mathrm{M_s^4}} = \frac{\pi}{2}\frac{1}{\Lambda_T^4}$ was used ($\Lambda_T \approx 1.12\,\mathrm{M_s}$) [19]. Results from HERA experiments (H1 and ZEUS) [71] on the search for virtual graviton exchange were derived using deep inelastic neutral current events with high Q^2. The differential cross section was given as a function of Q^2 for the process $e^+q \to e^+q$. An effect would be measurable at $Q^2 > 10^4\,\mathrm{GeV}^2$. The combination of e^-p and e^+p data yielded to very similar limits on $\mathrm{M_s}$ of about 0.8 TeV for both experiments.

Limits from direct searches for a graviton propagation with a signal of single photon production with missing energy have been derived by LEP experiments, resulting to a $\mathrm{M_s}$ dependent on the number of extra dimension between 1.4 TeV (for $n = 2$) and 0.6 TeV (for $n = 6$) [72].

[5]From Winter conference 2001 without DELPHI data for electrons

Final State	Year	$\sqrt{s}$ (GeV)	ϵ_{best} (TeV)$^{-4}$	λ	M_S(TeV)
$\mu^+\mu^-$	1997	183	$-3.01^{+7.74}_{-8.25}$	-1	0.496
				$+1$	0.526
	1998	189	$-1.69^{+3.86}_{-4.24}$	-1	0.583
				$+1$	0.623
	1999	$192-196$	$+5.25^{+2.72}_{-2.82}$	-1	0.685
				$+1$	0.567
	2000	$205-207$	$-0.47^{+2.53}_{-2.73}$	-1	0.671
				$+1$	0.694
	1997 -2000	$183-207$	$+1.12^{+1.68}_{-1.70}$	-1	0.775
				$+1$	0.713
$\tau^+\tau^-$	1997	183	$-16.79^{+13.64}_{-14.90}$	-1	0.395
				$+1$	0.455
	1998	189	$-2.87^{+6.51}_{-6.97}$	-1	0.514
				$+1$	0.548
	1999	$192-196$	$+6.50^{+4.15}_{-4.43}$	-1	0.614
				$+1$	0.523
	2000	$205-207$	$-10.92^{+5.26}_{-5.40}$	-1	0.474
				$+1$	0.582
	1997-2000	$183-207$	$-2.80^{+3.01}_{-2.88}$	-1	0.604
				$+1$	0.675
l^+l^-	1997	183	$-6.80^{+6.91}_{-7.08}$	-1	0.483
				$+1$	0.543
	1998	189	$-2.15^{+3.47}_{-3.47}$	-1	0.598
				$+1$	0.647
	1999	$192-196$	$+5.63^{+2.26}_{-2.39}$	-1	0.572
				$+1$	0.716
	2000	$205-207$	$-2.85^{+2.26}_{-2.44}$	-1	0.618
				$+1$	0.714
	1997-2000	$183-207$	$+0.12^{+1.46}_{-1.47}$	-1	0.804
				$+1$	0.794

Table 6.5: The best fit values for the parameter ϵ in quantum gravity in extra dimensions, together with the lower limits on the string scale, M_s, at 95% CL obtained for $\mu^+\mu^-$ and $\tau^+\tau^-$ final states as well for the combination of both (l^+l^-) at different energies.

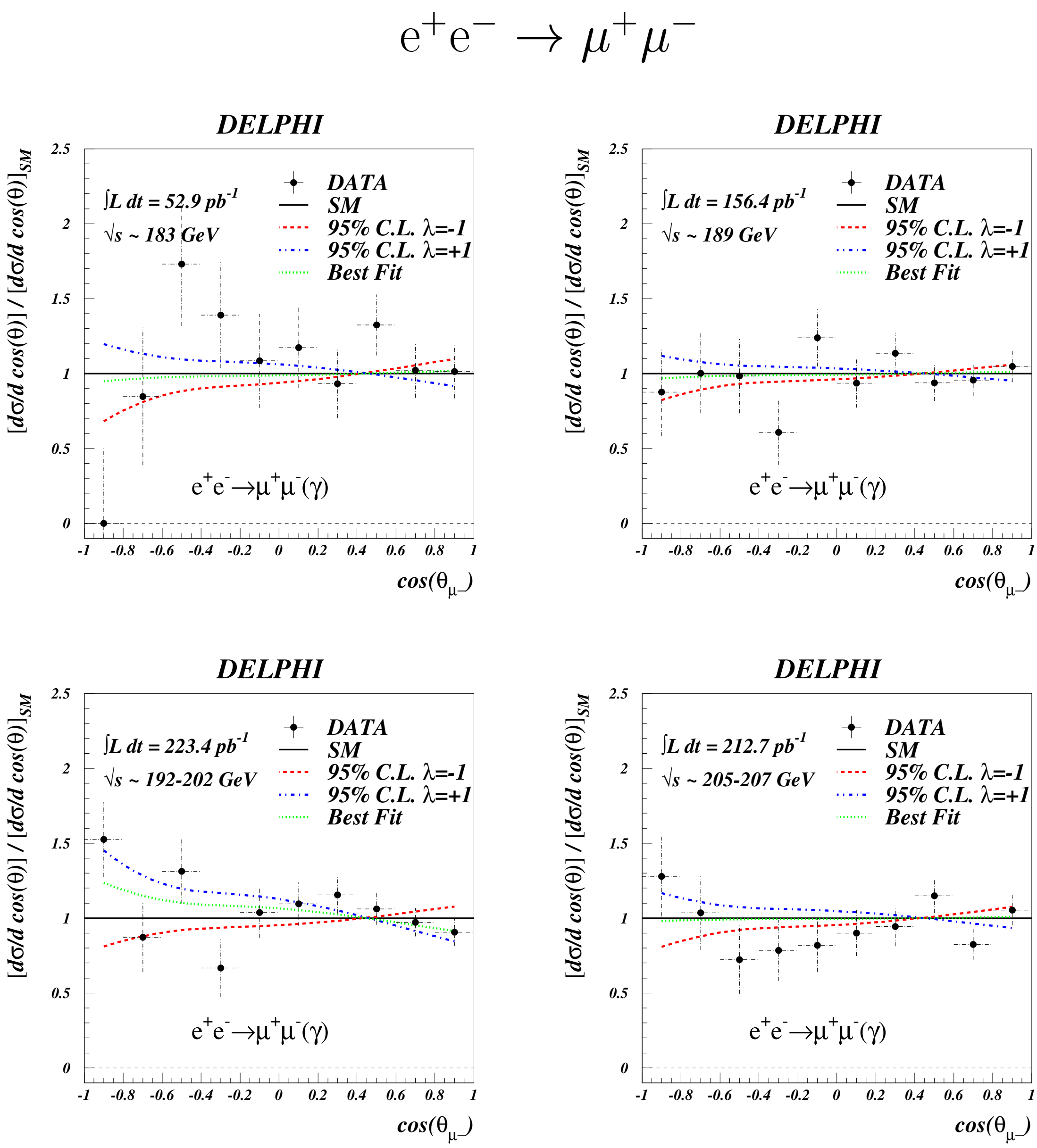

Figure 6.12: The ratio of the differential cross sections for the fits including quantum gravity (curves) and the data (points) to the Standard Model expectation obtained for the process $e^+e^- \to \mu^+\mu^-$ for each years data sample (1997-2000). The curves show the best fit to the data as well as the 95% confidence level limits for both choices of λ.

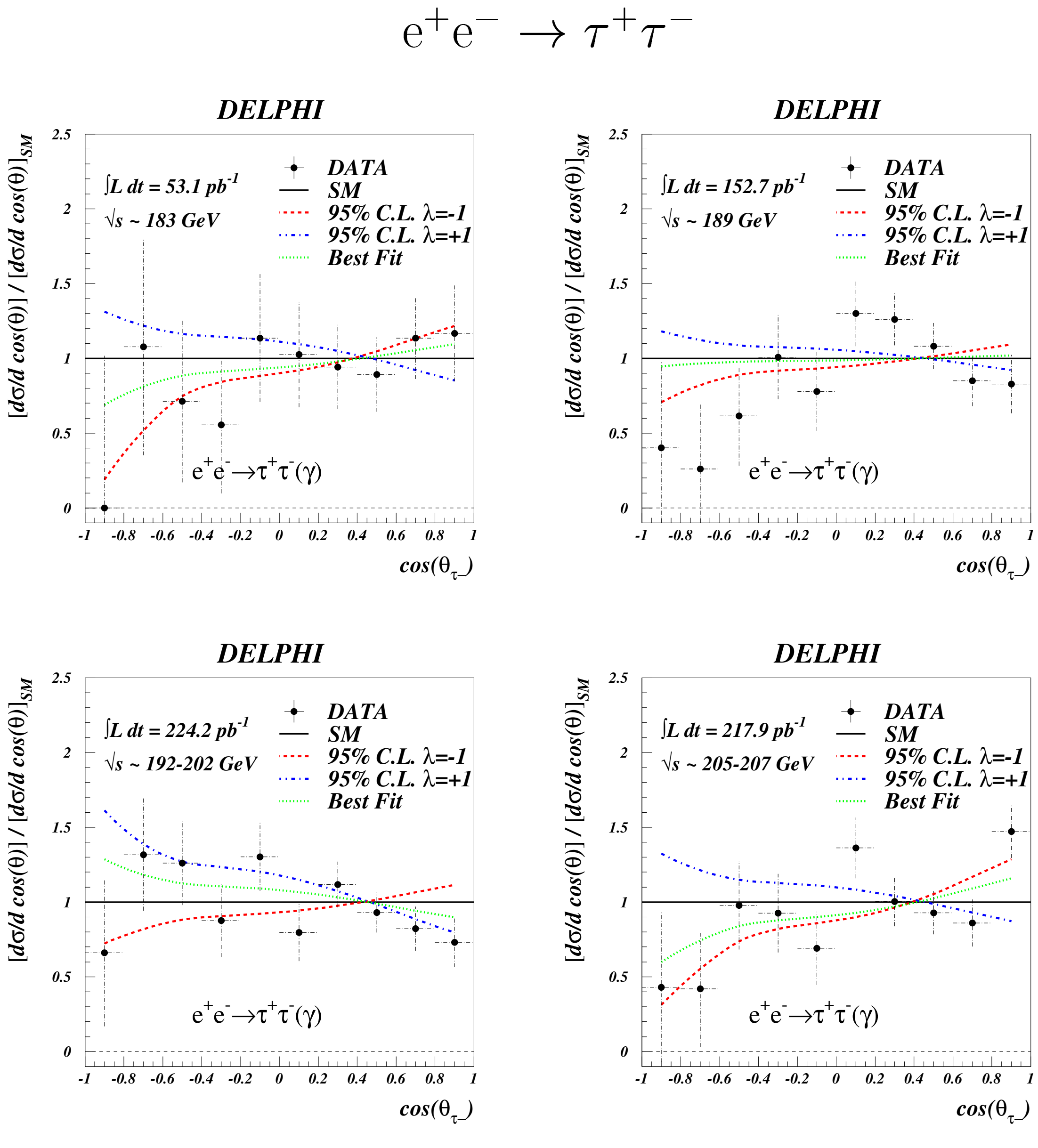

Figure 6.13: The ratio of the differential cross sections for the fits including quantum gravity (curves) and the data (points) to the Standard Model expectation obtained for the process $e^+e^- \to \tau^+\tau^-$ for each years data sample (1997-2000). The curves show the best fit to the data as well as the 95% confidence level limits for both choices of λ.

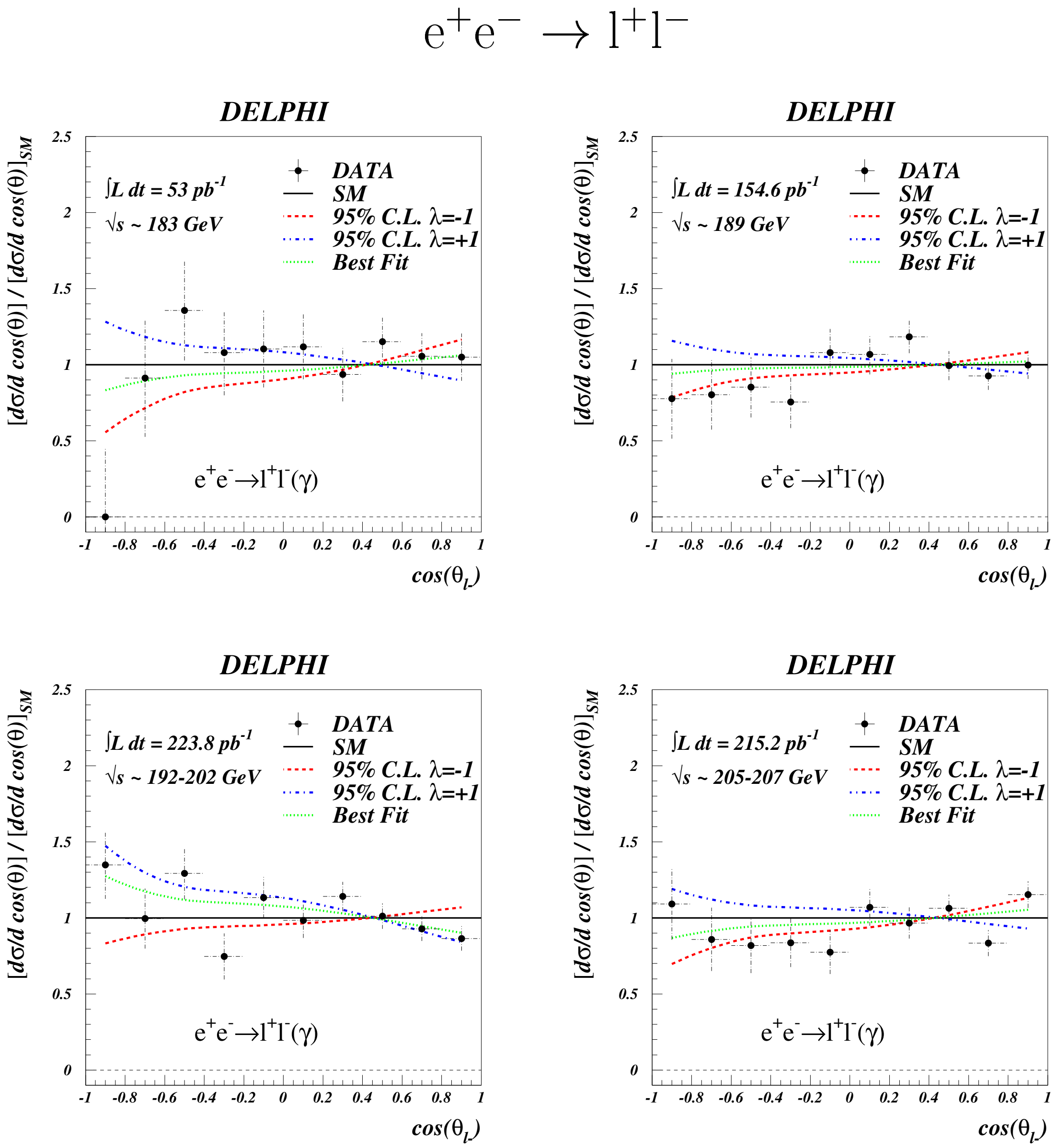

Figure 6.14: The ratio of the differential cross sections for the fits including quantum gravity (curves) and the data (points) to the Standard Model expectation obtained for the process $e^+e^- \to l^+l^-$ ($\mu^+\mu^-$, $\tau^+\tau^-$) for each years data sample (1997-2000). The curves show the best fit to the data as well as the 95% confidence level limits for both choices of λ.

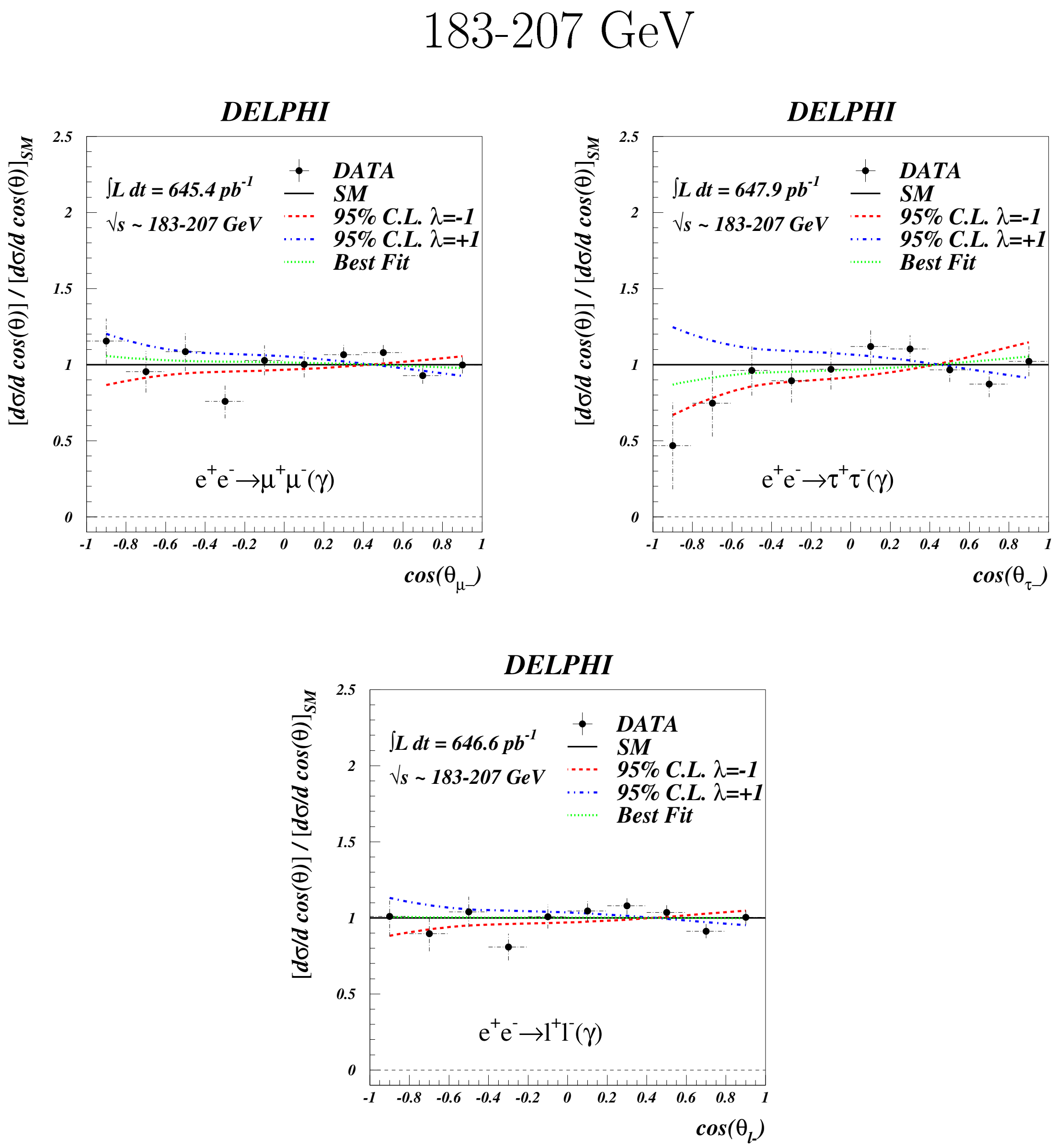

Figure 6.15: The ratio of the differential cross sections for the fits including quantum gravity (curves) and the data (points) to the Standard Model expectation obtained for the processes $e^+e^- \to \mu^+\mu^-$, $e^+e^- \to \tau^+\tau^-$ and the combination of both using all years data samples at energies from 183 to 207 GeV. The curves show the best fit to the data as well as the 95% confidence level limits for both choices of λ.

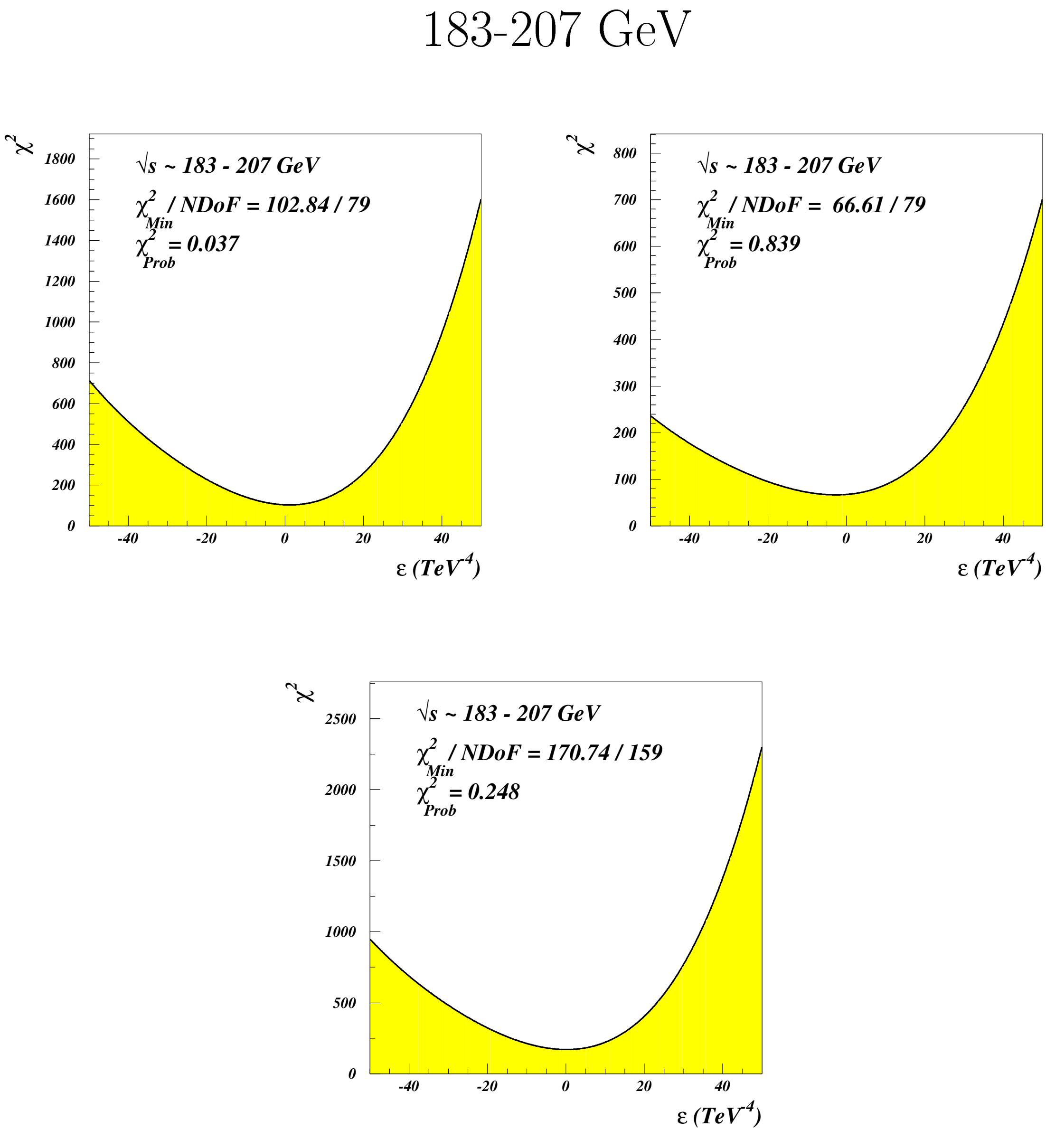

Figure 6.16: The χ^2 curves obtained for the quantum gravity fits to the $\mu^+\mu^-$ (top left) and $\tau^+\tau^-$ (top right) final states and the combination of both using all years data samples at energies from 183 to 207 GeV (bottom).

Chapter 7

Conclusions

This thesis presents the measurement of muon-pair production from the e^+e^--annihilation at energies well above the Z resonance which were considered as the final results of the DELPHI Collaboration. The analysis is based on a total data set corresponding to a luminosity of ~ 650 pb^{-1} at nominal center-of-mass energies from 183 to 207 GeV, collected from 1997 to 2000 at LEP with the DELPHI detector.

The $e^+e^- \to \mu^+\mu^-$ process provides a clear signature for selecting muon pairs with high efficiencies above 90%. The muon as a minimal ionising particle (MIP) allows a solid particle identification using a combination of the calorimetry and muon chambers. Due to large radiative corrections leading to a reduction of the effective center-of-mass energy, $\sqrt{s'}$, the data sets have been divided into two subsamples: (i) an *inclusive* sample that included also radiative events down to $\sqrt{s'} \geq 75$ GeV, and (ii) a *non-radiative* sample with a cut of $\sqrt{s'}/\sqrt{s} > 0.85$ that allowed only *soft* photon radiation. $\sqrt{s'}$ was defined to be the bare invariant mass of the final muon-pair and was obtained by a kinematic fit. Measurements of the total cross section and the forward-backward asymmetry for each of the eight energy points have been made with both subsamples, using in total about 3700 events for (i) and 1600 for (ii). Differential cross sections have been computed only for the non-radiative sample. The error of the measurement was dominated by the statistical uncertainty at a single energy point, e.g $\Delta_{stat} = 4.9\%$ at 189 GeV for the non-radiative $\sigma_{\mu\mu}$. Different sources of the systematic error have been investigated yielding to a total value of $\mathcal{O}(1\%)$ for the cross section measurement, with major contributions coming from the errors on the efficiency and the luminosity.

The results for the measurement of $\sigma, \mathrm{A_{FB}}$, and $d\sigma/d\cos\theta$ from the $e^+e^- \to \mu^+\mu^-$ process have been compared to the predictions from the Standard Model, computed with the ZFITTER program (v. 6.36). They were found to be in a good agreement, no significant deviations were observed. The ratio of the measurement to the SM has been computed using the combination of all $\sigma_{\mu\mu}$ taking into account the full error matrix, yielding on average to:

$$\boldsymbol{\sigma_{\mu\mu}:} \qquad \boldsymbol{\langle\mathcal{R}\rangle_{incl} = 1.004 \pm 0.020} \qquad \boldsymbol{\langle\mathcal{R}\rangle_{nrad} = 0.997 \pm 0.026.}$$

The difference to the SM was computed for $\mathrm{A_{FB}^{\mu\mu}}$ accordingly, resulting on average to:

$$\boldsymbol{\mathrm{A_{FB}^{\mu\mu}}:} \qquad \boldsymbol{\langle\mathcal{D}\rangle_{incl} = 0.008 \pm 0.017} \qquad \boldsymbol{\langle\mathcal{D}\rangle_{nrad} = 0.010 \pm 0.021.}$$

An overall χ^2 was computed taking into account the full error matrix, yielding to (4.4/58.0)% for $\sigma_{\mu\mu}$ and (87.0/97.0)% for $\mathrm{A_{FB}^{\mu\mu}}$ (non-rad./incl. respectively). Discrepancies observed in the angular distributions have been investigated and found to be statistical fluctuations. Here, an overall χ^2/ndof of 103.3/80 was achieved.

The non-radiative measurements that are most sensitive to new physics phenomena were used to probe the effects coming from an additional heavy gauge boson, Z', and from a spin-2 graviton in quantum gravity in large extra dimensions. No evidence for the existence of any of these considered particles was found. Lower limits at 95% confidence level were derived using a χ^2 fit.

The limits on $\mathrm{M_{Z'}}$ and $\theta_{\mathrm{ZZ'}}$, the parameter of a possible Z', have been achieved using the measurements of the leptonic and hadronic $\sigma(\mu^+\mu^-, \tau^+\tau^-, \mathrm{q\bar{q}})$ and the measurement of the leptonic $\mathrm{A_{FB}}(\mu^+\mu^-, \tau^+\tau^-)$ at LEP II energies (130 to 207 GeV), together with results for σ and $\mathrm{A_{FB}}$ measured at LEP I. For the different models considered ($\mathrm{E_6}$,L-R) this yielded to:

$$\mathbf{M_{Z'} > 360 - 530\ GeV/c^2}$$

In the sequential SM the mass must be > 1300 GeV/c^2. The value of $\theta_{\mathrm{ZZ'}}$ was found to be consistent with zero, with upper limits between 2.6 and 9.6 mrad. The usage of the LEP II combined results (ADLO) and averaged LEP I measurements in terms of the *pseudo observables* improved the limits to $\mathrm{M_{Z'}} > 435 - 665$ GeV/c^2 and $\theta_{\mathrm{ZZ'}} <$ 1.3-8.2 mrad. In a model independent approach, limits on the normalised couplings of the Z' to the leptons were achieved: $\boldsymbol{|a_l'^N| < 0.19}$ and $\boldsymbol{|v_l'^N| < 0.19}$. The limits were reduced to $|a_l'^N| < 0.14$ and $|v_l'^N| < 0.13$ using the LEP II combined numbers for σ_{ll} and $\mathrm{A_{FB}^{ll}}$ $(l = \mu, \tau)$.

A spin-2 graviton exchange would not alternate the total cross section in fermion-pair production, but rather would affect the angular distribution. The limits on the string scale in a TeV scale quantum gravity were obtained using the differential cross section of the $\mathrm{e^+e^-} \to \mu^+\mu^-, \tau^+\tau^-$ process at energies from 183 to 207 GeV. The best fit value of $\epsilon = \lambda/\mathrm{M_s^4}$ was consistent with the SM value of zero using a combination of all data:

$$\boldsymbol{\epsilon_{best} = +0.12^{+1.46}_{-1.47}\ \mathrm{TeV}^{-4}.}$$

From this, lower limits on $\mathrm{M_s}$ at 95% CL were derived: $\mathbf{M_s > 794/804\ GeV}$ (for $\lambda = +1/-1$).

The search for a Z' particle and spin-2 graviton will be an important subject in future high-energy experiments, like the LHC, a 14 TeV *pp* collider which is expected to be operational in 2007, or a possible large linear $\mathrm{e^+e^-}$ collider. Achieving higher energies and luminosities, exclusion limits will be extended or, hopefully, the discovery limit approached.

Appendix A

Constrained Fit

In this chapter the algorithm used for the reconstruction of $\sqrt{s'}$ with the constrained fitting is described. The method is based on a χ^2 minimization under application of constraints using Lagrange multipliers ([34]). The χ^2 is formed in the following way:

$$\chi^2(\vec{y}) = (\vec{y} - \vec{y}_0)^{\mathsf{T}} \, \mathbf{V^{-1}} \, (\vec{y} - \vec{y}_0), \tag{A.1}$$

with V ($V_{kl} = \sigma_{y_k y_l}$) being the usual error matrix and $\vec{y}, \vec{y}_0$ are vectors containing the measured and the expected quantities respectively. The χ^2 is assumed to be quadratic in the parameters $\vec{y}$. The constraints are given in a vector $\vec{f}(\vec{y})$, with the length equal to the number of constraints. The fitted parameters must then follow:

$$\frac{\partial \chi^2}{\partial \vec{y}} = \vec{0} \qquad \vec{f}(\vec{y}) = \vec{0} \tag{A.2}$$

Lagrange multipliers, λ, are multiplied by the constraints $\vec{f}$ and then added to the χ^2 yielding to a new function $Q(\vec{y}, \vec{f})$:

$$Q(\vec{y}, \vec{\lambda}) = (\vec{y} - \vec{y_0})^{\mathsf{T}} \, \mathbf{V^{-1}} \, (\vec{y} - \vec{y_0}) + 2\,\vec{\lambda} \cdot \vec{f}(\vec{y}) \tag{A.3}$$

$Q(\vec{y}, \vec{\lambda})$ must be minimized as a function of $\vec{y}$ and must be independent of λ as $\vec{f} \equiv 0$. The factor of two is used for convenience. With (A.3) equation (A.2) becomes:

$$\frac{\partial Q}{\partial \vec{y}} = \vec{0} \qquad \frac{\partial Q}{\partial \vec{\lambda}} = \vec{0} \tag{A.4}$$

The constraints are first-order Taylor expanded to make the minimization linear.

$$\vec{f}(\vec{y}) = \vec{f}(\vec{y}^{(l)}) + \mathbf{B}(\vec{y} - \vec{y}^{(l)}) \tag{A.5}$$

where

$$\mathbf{B} = \frac{\partial \vec{f}(\vec{y})}{\partial \vec{y}} \,|_{\vec{y}=\vec{y}^{(l)}} \tag{A.6}$$

Minimizing $Q(\vec{y},\vec{\lambda})$ the first time there will remain a second order part of the constraints. Therefore an iterative procedure follows consequently minimizing in the next step:

$$Q(\vec{y}^{(l+1)},\vec{\lambda}) = (\vec{y}^{(l+1)} - \vec{y_0})^{\mathsf{T}}\,\mathbf{V^{-1}}\,(\vec{y}^{(l+1)} - \vec{y_0}) + 2\,\vec{\lambda}\cdot(\vec{f}(\vec{y}^l) + \mathbf{B}(\vec{y}^{(l+1)} - \vec{y}^l) \tag{A.7}$$

Multiplying equation (A.4) by one half and differentiating with respect to $\vec{y}^{(l+1)}$ and $\vec{\lambda}$ gives:

$$\begin{aligned} \frac{1}{2}\frac{\partial Q}{\partial \vec{y}^{(l+1)}} = \mathbf{V}^{-1}(\vec{y}^{(l+1)} - \vec{y_0}) + \mathbf{B}^{\mathsf{T}}\vec{\lambda} &= \vec{0} \\ \frac{1}{2}\frac{\partial Q}{\partial \vec{y}} = \vec{f}(\vec{y}^{(l)}) + \mathbf{B}(\vec{y}^{(l+1)} - \vec{y}^{(l)}) &= \vec{0} \end{aligned} \tag{A.8}$$

which can be expressed in matrix form:

$$\begin{pmatrix} \mathbf{V}^{-1} & \mathbf{B}^{\mathsf{T}} \\ \mathbf{B} & 0 \end{pmatrix} \begin{pmatrix} \vec{y}^{(l+1)} \\ \vec{\lambda} \end{pmatrix} = \begin{pmatrix} \mathbf{V^{-1}}\vec{y_0} \\ -\vec{f}(\vec{y}^{(l)}) + \mathbf{B}\vec{y}^{(l)} \end{pmatrix} \tag{A.9}$$

Inverting the matrix on the left side yields:

$$\begin{pmatrix} \mathbf{V}^{-1} & \mathbf{B}^{\mathsf{T}} \\ \mathbf{B} & 0 \end{pmatrix}^{-1} = \begin{pmatrix} \mathbf{V} - \mathbf{VB}^{\mathsf{T}}\left(\mathbf{BVB}^{\mathsf{T}}\right)^{-1}\mathbf{BV} & \mathbf{VB}^{\mathsf{T}}\left(\mathbf{BVB}^{\mathsf{T}}\right)^{-1} \\ \left(\mathbf{BVB}^{\mathsf{T}}\right)^{-1}\mathbf{BV} & -\left(\mathbf{BVB}^{\mathsf{T}}\right)^{-1} \end{pmatrix} \tag{A.10}$$

This gives an formula determing $\vec{y}^{(l+1)}$ recursively:

$$\vec{y}^{(l+1)} = \vec{y_0} + \mathbf{VB}^{\mathsf{T}}\left(\mathbf{BVB}^{\mathsf{T}}\right)^{-1}\left(\mathbf{B}\left(\vec{y}^{(l)} - \vec{y_0}\right) - \vec{f}(\vec{y}^{(l)})\right) \tag{A.11}$$

The iterative expression of chosen parameters $\vec{y}$ has to converge and minimize the χ^2 under the kinematic constraints in $\vec{f}(\vec{y})$.

Appendix B

Bin-by-bin Corrections on $d\sigma/d\cos\theta$

$d\sigma/d\cos\theta$ ($e^+e^- \to \mu^+\mu^-$)						non-radiative		$\sqrt{s} \sim 183$ GeV	
$\cos\theta$		Δ^{exp}_{stat}	Δ^{Qmisid}_{syst}	N_{exp}	N_{sel}	ϵ_{sel}	F_{mig}	N_{bgd}	N_{cos}
-0.97	-0.80	0.243	-0.0002	3.78	0.0	90.26±1.44	1.005±0.020	0.04±0.02	0.00±0.00
-0.80	-0.60	0.223	-0.0001	4.64	4.0	93.57±1.16	1.027±0.013	0.06±0.06	0.03±0.02
-0.60	-0.40	0.238	-0.0001	5.80	10.0	95.13±0.84	1.003±0.010	0.05±0.04	0.10±0.04
-0.40	-0.20	0.270	0.0000	7.96	11.0	97.08±0.59	1.001±0.007	0.03±0.02	0.25±0.06
-0.20	0.00	0.330	0.0000	10.12	11.0	93.56±0.76	1.016±0.007	0.03±0.02	0.06±0.03
0.00	0.20	0.389	0.0000	13.64	16.0	91.39±0.74	1.011±0.006	0.05±0.03	0.13±0.04
0.20	0.40	0.438	0.0000	19.29	18.0	96.19±0.44	1.001±0.005	0.05±0.03	0.06±0.03
0.40	0.60	0.512	0.0001	24.14	32.0	94.40±0.46	1.026±0.005	0.06±0.04	0.06±0.03
0.60	0.80	0.585	0.0001	30.29	31.0	92.91±0.45	1.030±0.005	0.10±0.06	0.06±0.03
0.80	0.97	0.713	0.0002	31.46	32.0	92.07±0.46	1.035±0.006	0.09±0.06	0.00±0.00

$d\sigma/d\cos\theta$ ($e^+e^- \to \mu^+\mu^-$)						non-radiative		$\sqrt{s} \sim 189$ GeV	
$\cos\theta$		Δ^{exp}_{stat}	Δ^{Qmisid}_{syst}	N_{exp}	N_{sel}	ϵ_{sel}	F_{mig}	N_{bgd}	N_{cos}
-0.97	-0.80	0.137	-0.0001	11.23	10.0	94.82±1.05	1.022±0.013	0.03±0.03	0.00±0.00
-0.80	-0.60	0.125	-0.0001	13.81	14.0	94.43±1.02	1.004±0.009	0.04±0.03	0.32±0.08
-0.60	-0.40	0.135	-0.0001	16.14	16.0	93.16±1.01	0.997±0.007	0.02±0.01	0.42±0.09
-0.40	-0.20	0.155	-0.0001	21.18	13.0	97.71±0.53	1.028±0.008	0.08±0.05	0.14±0.05
-0.20	0.00	0.186	0.0000	27.45	34.0	93.08±0.77	1.034±0.007	0.06±0.05	0.28±0.07
0.00	0.20	0.218	0.0000	37.30	35.0	92.22±0.71	1.022±0.006	0.05±0.04	0.18±0.06
0.20	0.40	0.245	0.0001	52.79	60.0	96.77±0.40	1.016±0.005	0.13±0.08	0.32±0.08
0.40	0.60	0.282	0.0001	67.99	64.0	95.27±0.43	1.012±0.004	0.12±0.08	0.18±0.06
0.60	0.80	0.321	0.0001	86.44	83.0	94.30±0.40	1.008±0.004	0.21±0.13	0.14±0.05
0.80	0.97	0.390	0.0001	90.19	95.0	94.07±0.40	1.018±0.004	0.26±0.16	0.05±0.03

Table B.1: Bin-by-bin corrections and expected statistical errors on $d\sigma_{\mu\mu}/\cos\theta$ (183-189 GeV)

$d\sigma/d\cos\theta$ ($e^+e^- \to \mu^+\mu^-$)						non-radiative		$\sqrt{s} \sim 192$ GeV	
$\cos\theta$		Δ^{exp}_{stat}	Δ^{Qmisid}_{syst}	N_{exp}	N_{sel}	ϵ_{sel}	F_{mig}	N_{bgd}	N_{cos}
-0.97	-0.80	0.329	-0.0001	1.90	0.0	94.08±0.80	1.001±0.009	0.04±0.03	0.01±0.00
-0.80	-0.60	0.309	-0.0001	2.16	1.0	94.75±0.68	1.030±0.007	0.01±0.01	0.02±0.01
-0.60	-0.40	0.332	-0.0001	2.56	4.0	95.39±0.61	1.012±0.006	0.00±0.00	0.01±0.00
-0.40	-0.20	0.383	-0.0001	3.27	2.0	94.71±0.57	1.034±0.007	0.01±0.01	0.03±0.01
-0.20	0.00	0.454	0.0000	4.31	5.0	92.31±0.57	1.033±0.006	0.00±0.00	0.02±0.01
0.00	0.20	0.538	0.0000	5.67	3.0	90.27±0.55	1.049±0.006	0.03±0.02	0.02±0.01
0.20	0.40	0.603	0.0001	8.09	14.0	95.10±0.34	1.035±0.004	0.02±0.01	0.04±0.01
0.40	0.60	0.680	0.0001	10.87	11.0	95.45±0.30	1.010±0.003	0.05±0.03	0.04±0.01
0.60	0.80	0.775	0.0001	13.76	11.0	94.10±0.29	1.006±0.002	0.04±0.03	0.02±0.01
0.80	0.97	0.941	0.0001	14.42	13.0	93.64±0.29	1.007±0.002	0.04±0.03	0.00±0.00

$d\sigma/d\cos\theta$ ($e^+e^- \to \mu^+\mu^-$)						non-radiative		$\sqrt{s} \sim 196$ GeV	
$\cos\theta$		Δ^{exp}_{stat}	Δ^{Qmisid}_{syst}	N_{exp}	N_{sel}	ϵ_{sel}	F_{mig}	N_{bgd}	N_{cos}
-0.97	-0.80	0.194	-0.0001	5.23	8.0	95.04±0.71	1.020±0.010	0.06±0.04	0.03±0.01
-0.80	-0.60	0.179	-0.0001	6.12	7.0	94.80±0.69	1.016±0.007	0.04±0.03	0.05±0.01
-0.60	-0.40	0.192	-0.0001	7.11	9.0	95.42±0.60	1.008±0.005	0.01±0.01	0.02±0.01
-0.40	-0.20	0.222	-0.0001	8.91	3.0	94.50±0.56	1.041±0.007	0.02±0.02	0.08±0.02
-0.20	0.00	0.263	0.0000	11.73	11.0	92.14±0.59	1.042±0.007	0.05±0.03	0.05±0.01
0.00	0.20	0.308	0.0000	15.81	22.0	91.28±0.53	1.045±0.006	0.13±0.07	0.07±0.02
0.20	0.40	0.348	0.0001	22.02	18.0	94.90±0.35	1.040±0.004	0.14±0.09	0.10±0.02
0.40	0.60	0.391	0.0001	29.83	29.0	96.01±0.28	1.011±0.003	0.09±0.05	0.10±0.02
0.60	0.80	0.447	0.0001	37.61	40.0	94.39±0.29	1.009±0.002	0.12±0.06	0.07±0.02
0.80	0.97	0.542	0.0001	39.60	32.0	94.18±0.28	1.010±0.002	0.14±0.09	0.00±0.00

$d\sigma/d\cos\theta$ ($e^+e^- \to \mu^+\mu^-$)						non-radiative		$\sqrt{s} \sim 200$ GeV	
$\cos\theta$		Δ^{exp}_{stat}	Δ^{Qmisid}_{syst}	N_{exp}	N_{sel}	ϵ_{sel}	F_{mig}	N_{bgd}	N_{cos}
-0.97	-0.80	0.181	-0.0001	5.78	7.0	94.15±0.78	1.011±0.009	0.10±0.07	0.04±0.01
-0.80	-0.60	0.167	-0.0001	6.65	4.0	94.23±0.72	1.015±0.007	0.03±0.02	0.05±0.02
-0.60	-0.40	0.178	-0.0001	7.75	13.0	95.70±0.56	1.009±0.006	0.02±0.02	0.02±0.01
-0.40	-0.20	0.203	0.0000	9.90	11.0	95.25±0.55	1.023±0.007	0.06±0.03	0.09±0.02
-0.20	0.00	0.243	0.0000	12.56	16.0	91.53±0.60	1.041±0.006	0.08±0.05	0.05±0.02
0.00	0.20	0.282	0.0000	17.07	21.0	91.51±0.52	1.038±0.005	0.11±0.06	0.07±0.02
0.20	0.40	0.321	0.0000	23.51	25.0	95.24±0.34	1.047±0.005	0.12±0.07	0.11±0.03
0.40	0.60	0.363	0.0001	31.54	42.0	95.12±0.30	1.015±0.003	0.06±0.05	0.11±0.03
0.60	0.80	0.412	0.0001	40.20	43.0	94.72±0.28	1.015±0.002	0.10±0.06	0.07±0.02
0.80	0.97	0.502	0.0001	41.96	41.0	93.35±0.30	1.013±0.003	0.13±0.07	0.00±0.00

Table B.2: Bin-by-bin corrections and expected statistical errors on $d\sigma_{\mu\mu}/\cos\theta$ (192-200 GeV)

$d\sigma/d\cos\theta$ $(e^+e^- \to \mu^+\mu^-)$						non-radiative		$\sqrt{s} \sim 202$ GeV	
$\cos\theta$		Δ^{exp}_{stat}	Δ^{Qmisid}_{syst}	N_{exp}	N_{sel}	ϵ_{sel}	F_{mig}	N_{bgd}	N_{cos}
-0.97	-0.80	0.260	-0.0001	2.72	9.0	93.45±0.78	1.016±0.009	0.02±0.02	0.02±0.01
-0.80	-0.60	0.238	-0.0001	3.18	4.0	93.43±0.72	1.015±0.007	0.02±0.02	0.03±0.01
-0.60	-0.40	0.250	-0.0001	3.77	2.0	96.88±0.49	1.009±0.006	0.03±0.02	0.01±0.01
-0.40	-0.20	0.290	-0.0001	4.64	2.0	94.97±0.54	1.033±0.007	0.01±0.01	0.05±0.01
-0.20	0.00	0.343	0.0000	6.01	4.0	91.92±0.57	1.041±0.007	0.04±0.02	0.03±0.01
0.00	0.20	0.403	0.0000	8.00	5.0	90.94±0.51	1.043±0.005	0.02±0.01	0.04±0.01
0.20	0.40	0.454	0.0001	11.23	18.0	95.72±0.32	1.046±0.004	0.05±0.03	0.05±0.01
0.40	0.60	0.512	0.0001	15.08	11.0	95.38±0.29	1.013±0.003	0.06±0.03	0.05±0.01
0.60	0.80	0.585	0.0001	19.02	14.0	94.14±0.29	1.014±0.003	0.05±0.03	0.04±0.01
0.80	0.97	0.706	0.0001	20.25	20.0	93.90±0.28	1.008±0.002	0.14±0.08	0.00±0.00

$d\sigma/d\cos\theta$ $(e^+e^- \to \mu^+\mu^-)$						non-radiative		$\sqrt{s} \sim 205$ GeV	
$\cos\theta$		Δ^{exp}_{stat}	Δ^{Qmisid}_{syst}	N_{exp}	N_{sel}	ϵ_{sel}	F_{mig}	N_{bgd}	N_{cos}
-0.97	-0.80	0.140	-0.0002	8.88	10.0	94.61±0.73	1.014±0.010	0.04±0.03	0.00±0.00
-0.80	-0.60	0.127	-0.0002	10.38	12.0	93.36±0.75	1.014±0.007	0.02±0.02	0.11±0.03
-0.60	-0.40	0.134	-0.0003	12.18	11.0	97.15±0.46	1.004±0.005	0.02±0.01	0.07±0.02
-0.40	-0.20	0.152	0.0001	15.33	14.0	96.64±0.45	1.010±0.006	0.04±0.03	0.04±0.02
-0.20	0.00	0.178	0.0000	20.20	18.0	94.03±0.51	1.011±0.005	0.09±0.06	0.07±0.02
0.00	0.20	0.208	0.0000	26.99	25.0	92.97±0.48	1.023±0.005	0.06±0.04	0.11±0.03
0.20	0.40	0.236	0.0001	37.24	36.0	96.42±0.30	1.015±0.004	0.07±0.04	0.09±0.02
0.40	0.60	0.271	0.0003	48.33	67.0	95.67±0.29	1.011±0.003	0.13±0.10	0.09±0.02
0.60	0.80	0.309	0.0002	61.20	49.0	93.84±0.30	1.015±0.002	0.08±0.05	0.13±0.03
0.80	0.97	0.377	0.0002	63.65	56.0	93.09±0.31	1.024±0.003	0.22±0.12	0.00±0.00

$d\sigma/d\cos\theta$ $(e^+e^- \to \mu^+\mu^-)$						non-radiative		$\sqrt{s} \sim 207$ GeV	
$\cos\theta$		Δ^{exp}_{stat}	Δ^{Qmisid}_{syst}	N_{exp}	N_{sel}	ϵ_{sel}	F_{mig}	N_{bgd}	N_{cos}
-0.97	-0.80	0.177	-0.0001	5.53	5.0	91.60±0.89	1.001±0.011	0.08±0.06	0.00±0.00
-0.80	-0.60	0.161	-0.0001	6.47	5.0	94.32±0.69	1.031±0.007	0.03±0.03	0.13±0.03
-0.60	-0.40	0.170	-0.0001	7.56	7.0	95.00±0.63	1.003±0.005	0.06±0.05	0.08±0.02
-0.40	-0.20	0.193	0.0000	9.50	10.0	96.22±0.49	1.020±0.006	0.02±0.02	0.05±0.02
-0.20	0.00	0.225	0.0000	12.61	14.0	94.90±0.48	1.025±0.005	0.11±0.07	0.08±0.02
0.00	0.20	0.264	0.0000	16.74	18.0	92.94±0.48	1.017±0.005	0.05±0.03	0.13±0.03
0.20	0.40	0.299	0.0000	23.16	20.0	96.54±0.30	1.016±0.004	0.10±0.06	0.10±0.03
0.40	0.60	0.343	0.0001	30.00	39.0	94.99±0.31	1.008±0.003	0.10±0.07	0.10±0.03
0.60	0.80	0.391	0.0001	38.03	29.0	94.01±0.30	1.011±0.003	0.17±0.11	0.15±0.03
0.80	0.97	0.479	0.0001	39.49	34.0	93.88±0.29	1.026±0.003	0.20±0.10	0.00±0.00

Table B.3: Bin-by-bin corrections and expected statistical errors on $d\sigma_{\mu\mu}/\cos\theta$ (202-207 GeV)

Appendix C

Predictions from Z′ Models

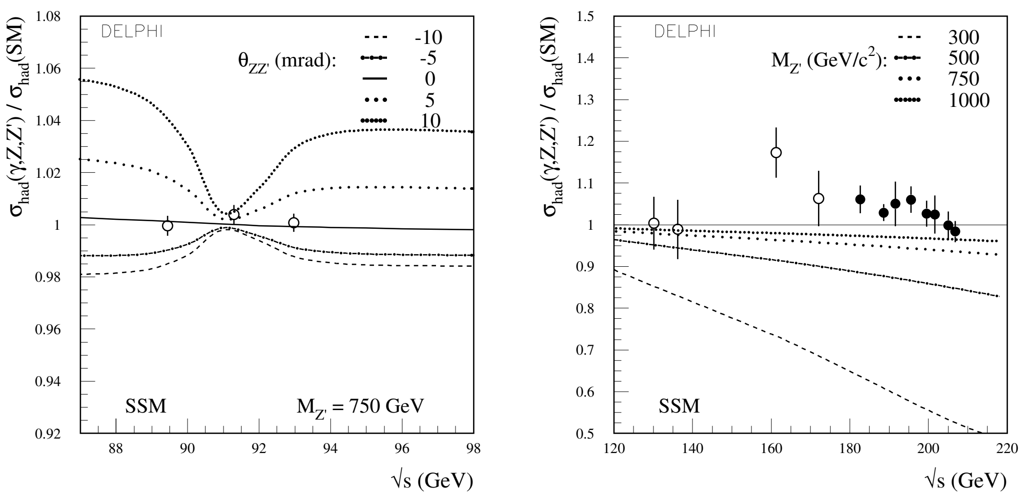

Figure C.1: Comparison of the sequential Standard Model and the SM for the total quark-pair production as a function of the center-of-mass energy, $\sqrt{s}$. The plots show the ratio of the cross section assuming different values for $M_{Z'}$ and $\theta_{ZZ'}$. For LEP II energies $\theta_{ZZ'}$ was set to zero. The closed points are the results presented in [51], the open points present previous results at lower energies from 1995-1996 ($\sqrt{s}$= 89.4, 91.2, 93.0, 130.2, 136.2, 161.3, 172.1 GeV) [53], [54].

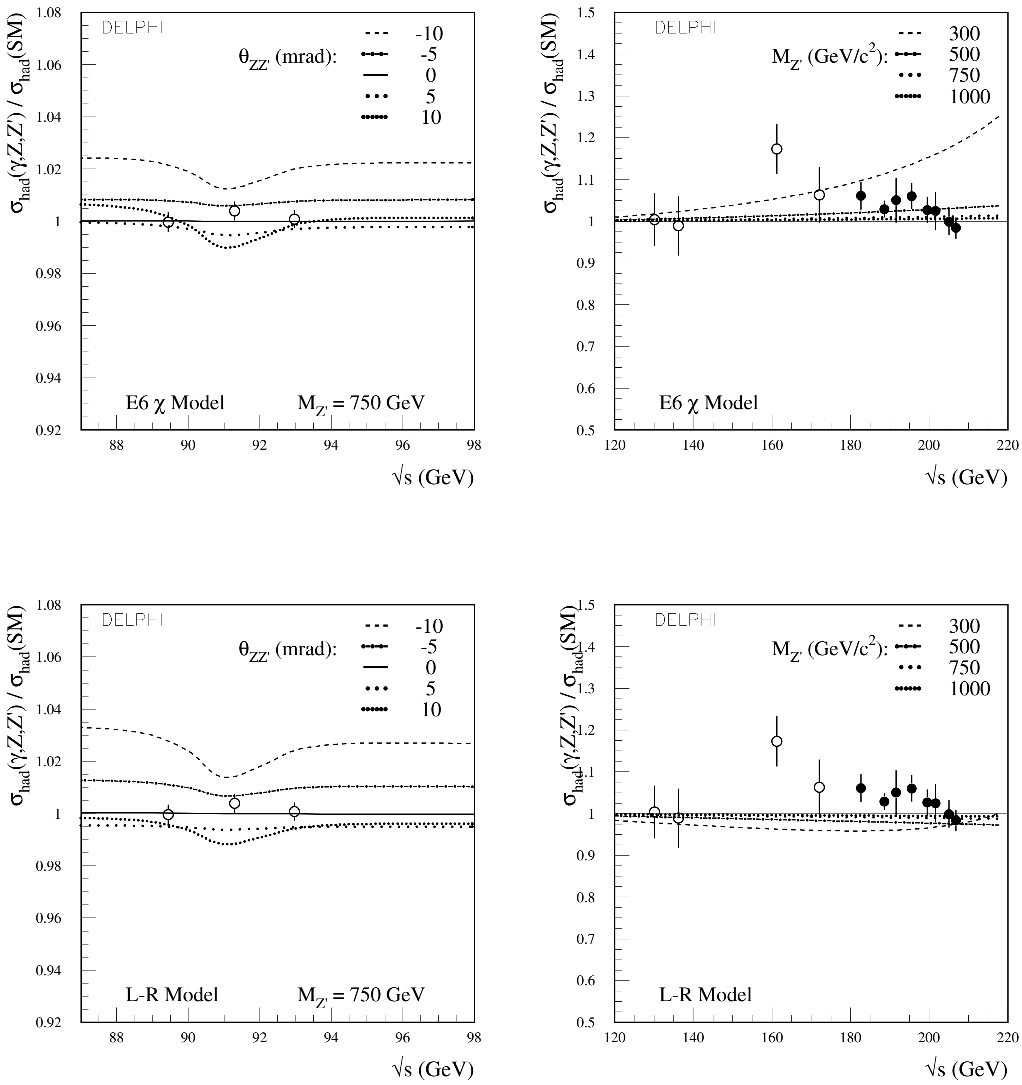

Figure C.2: Comparison of the E_6 χ and L-R model and the SM for the total quark-pair production as a function of the center-of-mass energy, $\sqrt{s}$. The plots show the ratio of the cross section assuming different values for $M_{Z'}$ and $\theta_{ZZ'}$. For LEP II energies $\theta_{ZZ'}$ was set to zero. The closed points are the results presented in [51], the open points present previous results at lower energies from 1995-1996 ($\sqrt{s}$= 89.4, 91.2, 93.0, 130.2, 136.2, 161.3, 172.1 GeV) [53], [54].

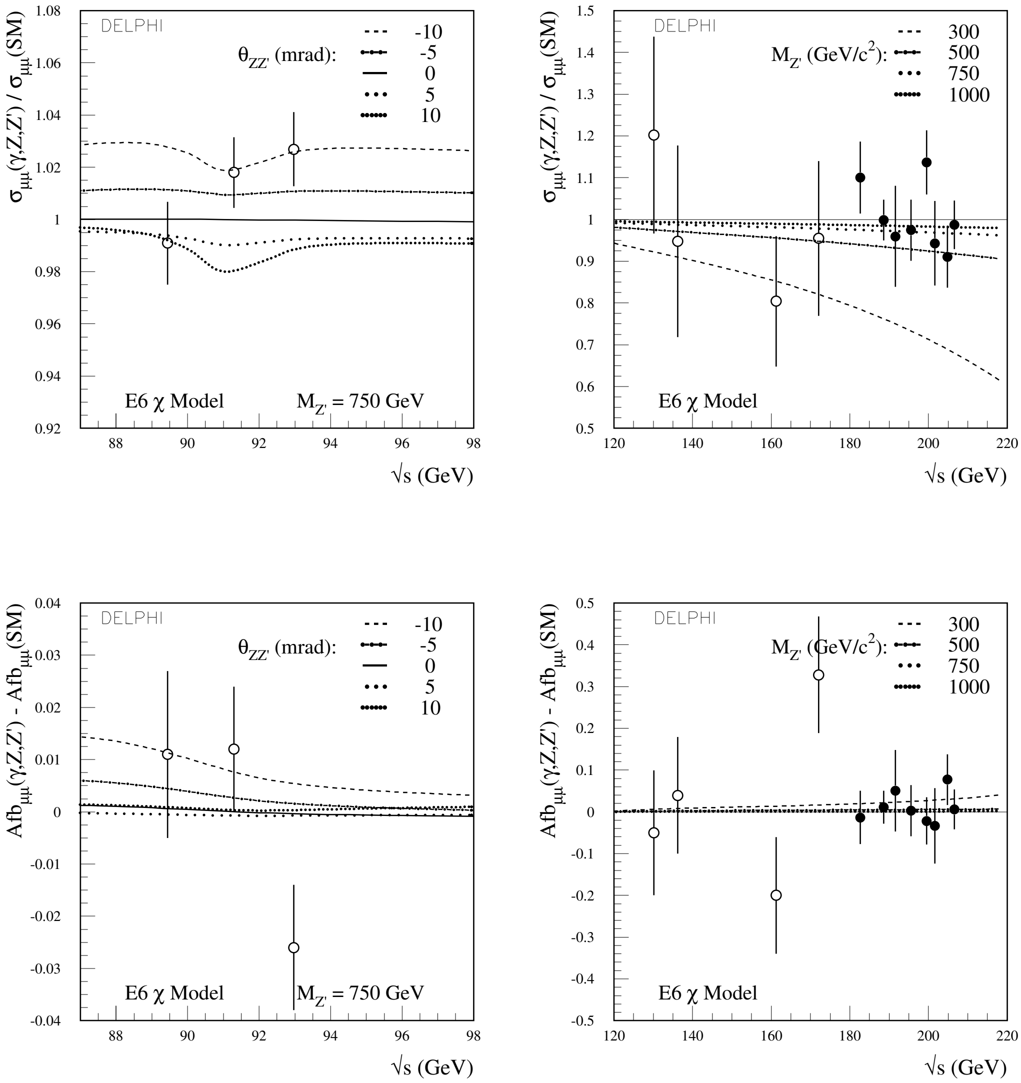

Figure C.3: Comparison of the E_6 χ model and the SM for the muon-pair production as a function of the center-of-mass energy, $\sqrt{s}$. The upper plots show the ratio of the cross section and the lower plots the difference of the forward-backward asymmetry assuming different values for $M_{Z'}$ and $\theta_{ZZ'}$. For LEP II energies $\theta_{ZZ'}$ was set to zero. The closed points are the results presented in this thesis, the open points present previous results at lower energies from 1995-1996 ($\sqrt{s}$= 89.4, 91.2, 93.0, 130.2, 136.2, 161.3, 172.1 GeV) [53], [54].

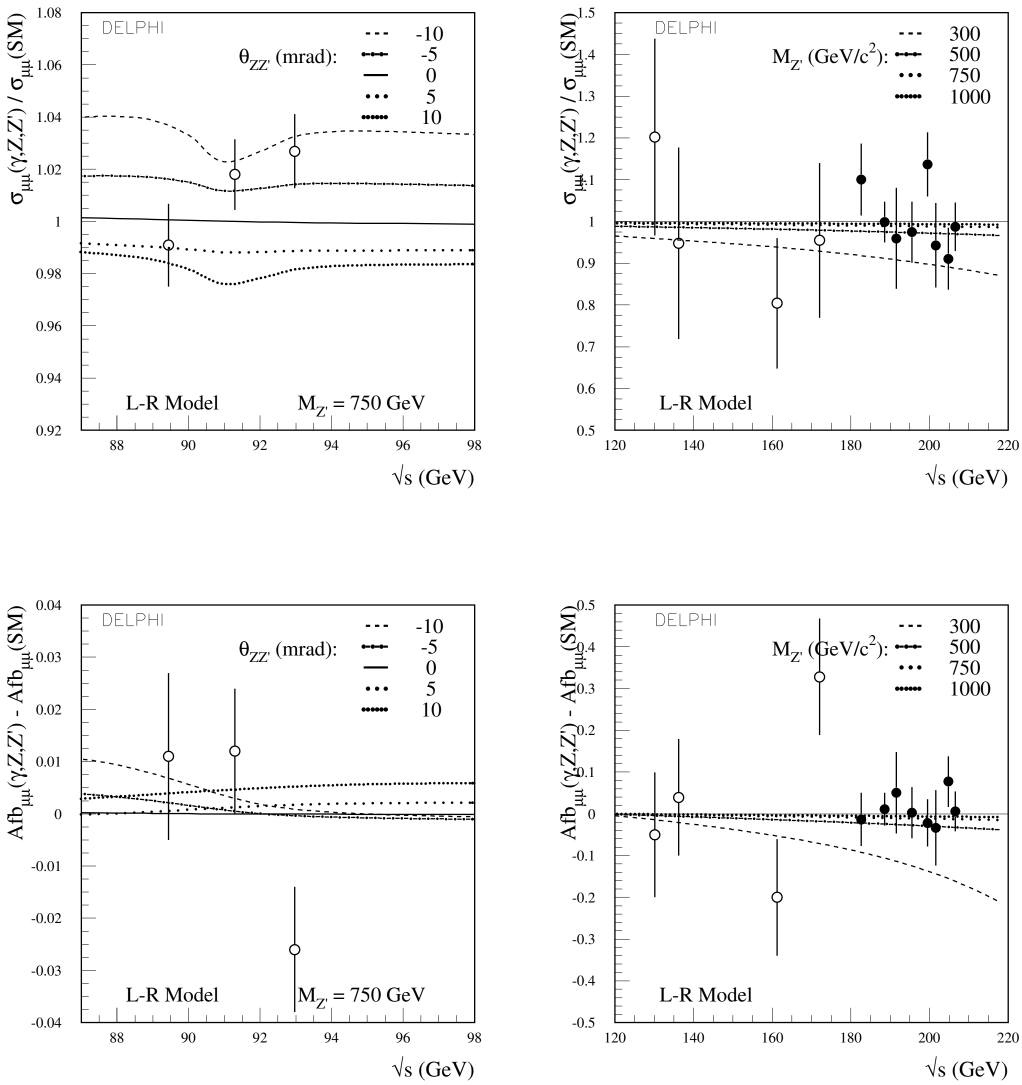

Figure C.4: Comparison of the L-R model and the SM for the muon-pair production as a function of the center-of-mass energy, $\sqrt{s}$. The upper plots show the ratio of the cross section and the lower plots the difference of the forward-backward asymmetry assuming different values for $M_{Z'}$ and $\theta_{ZZ'}$. For LEP II energies $\theta_{ZZ'}$ was set to zero. The closed points are the results presented in this thesis, the open points present previous results at lower energies from 1995-1996 ($\sqrt{s}$= 89.4, 91.2, 93.0, 130.2, 136.2, 161.3, 172.1 GeV) [53], [54].

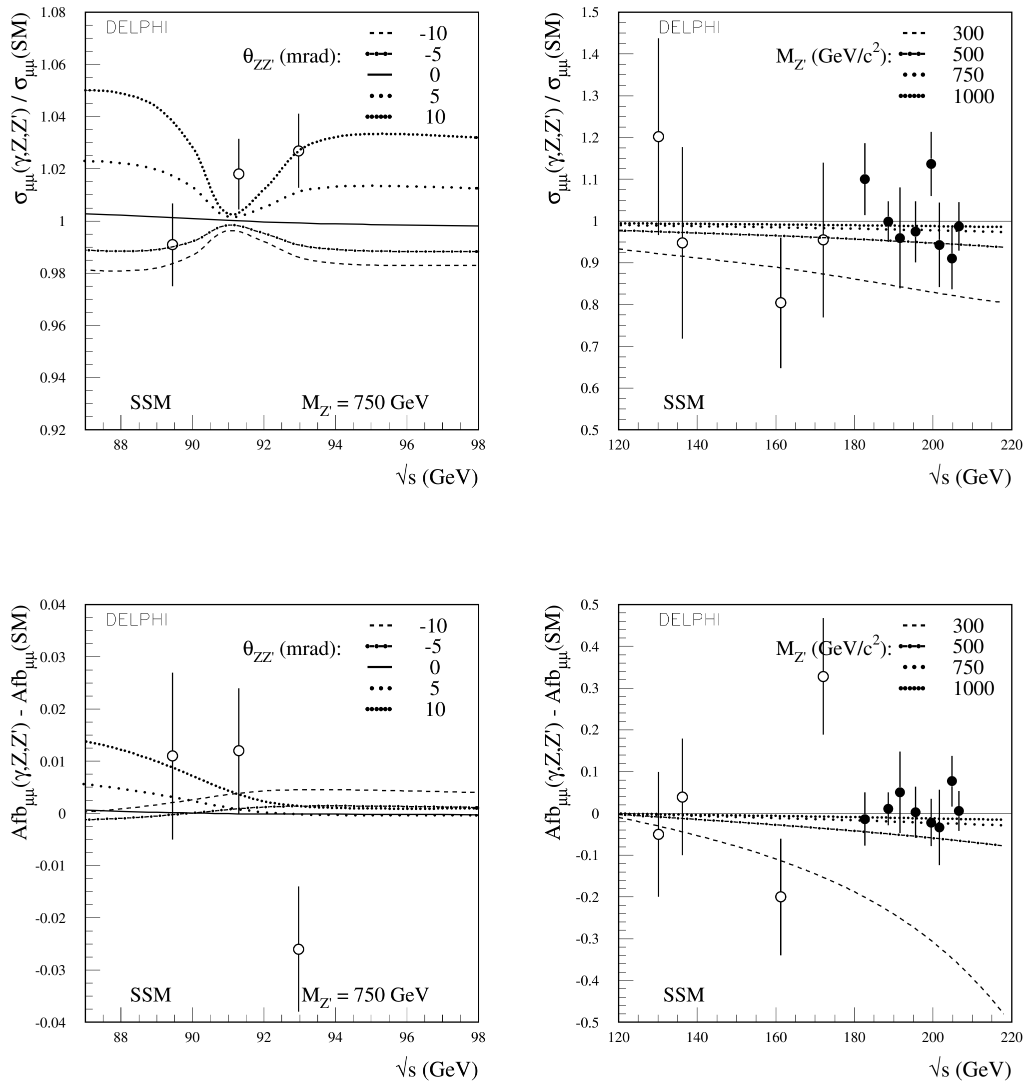

Figure C.5: Comparison of the sequential Standard Model and the SM for the muon-pair production as a function of the center-of-mass energy, $\sqrt{s}$. The upper plots show the ratio of the cross section and the lower plots the difference of the forward-backward asymmetry assuming different values for $\mathrm{M}_{\mathrm{Z}'}$ and $\theta_{\mathrm{ZZ}'}$. For LEP II energies $\theta_{\mathrm{ZZ}'}$ was set to zero. The closed points are the results presented in this thesis, the open points present previous results at lower energies from 1995-1996 ($\sqrt{s}$= 89.4, 91.2, 93.0, 130.2, 136.2, 161.3, 172.1 GeV) [53], [54].

Bibliography

[1] M. Gell-Mann, Phys. Lett. **8** (1964) 214; G. Zweig, CERN-TH-412 (1964)

[2] S.L. Glashow, Nucl. Phys. **B22** (1961) 579; S. Weinberg, Phys. Rev. Lett. **19** (1967) 1264; A. Salam, Phys. Rev. **127** (1962) 331

[3] N. Cabibbo, Phys. Rev. Lett. **10** (1963) 531;
M. Kobayashi, K. Maskawa, Prog. Theor. Phys. **49** (1973) 652

[4] P. Langacker, "Precision Tests of the Standard Electroweak Model", publ. 1995 by World Scientific, ISBN 981-02-1284-4

[5] M. Consoli, W. Hollik, CERN 89-08 Vol 1. (1989), 7;
M. Böhm, W. Hollik, CERN 89-08 Vol 1. (1989), 203

[6] F. Boudjema, B. Mele, CERN 96-01 Vol.1 (1996) 207

[7] M. Kobel *et al.* , "Two-Fermion Production in Electron-positron Collision", in S. Jadach *et al.* , "Reports of the Working Groups on Precision Calculations for LEP2 Physics: proceedings", CERN 2000-009, hep-ph/0007180.

[8] LEP Electroweak Working Group
http://lepewwg.web.cern.ch/LEPEWWG/Welcome.html

[9] P. Langacker, R. Robinett and J. Rosner, Phys. Rev. **D30** (1984) 1470
P. Langacker, Phys. Rev. **D30** (1984) 2008

[10] D. London and J. Rosner, Phys. Rev. **D34** (1986) 1520

[11] J. Pati and A. Salam, Phys. Rev. **D10** (1974) 275
R. Mohapatra and J. Pati, Phys. Rev. **D11** (1975) 566

[12] P. Langacker and M. Luo, Phys. Rev. **D45** (1992) 278

[13] P. Chiappetta and C. Verzegnassi, "Z' Physics", Workshop Contr. Physics at LEP2

[14] B. Greene, "The elegant Universe", (1999), W.W. Norton & Company, NY, London

[15] T. Kaluza, Sitzungsber. Preuss. Akad. d. Wiss., Phys. Math. Klasse 996 (1921), O. Klein, Z. f. Physik, **37**, 895 (1926), reprinted in Modern Kaluza-Klein Theories, T. Appelquist, A. Chodos, P.G.O. Freund (Addison-Wesley, Menlo Park, 1987)

[16] G. Gabadadze, "ICTP Lectures on large Extra Dimensions", CERN-TH/2003-157

[17] N. Arkani-Hamed, S. Dimopoulos, G. Dvali, Phys. Lett. **B429** (1998) 263, I. Antoniadis, N. Arkani-Hamed, S. Dimopoulos and G. Dvali, Phys. Lett. **B436** (1998) 257

[18] N. Arkani-Hamed, S. Dimopoulos, G. Dvali, Phys. Rev. **D59**, 086004 (1999)

[19] G.F. Giudice, R. Rattazzi and J.D. Wells, Nucl. Phys. **B544** (1999) 3

[20] I. Antoniadis, Phys. Lett. **B246**, 377 (1990); J. Lykken, Phys. Rev. **D54**, 3693 (1996); E. Witten, Nucl. Phys. **B471**, 135 (1996); P. Horava and E. Witten, Nucl. Phys. **B460**, 506 (1996)

[21] J. L. Hewett, Phys. Rev. Lett. **82** (1999) 4765 (SLAC-PUB-8001 1998)

[22] The LEP Energy working Group, "Calibration of center-of-mass energies at LEP1 for precise measurements of Z properties", Eur. Phy. J. **C6** Vol.2 (1999) 187

[23] The LEP Energy Working Group, "Evaluation of the LEP centre-of-mass energy for data taken in 2000", 01/01 (March 2001); "Evaluation of the LEP center-of-mass energy above the W-pair threshold", Eur. Phy. J. **C11** Vol.4 (1999) 573

[24] The DELPHI Collaboration, Nucl. Instr. and Meth. in Phys. Research **A 303** (1991) 233 and **A 378** (1996) 57

[25] A. Augustinus *et al.* , "The DELPHI Trigger System at LEP2 Energies", CERN-EP/2002-086 (November 2002)

[26] DELPHI Coll. "Event viewing software", Note 89-6, 1989

[27] DELPHI Coll. "DELPHI event generation and detektor simulation", Note 89-67, 1989

[28] S. Jadach, B. Ward and Z. Was, "The Precision Monte Carlo Event Generator $\mathcal{KK}$ for Two-Fermion Final States in e^+e^- Collisions", Comp. Phys. Comm. **130** (2000) 260

[29] A. Behrmann, P.J. Holt, "Muon Momentum and Muon Chamber Efficiency Corrections for LEP II", DELPHI 2002-017 PHYS 918 (April 2002)

[30] P. Billoir, Y.Sacquin "The DELPHI TPC distortions", DELPHI 92-16 TRACK 68 (January 1992)

[31] E. Piotto, P. Charpentier, W. Venus, J. Wickens, Y. Arnoud "Correction of the TPC distortions for the final processing of LEP II data", DELPHI 2001-110 TRACK 96 (June 2001)

[32] M. Elsing *et al.* , "Changes in the track reconstruction to recover from the TPC sector 6 failure", DELPHI 2001-004 TRACK 95 (January 2001)

[33] D. Bardin *et al.* , "ZFITTER v.6.21 , A Semi-Analytical Program for Fermion Pair Production in e^+e^- Annihilation", DESY 99-070 (1999) [hep-ph/9908433] publ. in: Comp. Phys. Commun. **133** (2001) 229-395

[34] N. Kjaer, R. Möller, "Reconstruction of Invariant Masses in Multi-Jet Events", DELPHI 91-17 PHYS 88 (April 1991)

[35] A. Behrmann, "Analyse der Myonpaarproduktion in der e^+e^--Annihilation bei Energien oberhalb der Z-Resonanz", Diploma Thesis WUD 98-18 (June 1998)

[36] T. Burgsmüller, "Untersuchung der Myon-Paarproduktion bei Energien auf und oberhalb der Z–Resonanz", Dissertation WUB-DIS 98-7 (August 1998)

[37] A. Behrmann, G.W. Morton, "Determination of the Muon ID and Track Reconstruction Efficiencies using Data collected in 1998", DELPHI 2000-002 PHYS 845 (January 2000)

[38] V. Canale, Private Communication

[39] E. Accomando, A. Ballestrero, Comp. Phys. Comm. **99** (1997) 270
E. Accomando, A. Ballestrero, E. Maina, Comp. Phys. Comm. **150** (2003) 166

[40] A. Ballestrero, R. Chierici, F. Cossutti, E. Migliore, "Four-fermion simulation at LEP2 in DELPHI", CERN-EP/2002-069 (June 2002)

[41] F. A. Berends, P. H. Daverveldt, R. Kleiss, "Monte Carlo Simulation of Two-Photon Processes", Comp. Phys. Comm. **40** (1986) 271

[42] Jadach, Stanislaw; Placzek, Wiesiek; Ward, B F L, "O(alpha) YFS Exponentiated Monte Carlo for Bhabha Scattering at Wide Angles for LEP1SLC and LEP2", hep-ph/9608412; UTHEP-95-1001. (August 1996)

[43] A. Ballestrero, Private Communication

[44] S. Jadach, B. Ward and Z. Was, "Coherent exclusive exponentiation CEEX", Phys. Lett. **B 449** (1999) 97-108, "Coherent Exclusive Exponentiation of 2f Processes in e^+e^- Annihilation", Nucl. Phys. B, Proc. Suppl. **89** (2000) 106-111, "Coherent Exclusive Exponentiation For Precision Monte Carlo Calculations" Phys. Rev. **D 63** (2001) 113009/1-65

[45] S. Jadach, B. Ward and Z. Was, Comp. Phys. Comm. **79** (1994) 503, Comput. Phys. Commun. **124** (2000) 233-237

[46] A. Arbuzov *et al.* , Phys Lett. **B 383** (1996) 238,
S. Jadach *et al.* , Comp. Phys. Commun. **102** (1997) 229 and "New Results on the Theoretical Precision of the LEP/SLC Luminosity", Phys. Lett. **B 450** (1999) 262

[47] L. Lyons *et al.* , Nucl. Inst. Meth. **A207** (1988) 110

[48] S. Riemann, FORTRAN Program ZEFIT, version 6.10

[49] A. Leike, S. Riemann, T. Riemann, "ZZ′ Mixing in Presence of Standard Weak Loop Corrections", LMU-91/06, hep-ph/9808374

[50] K. Hagiwara *et al.* , Physical Review **D66** (2002), 010001

[51] P. Abreu *et al.* , "Measurement and Interpretation of Fermion-Pair Production at LEP energies above the Z Resonance" CERN-EP/2002-332 / draft 1

[52] DELPHI Collaboration, P. Abreu *et al.* , Nucl. Phys. **B417** (1994), 3
DELPHI Collaboration, P. Abreu *et al.* , Nucl. Phys. **B418** (1994), 403

[53] DELPHI Collaboration, P. Abreu *et al.* , Eur. Phys. J. **C16** (2000), 371

[54] DELPHI Collaboration, P. Abreu *et al.* , Eur. Phys. J. **C11** (1999), 383

[55] DELPHI Collaboration, P. Abreu *et al.* , Phys. Lett. **B485** (2000), 45

[56] F. James, “MINUIT, Function Minimization and Error Analysis, Reference Manual”, CERN Program Library (1992)

[57] CERN-EP/2002-091, LEP electroweak and SLD working group, "Combination of Preliminary Electroweak Measurements and Constraints on the Standard Model", LEPEWWG/2002-02, ALEPH 2002-042 Physic 2002-018, DELPHI 2002-098 PHYS 927, L3 note 2788, OPAL PR 370 (2001)

[58] LEPEWWG $f\bar{f}$ Subgroup, C. Weniger *et al.* , "Combination of the LEP II $f\bar{f}$ Results", Results for Summer Conference 2002. LEP2FF/02-03, ALEPH 2002-039 Physic 2002-015, DELPHI 2002-096 PHYS 926, L3 note 2785, OPAL TN727 (2000)

[59] see web page: http://lepewwg.web.cern.ch/LEPEWWG/lep2/summer2002/Welcome.html

[60] LEPEWWG Line Shape Subgroup, “Combination procedure for the precise determination of Z boson parameters from results of the LEP experiments”, CERN-EP-2000-153 (2000)

[61] M.K. Pillai “Limits on Z' production at the Tevatron using CDF & DØ data”, hep-ex/9608013 (1996), DØ Collaboration, S. Abachi *et al.* , Phys. Lett. **B385** (1996) 471, CDF Collaboration, F. Abe *et al.* , Phys. Lett. Rev. **79** (1997) 2192

[62] A. Leike, S. Riemann, “Z' search in e^+e^- annihilation”, Z. Phys. **C75**, 341-348 (1997)

[63] P. Comas, M. Martinez, Z. Phys. **C58** (1993) 15

[64] I. Boyko, “Tau Pair Selection at LEP2”, DELPHI 2000-147 PHYS 869 (2000)

[65] G. W. Morton, “A Study of $e^+e^- \to \mu^+\mu^-(\gamma)$ and a Search for Quantum Gravity in Large Extra Compactified Dimensions at LEP2”, D. Phil. Thesis, Oxford (2000)

[66] The ALEPH Collaboration, Eur. Phys. J. **C28** (CERN-EP/2002-033 (2002)) CERN-ALEPH-2002-032 (2002), CERN-ALEPH-2000-047 (2000)

[67] The L3 Collaboration, CERN-EP/2003-034 (2003), CERN-EP/2001-096 (2001), Phys. Lett. **B470** (1999) 281, CERN-EP/99-146 (1999), Note 2543

[68] The OPAL Collaboration, Physics Note 440 (2000), Note PN471 (2001), CERN-EP-2002 060 (2002), CERN-EP-99-097 (1999), Eur. Phys. J., **C13** (2000) 553-72

[69] D. Bourilkov, Review Talk given in La Thuile, Italy, March 2001, “Two-fermion and Two-photon Final States at LEP2 and Search for Extra Dimensions”, preprint hep-ex/0103093 (2001)

[70] DØ Collab., B. Abbot *et al.* , Phys. Rev. Lett. **86** (2001) 1156

[71] H1 Collab. submitted paper 979 to ICHEP02, Amsterdam (2002)
Zeus Collab. submitted paper 602 to EPS HEP01, Budapest (2001)

[72] G. Pásztor, “Search for Supersymmetry, extra Dimensions and exotic Phenomena at LEP”, Talk given in La Thuile , Italy, March 2003, preprint hep-ex/0210015

Acknowledgements

In particular, I would like to thank my doctoral advisor Prof. Dr. Jürgen Drees for offering me the possibility to work in this interesting field and for motivating this analysis. He provided me with the confidence and freedom I needed to achieve the results presented here and supported me, whenever necessary, in a very encouraging way. The participation in an international Collaboration including many visits to Cern and attendances at national and international conferences was a very valuable experience.

I also would like to thank the second referee Prof. Dr. K.-H. Becks. I greatly appreciated the help and constant support of Dr. Helmut Wahlen, specially during the numerous team meetings at Cern. His experience has been a great profit to this analysis.

I am grateful to my colleagues of the physics department at the university of Wuppertal who took part in the success of this thesis. Special thanks go to Tobias Burgsmüller who, at the beginning, introduced me into the muon analysis and which I continued afterwards, and Patrick Buschmann for his great effort to develop my technical skills. I am much obliged to our computer administrators Karl-Heinz Becker, Torsten Harenberg and Andreas Kootz for their help whenever necessary and who did an excellent job keeping the machines running (even the VMS cluster).

Without the work of many people performing the experiment this thesis would have been impossible. I am owing great thanks to the members of the DELPHI collaboration. Particularly, I am grateful to the 2-Fermion/2-Photon team for a pleasant and helpful cooperation. My special thanks go to John Holt from the Oxford group for many inspiring discussions. I would like to thank the many people I met at Cern who made the time there so interesting and enjoyable.

I also would like to thank Sabine Riemann, the author of the ZEFIT package, for her help and support performing the Z' fits.

Many thanks to Moira Casey and Birgit Kühn for their help in English proof-reading of the manuscript.

Last but definitely not least I thank my parents for their great and unconditional support, and Peter for his patience and understanding during these years.